THE PEAK-PATCH PICTURE OF COSMIC CATALOGS. I. ALGORITHMS

J. R. BOND

CIAR Cosmology Program, Canadian Institute for Theoretical Astrophysics, McLennan Physical Laboratories, Toronto, ONT M5S 1A1, Canada

AND

S. T. MYERS

Department of Astronomy, 105-24, California Institute of Technology, Pasadena, CA 91125; David Rittenhouse Laboratory, University of Pennsylvania, 209 S. 33d Street, Philadelphia, PA 19104-6396

ABSTRACT

We develop a picture of cosmic structure formation that identifies virialized cosmological objects with a point process of "peak patches" in the initial (Lagrangian) space. The strongly nonlinear internal dynamics of the collapsing patch is largely decoupled from the weakly nonlinear dynamics describing peak-patch flow. A modest set of local field measurements on the patch region suffices to approximately determine the fate of the peak. The candidate peak points are identified using a hierarchy of smoothing operations on the density field. Patch size and mass are found by requiring complete collapse of a homogeneous ellipsoid model for internal patch dynamics which includes the important influence of the external tidal field. Exclusion algorithms that prevent peak-patch overlaps trim the candidate list into the final "hierarchical peak" list. The Zeldovich approximation with locally adaptive filtering of the displacement field is used for external dynamics to move the surviving patches to their final state (Eulerian) positions, augmented by a quadratic nonlinear correction where necessary. Thus both statistical and dynamical clustering of the peaks are included. Our technique is the natural generalization of both the Press-Schechter method (to include nonlocal effects) and the BBKS single-filter peaks theory (to allow a mass spectrum and solve the cloud-in-cloud problem). It allows efficient Monte Carlo constructions of three-dimensional catalogs of objects such as groups and clusters of galaxies, and, with more selection criteria, of galaxies in their formation phases.

Subject headings: cosmology: theory — galaxies: clusters: general— galaxies: formation — methods: numerical

1. INTRODUCTION

One might wonder why we put effort into approximate descriptions of cosmic structure formation given the tremendous recent and promised advances in computing power. Surely the not very distant future will bring computations of arbitrarily large simulation volumes with arbitrarily high resolution using arbitrarily adaptive hydrodynamical and *N*-body techniques. That will be so. But even so, we need a physical language to discuss the outcomes.

For the all important rare events in the medium, such as massive clusters now and bright galaxies at high redshift, the appropriate idiom is the flowing peak patch at which grand constructive interferences in density and velocity waves mark out the sites of collapse. And radiating outward from the peak-patch core are filaments and sheets that too are rare. The structure may finally fade into the root-mean-square fluctuations in the medium as coherence in the phases fades into randomness. Or the structure may blend into another peak patch, for rare constructive interferences tend to be clustered. No image from the cosmology of the 1980s was as powerful as the CfA picture of Coma and its Great Wall, the paradigm for a peak patch and its environs.

Because most observables rely on luminosity, the root-mean-square fluctuation is not the typical catalog member. We catalog from the bright end downward. Thus we are most sensitive to intermittency in the medium, the rare fluctuations where the observable action happens. The goal of cosmological *N*-body or gas-dynamical computations is to identify structures in the simulation volume, measure their internal and external properties, and compare these with observational catalogs. It is a delicate art to construct a point process that can serve as a Monte Carlo realization of a given observational catalog—even with the most ambitious simulations. This is because the physics which defines the observational point process is typically far beyond what can be simulated. Certainly anything to do with stars forming and exploding in cosmology has this unfortunate feature. It is very useful to have a variety of techniques for constructing catalogs, with simplifying assumptions being offset by computational speed.

In this paper, we describe a rapid Monte Carlo method for identifying collapsed structures based on the peak-patch picture. In a second paper in this series, Bond & Myers (1995a, hereafter BM2), we show that our approximate catalogs compare well with those of *N*-body groups and cost only a small fraction of the *N*-body computer time to construct. We believe this gives solid proof that the peak-patch picture works, especially for rare events. In a Bond & Myers (1995b, hereafter BM3), we apply the technique to clusters of galaxies. In a fourth paper, Bond & Myers (1995c, BM4), we describe an analytical counterpart to the peak-patch picture which allows even more rapid calculations of catalogue properties. An early version of the hierarchical peaks algorithm was described in Bond & Myers (1991).

1

Developing or applying semi-analytic approaches to catalog statistics has been one of the main source of cosmological papers for the past two decades. There have been two main streams that purport to determine these statistics from the initial structure of the cosmological fields defining the theoretical structure formation model. These are the density excursion set or Press-Schechter approach (Press & Schechter 1974, hereafter PS) and the density peaks approach (Bardeen et al. 1986, hereafter BBKS). Although much used for the construction of "one-point statistics" such as mean number density functions for mass, X-ray temperature, and velocity dispersion, almost all users now treat the PS function as a fitting formula that has been shown to fit mass functions for N-body groups reasonably well. That is because there is little physical justification for the original PS formula. The main difficulty is that points in the medium that collapse together to form a virialized object of a given mass will actually be counted as belonging to objects of different mass, as Bond et al. (1991, hereafter BCEK) showed graphically by comparing with N-body calculations. Another unappealing aspect is that the derivation of the PS formula requires a rather unphysical form of density smoothing which uses an oscillatory window function (associated with a "top hat" filter in Fourier transform space) and an arbitrary mass assignment scheme (BCEK). More natural window functions such as top hats in position space, or Gaussians, lead to different formulae which are not quite as phenomenologically successful as the PS one (Peacock & Heavens 1990; BCEK). Although we call our technique the hierarchical peak-patch picture, we could equally well call it the nonlocal Press-Schechter picture, since it is the natural generalization of the PS method which ensures that nearby points which collapse together are counted in the same object and that natural top-hat filtering is used for mass assignment (§ 3.3). An early nonlocal prescription using the basic PS framework was the "brick" model used by Cole & Kaiser (1988).

Peak theory applied to cosmological models was first developed by Doroshkevich (1970) and Doroshkevich & Shandarin (1978a, b) for models with a natural filter such as adiabatic hot dark matter models in which large structures from first, and for hierarchical models such as the cold dark matter model by Peacock & Heavens (1985) and BBKS. The BBKS theory gave a calculational framework for constructing clustered points in the initial conditions (in Lagrangian space) for an N-body simulation that were identified with galaxies or clusters and which could then be moved along via N-body algorithms to give an evolved final clustering pattern (in Eulerian space). This was essential before the recent expansion of computational capabilities (e.g., Davis et al. 1985) and is still being used to good effect for very large scale structure simulations (e.g., Park 1990). More importantly, it gave us a way to determine correlation functions in the linear regime by simply computing a bias factor by which the long wavelength object-density field is amplified over the long-wavelength mass-density field. But, in our estimation, the most significant contribution was the language it gave us to discuss cosmic evolution sensibly rather than resorting to "this is what the N-body code tells us." This paper and its companions correct the grammar and modify the syntax, but essentially confirm the vocabulary.

The BBKS picture used a single-filter snapshot of the medium, identified the density peaks in the snapshot, and assigned them all the same mass, identified as the mean density times the volume associated with the smoothing window. A necessary ingredient for comparison with catalogues are differential mass functions, but no $dn_{pk}(M)/d \ln M$ could be constructed. A first attempt using multiple filter snapshots and a better estimation of mass using peak profiles was made in Bond (1988), but was only moderately successful because it did not solve the "cloud-in-cloud" problem that BBKS emphasized: within large-sized peaks there will be smaller ones whose inclusion could lead to overcounting of objects. Thus an exclusion criterion for removing peaks is essential. Bond (1989a) gave an analytic formula for the differential number density which was shown to be the high peak limit of a more general formula (Bond 1989b). The Bond (1989b) mass function formula counted only those density peaks on a given filter scale which were *just* crossing through a density threshold whose height was chosen to correspond to a spherical approximation for dynamical evolution of the peak. This requirement that the density height be a precise value solved most of the cloud-in-cloud problem. An approximate formula describing further exclusion was also given. Much analytic development has occurred since then and is described in BM4.

We sketched an early version of our peak-patch simulation method for constructing catalogues in Bond & Myers (1991). There we assumed a spherical model for the collapse dynamics. Our method has undergone many refinements since then, which we describe in detail in this paper.

In § 2, we introduce the peak-patch picture and the density, displacement, and strain fields of relevance for peak-patch measurements. The dynamical equations for the homogeneous ellipsoidal collapse are presented in § 2.1.3 and derived in Appendix A. We present the expressions for the internal energy of the collapsed patch § 2.1.4 (derived in Appendix B) which we use for estimations of virial velocities. The makeup of a peak patch and the effect of the background and fluctuation fields upon its fate are discussed in § 2.2, where realizations of constrained Gaussian random fields are used to illustrate the importance of the external tidal fields, subclumping and bulk peak velocity for defining the nature of the peak-patch. The methods used to make the constrained field simulations are discussed in Appendix C.

The point process used to define our "cosmic" catalogs is introduced in § 3, along with the important topics of Lagrangian exclusion and Eulerian merging. In § 3.3, the hierarchical peaks formulation of the peak-patch picture is put in the context of a generalized Press-Schechter method.

In § 4, we present and discuss in detail our numerical algorithms for realizing density and displacement fields in very large regions that cover the catalog volume, finding candidate peak points, measuring their mass, initial energy, and bulk velocity, excluding or modifying candidate patches which overlap, and finally mapping from Lagrangian (initial state) space to Eulerian (final state) space using the Zeldovich approximation for the external dynamics. We show some of the basic internal properties we measure and compare the hierarchical peak mass function with the PS mass function in § 4.2. We present many more results in the companion Paper II, where they are directly confronted with the results of N-body simulations.

2. PEAK PATCHES IN THE DENSITY AND DISPLACEMENT FIELDS

What we wish to develop is a method that differentiates fast (nonlinear) internal dynamics from slower (hopefully linear) external dynamics of collapsing structures. The conceptual picture is that of a local "peak patch" collapsing to form the object in question, with the entire patch moving with a bulk peculiar velocity, and acted upon by external tidal fields, determined by long-wavelength components of the fields. The locations of the peak-patches define a point process. Of course the split between what is external and what is internal is necessarily time dependent to take into account, for example, matter accreting or objects merging. Apart from the dipole (bulk velocity) and quadrupole (tidal field), there will generally be external octupole and higher multipole fields that can only be ignored with some error.

Much theoretical work is going into designing spatially and temporally adaptive algorithms to allow fully coupled interior and exterior evolution for very large simulation volumes, and there is little doubt that this represents the long-range future of the subject. Consider some of the N-body methods currently being used. Typically tree codes have a fixed softening length but can have spatially adaptive time stepping implemented (Barnes & Hut 1986, 1989; Hernquist & Katz 1989). The adaptive P^{3}M method of Couchman (1991) uses extra local meshes for determining the gravitational force around active dynamical regions; it has a fixed softening length and a spatially constant time step. The adaptive PM method of Villumsen (1989) also uses extra local meshes to determine the gravitational potential. With current computing limitations, the price one pays for trying to get enough members for a full catalog from a simulation is that the internal resolution of the members is not very good.

A general method more akin to the philosophy we adopt here is to follow the evolution of single members with high resolution to determine internal properties by setting up constrained initial fields which condition the simulation volume to have the structure forming within it. The locations and peculiar velocities of catalog members are determined by other lower resolution techniques. The simplest way to set up a constrained field is to cut out dynamically interesting patches from a low resolution realization, add higher spatial frequency components to the fields, as much as the resolution permits, then spawn a separate calculation. Another approach useful for fields which are initially Gaussian is to directly make constrained realizations for the patch (e.g., Bertschinger 1987). Proper treatment of boundary conditions and external fields is essential if this constrained method is to accurately give internal properties.

Although the details of collapse and virialization depend upon all aspects of the local field associated with the peak patch, and thus on an infinite number of degrees of freedom, the gross features are sensitive to a much smaller number of degrees of freedom. That is why lower resolution simulations often reproduce the main features of higher resolution ones, such as correlation functions and mass functions, although details of the collapsed objects such as merging times, substructure, and orbital dynamics may be poorly reproduced. (Of course, gas-dynamical computations can be quite sensitive to very high spatial frequencies, through feedback from supernovae, etc.) What is difficult to determine is an optimal and minimal set of degrees of freedom that largely determine a specific property we are interested in measuring. However, we can adopt the main lessons from a study of the evolution of constrained fields around density peaks to guide us to some of the necessary, if not sufficient, local measurements needed. As we shall see, the constraints of most relevance here are the bulk velocity, the external tidal field and the average overdensity.

2.1. Internal and External Fields for Peak Patches

The nonlinear gravitational evolution of a medium is a highly complex phenomenon—even without complications arising from gas dynamics or primordial velocity dispersions in the dark matter. In many circumstances in cosmology, gravitational forces are sufficiently dominant over pressure forces that the pressure can be ignored, at least to get the main features of the evolution of the medium. This is true, of course, for the cold dark matter model. In that case, the gravitational evolution is a mapping from an unperturbed Lagrangian space in which the cold particles are labeled by their initial positions r to a highly perturbed Eulerian space with the particles at physical (expanding) Eulerian positions $X(r, t) \equiv \bar{a}(t)x(r, t)$ at time t, where the comoving Eulerian coordinate x has the average (background) expansion factor of the universe, $\bar{a}(t)$ factored out. The mapping can quite generally be written in terms of a displacement field $s(r, t)$ describing the deviation of the particle from its initial site:

$$x(r, t) \equiv r - s(r, t) \tag{2.1}$$

The peculiar velocity is

$$V_P \equiv \dot{X} - HX = -\bar{a}(t)\frac{\partial}{\partial t}s(r, t), \tag{2.2}$$

where $H \equiv \dot{\bar{a}}/\bar{a}$ is the Hubble parameter. (In the case in which the particles have a primordial velocity dispersion, the initial (thermal) velocity of the particles is, of course, also needed to label the particles.)

In the early evolution of a cold medium, linear perturbation theory holds, and the displacement and peculiar velocity fields are separable (Zeldovich 1970):

$$\text{Zeldovich approximation: } s(r, t) = D(t)s(r), \qquad V_P(r, t) = -\bar{a}(t)H_D s(r), \text{ with } H_D \equiv \dot{D}/D . \tag{2.3}$$

$D(t)$ is a function describing the linear growing mode of fluctuations (Peebles 1980, § 2.3). We normalize $D(t)$ to be unity at the present. In a $\Omega = 1$ cold dark matter universe, $D(t) = \bar{a}(t)$ and its logarithmic time derivative H_D is just the Hubble parameter H, but in the general case the evolution is more complex. The initial displacement field is denoted by $s(r)$. It is normalized at $D = 1$, hence corresponds to extrapolating linear growth until the current time.

The mapping from Lagrangian to Eulerian space is initially invertible for small D, remaining so until caustics appear, at which point the medium becomes multistream, and the map x develops many branches. One must resort to N-body simulations to obtain $s(r, t)$ accurately. Obviously we would like to find simplifications to avoid always resorting to N-body studies.

The Zeldovich approximation describes the broad textural features of a cold medium, provided one smooths the displacement field sufficiently so that the deviation from linearity is not too great. It has had its greatest success in the adhesion approximation (Gurbatov, Saichev, & Shandarin 1989; Shandarin & Zeldovich 1989), in which particles are free to follow the Zeldovich displacement field, except an artificial viscosity does not allow them to stream through each other, but rather to stick at caustics. However, in three dimensions the Zeldovich approximation for $s(r, t)$ does not give an accurate description of even relatively weak nonlinearity. This is because the places where structure first forms in the medium are around the rarest high peaks of the density field, which are relatively spherical (BBKS; Bernardeau 1994). The nonlinear evolution is then approximately that of a spherical cold collapse, which turns around and reaches zero radius much faster than the Zeldovich approximation would predict. Thus, although the Zeldovich approximation and its adhesion variant may be adequate for gross large-scale features of the flow, it cannot be used by itself to build a catalogue. In particular, it is hopeless for describing internal properties of collapsed structures.

2.1.1. Smoothing Kernels for Fields

We first introduce the smoothing operations we use on the fields. We denote the (unsmoothed) linear density field by $F(r, t)$, its Fourier transform by $\tilde{F}_k$ and its power spectrum by the ensemble average $P_F(k) \equiv \langle |\tilde{F}_k|^2 \rangle$. The smoothed field is a convolution,

$$
F(r, t; R_f) \equiv \int d^3r' W_f(r - r'; R_f) F(r', t)
$$

$$
= \int \frac{d^3k}{(2\pi)^3} \tilde{F}_k \tilde{W}_f(k; R_f) e^{ik \cdot r}, \qquad f = G, \text{TH}, k, \text{sph}, \dots, \tag{2.4}
$$

where $W_f(r; R_f)$ is a window function, $\tilde{W}_f(k; R_f)$ is its Fourier transform, a filter function, and R_f denotes the filter scale characterizing the falloff of $\tilde{W}(k)$ at high k. For Gaussian filtering on scale R_G the window and filter functions are

$$
W_G(r; R_G) = \frac{1}{(2\pi)^{3/2} R_G^3} \exp[-r^2/(2R_G^2)], \qquad \tilde{W}_G(k; R_G) = \exp[-(kR_G)^2/2], \tag{2.5}
$$

while for "top hat" filtering on scale R_{TH},

$$
W_{\text{TH}}(r; R_{\text{TH}}) = \frac{1}{(4\pi/3)R_{\text{TH}}^3} \vartheta(R_{\text{TH}} - |r|), \qquad \tilde{W}_{\text{TH}}(k; R_{\text{TH}}) = 3j_1(kR_{\text{TH}})/(kR_{\text{TH}}), \tag{2.6}
$$

where j_1 is the spherical Bessel function of order 1. Here, ϑ is the Heaviside unit function. A third type of smoothing is top-hat filtering in k-space:

$$
W_k(r; R_k) = \frac{1}{(6\pi^2)R_k^3} 3j_1(r/R_k)/(r/R_k), \qquad \tilde{W}_k(k; R_k) = \vartheta(R_k^{-1} - |k|). \tag{2.7}
$$

We shall also have occasion to use a filter which is a good approximation to the Gaussian for small k, but whose smoothing function is a piecewise polynomial of compact support, yet is continuous in its first and second derivatives:

$$
W_{\text{sph}}(r; R_h) = \frac{1}{\pi R_h^3} W_{\text{nsph}}(r/R_h), \tag{2.8}
$$

$$
W_{\text{nsph}}(u) \equiv \begin{cases} 1 - (3/2)u^2 + (3/4)u^3, & 0 \le u \le 1, \\ (1/4)[2 - u]^3, & 1 \le u \le 2, \\ 0, & u \ge 2. \end{cases}
$$

$$\tilde{W}_{\mathrm{sph}}(k; R_h) = \frac{12}{(kR_h)^5}\left\{-2\sin(kR_h) + \sin(2kR_h) + k^{-1}[6 - 8\cos(kR_h) + 2\cos(2kR_h)]\right\},$$

$$\approx 1 - \frac{13}{84}(kR_h)^2 \text{ as } k \to 0. \tag{2.9}$$

This smoothing function is widely used in smooth particle hydrodynamics, following Monaghan (1985) and Monaghan & Lattanzio (1985). Out to $3R_h^{-1}$ in k, a Gaussian fit to the Fourier transform is excellent: matching $\tilde{W}_{\mathrm{sph}}$ to $\tilde{W}_G$ in the neighborhood of $k = 0$ gives $R_G = 0.556\,R_h$, while matching where $\tilde{W}_{\mathrm{sph}}$ falls by $1/e$ gives the almost identical $0.561\,R_h$.

Following BBKS, we introduce the variances

$$\sigma_{fj}^2(R_f) \equiv \int \frac{d^3k}{(2\pi)^3} k^{2j} P_F(k) \tilde{W}_f^2(k; R_f), \qquad f = \text{G, TH, } k, \text{ sph, } \cdots \tag{2.10}$$

$$\gamma_f \equiv \frac{\sigma_{f1}^2}{\sigma_{f0}\sigma_{f2}}, \qquad \gamma_{fv} \equiv \frac{\sigma_{f0}^2}{\sigma_{f-1}\sigma_{f1}}, \qquad R_{f*}(R_f) \equiv \frac{\sqrt{3}\,\sigma_{f1}}{\sigma_{f2}}, \tag{2.11}$$

which are, of course, dependent upon the type of filtering. For example, we normalize linear density spectra by parameterizing its overall amplitude by the value of $\sigma_8 \equiv \sigma_{\mathrm{TH}0}(8h^{-1}\mathrm{Mpc})$. The "biasing" factor is $b_8 \equiv \sigma_8^{-1}$. We shall also have occasion to use mixed-filtering (top hat plus Gaussian) and half-filtering quantities:

$$\sigma_{f'f,j}^2(R_{f'}, R_f) \equiv \int \frac{d^3k}{(2\pi)^3} k^{2j} P_F(k) \tilde{W}_{f'}(k; R_{f'})\tilde{W}_f(k; R_f), \qquad f, f' = \text{G, TH, } k, \text{ sph}, \tag{2.12}$$

$$\gamma_{f'f} \equiv \frac{\sigma_{f'f,1}^2}{\sigma_{f'0}\sigma_{f2}}, \qquad \gamma_{f'fv} \equiv \frac{\sigma_{f'f,0}^2}{\sigma_{f'-1}\sigma_{f1}}, \tag{2.14}$$

$$\sigma_{hf,j}^2(R_f) \equiv \int \frac{d^3k}{(2\pi)^3} k^{2j} P_F(k) \tilde{W}_f(k; R_f), \qquad f = \text{G, TH, } k, \text{ sph}, \ldots. \tag{2.13}$$

Thus $\sigma_{ff,j} \equiv \sigma_{fj}$.

2.1.2. *Linear Displacements and Tides*

The field quantities that must be specified at a point r_{pk} for it to be the site of a peak of the smoothed density field $F(r, t; R_f)$ are the gradient $\nabla_i F$, which must vanish, and the second derivative tensor $\nabla_i\nabla_j F$, which must be negative definite. BBKS considered properties of peaks as a function of the height $F(r_{\mathrm{pk}}, t; R_f)$ and these derivatives. However, although $\nabla_i F$ and $\nabla_i\nabla_j F$ do play a role in determining the core properties of the peak, it should not be surprising that it is the expansion of the smoothed displacement field $s(r)$ about the peak which is more fundamental to the dynamics than is the local expansion of F, since it is s that defines the initial flow pattern for the region about the peak through the Zeldovich approximation.

We write the displacement as $s = s_b + s_f$, where s_b is smoothed over a large-scale $R_f = R_{\mathrm{pk}}$ and s_f is the residual. It is convenient to consider the "fluctuating" field to be statistically independent of the "background" field, which occurs if the filter is a sharp k-space one, k_b^{-1}. It should be some factor times R_{pk}, but exactly which factor depends upon the application we have in mind. The choice of filter also depends upon the application. For example, we use Gaussian filtering on the density field to do peak finding in § 4, but use top-hat filtering with $R_{\mathrm{TH}} = R_{\mathrm{pk}}$ to evaluate the smoothed displacement field and internal peak-patch properties. In the immediate neighborhood of the peak, the "background" field s_b is completely specified by a bulk peak displacement s_{pk} and a peak strain, $e_{\mathrm{pk},ij}$:

$$s_{bi}(r) \approx s_{\mathrm{pk},i} - \sum_j e_{\mathrm{pk},ij}(r - r_{\mathrm{pk}})_i + \cdots. \tag{2.15}$$

where the "background" (perturbed) strain field is

$$e_{b,ij} \equiv -\frac{1}{2}\left(\frac{\partial s_{bi}}{\partial r_j} + \frac{\partial s_{bj}}{\partial r_i}\right)(r) \tag{2.16}$$

and $e_{\mathrm{pk},ij} \equiv e_{b,ij}(r_{\mathrm{pk}})$. The residual fluctuating field s_f, predominantly made up of spatial wavenumber components higher than R_{pk}^{-1}, is important for determining substructure and merging times and will influence the overall collapse time. Even so, s_{pk} and $e_{\mathrm{pk},ij}$ should be fundamental for determining gross features of the evolution.

In linear theory, the smoothed peculiar velocity of the peak is $V_{\mathrm{pk}} = -aH_D s_{\mathrm{pk}}$. It obeys $\dot{V}_{\mathrm{pk}} + HV_{\mathrm{pk}} = g_{\mathrm{PL}}$, where the smoothed peculiar gravitational acceleration is $g_{\mathrm{PL}} = -4\pi G\bar{\rho}_{\mathrm{nr}}\bar{a}(t)s_{\mathrm{pk}}$. Here $\bar{\rho}_{\mathrm{nr}}$ is the mean background density of nonrelativistic particles (the matter which can cluster). We separate the peak strain into its trace, the smoothed linear (relative) overdensity of the peak,

$$F_{\mathrm{pk}} = -e^i_{\mathrm{pk},i} = [\nabla \cdot s_b](r_{\mathrm{pk}}) \tag{2.17}$$

and its anisotropic part,

$$e'_{\mathrm{pk},ij} = e_{\mathrm{pk},ij} + \tfrac{1}{3}F_{\mathrm{pk}}\delta_{ij} . \tag{2.18}$$

The anisotropic shear tensor is just the time derivative of the anisotropic strain, $\dot{e}'_{\mathrm{pk},ij}$, and the relative volume dilation rate is $\dot{e}^i_{\mathrm{pk},i} = -H_D F_{\mathrm{pk}}$. In linear theory, the smoothed peculiar tidal field acting on the peak patch is also proportional to $e_{\mathrm{pk},ij}$:

$$T_{L,ij} = -4\pi G\bar{\rho}_{\mathrm{nr}}e_{\mathrm{pk},ij} . \tag{2.19}$$

(The peculiar tidal field is defined by $T_{ij} \equiv \partial^2\Phi_P/\partial X^i \partial X^j$, where Φ_P is the peculiar gravitational potential [see Appendix A]. In the linear regime, $s_{bj} = [4\pi G\bar{\rho}_{\mathrm{nr}}\bar{a}^2]^{-1}\partial\Phi_P/\partial r^j$.)

The strain tensor $e_{\mathrm{pk},ij}$ can be expanded in eigenvalues λ_{vA} and unit vectors $\hat{n}_{vA}$ which specify the principal axes of the tensor:

$$e^{ij}_{\mathrm{pk}} = -\sum_{A=1}^{3} \lambda_{vA}\hat{n}^i_{vA}\hat{n}^j_{vA} , \tag{2.20a}$$

$$\lambda_{v3} = (F_{\mathrm{pk}}/3)(1 + 3e_v + p_v) , \tag{2.20b}$$

$$\lambda_{v2} = (F_{\mathrm{pk}}/3)(1 - 2p_v) , \tag{2.20c}$$

$$\lambda_{v1} = (F_{\mathrm{pk}}/3)(1 - 3e_v + p_v) . \tag{2.20d}$$

The eigenvalues are arranged so that $\lambda_{v3} \geq \lambda_{v2} \geq \lambda_{v1}$. Thus it is along the 3-axis that collapse will first occur. The λ_{vi} can be parameterized in terms of the height of the peak $v_{\mathrm{pk}} = F_{\mathrm{pk}}/\sigma_0(R_{\mathrm{pk}})$ and the shear ellipticity e_v and prolaticity p_v as indicated. The ordering constraint restricts $e_v \geq 0$ and $-e_v \leq p_v \leq e_v$. The remaining three coordinates required to fix the symmetric tensor $e_{\mathrm{pk},ij}$ are the Euler angles which describe the orientation of the orthonormal triad $\hat{n}_{vA}$. The anisotropic strain tensor $e'_{\mathrm{pk},ij}$ has eigenvalues $\lambda'_{vi} \equiv \lambda_{vi} - F_{\mathrm{pk}}/3$ which sum to zero.

In the principal axis system, the smoothed linear evolution in the neighborhood of the peak point is $X_A - X_{\mathrm{pk},A} \approx \bar{a}(t)[1 - \lambda_{vA}(t)](r_A - r_{\mathrm{pk},A})$. Therefore, the local effect of the long-wavelength fields upon an initially spherical region of Lagrangian space will be to distort it into a collapsing homogeneous ellipsoid, whose principal axes are those of $e_{\mathrm{pk},ij}$, as the patch moves with velocity V_{pk}. Of course, the dynamics of a peak patch is much more complex because of the spatial variation of s_b and the complex structure of s_f. The homogeneous ellipsoid picture may be thought of as a tensor virial theorem approach to the average interior dynamics. The first approach we took to the dynamics in Bond & Myers (1991) was a spherical approximation (e.g., Gunn & Gott 1972; Gott & Rees 1975), which has the advantage of allowing inhomogeneous radial distributions to be explicitly treated. Although the ellipsoid approach is obviously imperfect, we feel it is very important to at least crudely take into account the long range shear field within which the peak-patch resides.

2.1.3. Homogeneous Ellipsoidal Collapse of a Patch

We derive the dynamical equations for the ellipsoid in a cosmological setting in detail in Appendix A. We show that one must be very careful with the external tidal fields to ensure that linear theory is reproduced. For illustration, we give the results for the case when the Universe has only nonrelativistic matter present, with background mass density $\bar{\rho}_{\mathrm{nr}}$, and no mean curvature, so $\Omega = \Omega_{\mathrm{nr}} = 1$. (In Appendix A, we pay special attention to the corrections necessary if there is mean curvature or if there is a nonzero cosmological constant.) The boundary of the Lagrangian sphere of radius R_{pk} evolves as $X_i(t) = a_i(t)R_{\mathrm{pk}}$, where the a_i are the scale factors for the three principal axes of the ellipsoid. The equations we solve for $X_i(t)$ are

$$\frac{d^2}{dt^2}X_i = -4\pi G\bar{\rho}_{\mathrm{nr}}X_i\left[\frac{1}{3} + \frac{\delta_{\mathrm{nr}}}{3} + \frac{b'_i}{2}\delta_{\mathrm{nr}} + \lambda'_{vi}(t)\right] . \tag{2.21}$$

Here the relative overdensity of the nonrelativistic matter is

$$\delta_{\mathrm{nr}} \equiv \delta\rho_{\mathrm{nr}}/\bar{\rho}_{\mathrm{nr}} \equiv \frac{\bar{a}^3}{a_1 a_2 a_3} - 1 , \tag{2.22}$$

where $\delta\rho_{nr} \equiv \rho_{nr} - \bar{\rho}_{nr}$. The factors

$$b'_j(t) \equiv b_j(t) - \frac{2}{3}, \text{ where } b_j(t) \equiv a_1(t)a_2(t)a_3(t) \int_0^\infty \frac{d\tau}{[a_j^2(t) + \tau]\prod_{m=1}^3 [a_m^2(t) + \tau]^{1/2}} \tag{2.23}$$

are familiar from the potential theory for homogeneous ellipsoids (e.g., Chandrasekhar 1969; Binney & Tremaine 1987). The initial conditions at time t_0 for these equations are obtained using a Zeldovich approximation setup:

$$X_i(t_0) = \bar{a}(t_0)R_{pk}[1 - \lambda_{vi}(t_0)], \qquad \dot{X}_i(t_0) = V_i(t_0) = H(t_0)X_i(t_0) - \bar{a}(t_0)H_D(t_0)\lambda_{vi}(t_0). \tag{2.24}$$

We stop collapse along axis i by simply freezing a_i once a critical radius $a_{eq,i} = f_r\bar{a}$ is reached during the infall phase. The redshift $z_{c,1}$ at which the last axis of the ellipsoid (1-axis) freezes out, which we take as our indicator of "virialization," is quite insensitive to the specific value of f_r. The radial freezeout factor $f_r = 0.18$ was chosen, since it turns out to reproduce the "virial" density contrast of 179 familiar from spherical top-hat calculations. We describe this in much more detail in Appendix A. We tabulate $1 + z_{c,1}$ as a function of the parameters e_v and p_v for a given F_{pk}. For $\Omega_{nr} = 1$, $1 + z_{c1}$ scales with F_{pk} (since $D = \bar{a}$), hence in that case we only need an $e_v - p_v$ table. One of the main features is that once the 3-axis collapses, the nonlinear density contrast causes the other two axes to collapse much more rapidly than linear theory would predict. Indeed, collapse along all three axes is possible even if $\lambda_{v1} < 0$. For illustration, the redshifts of collapse for a perturbation with current linear overdensity $F = 2$ are plotted in Figure 1 as a function of shear ellipticity e_v for a CDM model. The collapse redshifts scale as $(1 + z) \propto F$ as F changes for this $\Omega_{nr} = 1$ Einstein–de Sitter case. These results are compared with the predicted collapse redshift in the Zeldovich approximation, which does not fare well at all. Only in the limit of very large e_v does the collapse redshift along the 3-axis approach that given by the Zeldovich approximation. And once one axis goes to nearly zero size, the gravitational attraction on the other axes becomes so large that collapse occurs very shortly after on the other two axes. The Zeldovich approximation does not come close to describing this accelerated evolution, whose origin is from nonlinear internal tidal effects that it ignores. If $e_v > 0.33$, λ_{v1} is negative, but full collapse can still occur.

In the spherical approximation to dynamics, the exterior anisotropic tidal force is taken to be zero and $b'_j(t) = 0$, so equation (2.21) reduces to $\ddot{X}_i = -(4\pi G/3)\bar{\rho}_{nr}(1 + \delta_{nr})X_i$, giving the usual cycloid solution for a closed universe. The equation is, of course, valid for an arbitrary interior radial profile provided spherical symmetry holds. The usual practice is to integrate each shell until it reaches zero radius, then to say that the mass is redistributed at that point into a virial structure. For the $\Omega_{nr} = 1$ model, this occurs when the linear overdensity $F_{pk}(t)$ reaches the familiar critical value $f_c = 1.686$. The value of f_c must be computed for more complicated cosmologies. The homogeneous ellipsoid solutions with $e_v \neq 0$ require larger values for $F_{pk}(t)$ than f_c.

To put the ellipsoidal collapse approximation into effect in the calculation of R_{pk}, we need to calculate the mass-averaged strain in the peak patch. Consider integration over a Lagrangian volume V with bounding surface element dS with unit normal $\hat{n}_i$. The mass average of e_{ij} is just

$$\langle e_{ij}\rangle_M = -\frac{1}{V} \int dS \frac{1}{2}[s_i(\boldsymbol{r})\hat{n}_j + s_j(\boldsymbol{r})\hat{n}_i]. \tag{2.25}$$

For example, for a Lagrangian sphere, the magnitude of $\boldsymbol{R} = \boldsymbol{r} - \boldsymbol{r}_{pk}$ on the surface is fixed at R, the area is $R^2 d\Omega = R^2 d\mu d\phi$, and the unit normal is $\hat{R}$. Since the angle average of $\hat{R}$ is zero for a sphere, we can subtract an arbitrary constant term from s_i in the above expression. We choose this to be the "bulk" displacement $\bar{s}_{pk,i}$ to explicitly show that it is relative displacement which is relevant:

$$e_{ij}(<R) = -\frac{3}{4\pi R} \int\int d\mu d\phi \frac{1}{2}[\Delta s_i(\mu, \phi)\hat{R}_j(\mu, \phi) + \Delta s_j(\mu, \phi)\hat{R}_i(\mu, \phi)]. \tag{2.26}$$

where

$$\Delta s_i(\mu, \phi) \equiv [s_i(R, \mu, \phi) - \bar{s}_{pk,i}].$$

2.1.4. *Internal Energy of a Patch*

The initial internal energy of the peak-patch (for $\Omega = 1$) is given by

$$\varepsilon_{int}(<R_{pk}) \equiv -\frac{1}{2}v_E^2 = -\frac{1}{2}(H_0 R_{pk})^2 \Omega_{nr} \frac{F_{pk}}{D} S(R_{pk}), \tag{2.27a}$$

where we introduce a dimensionless shape factor (Bond 1988),

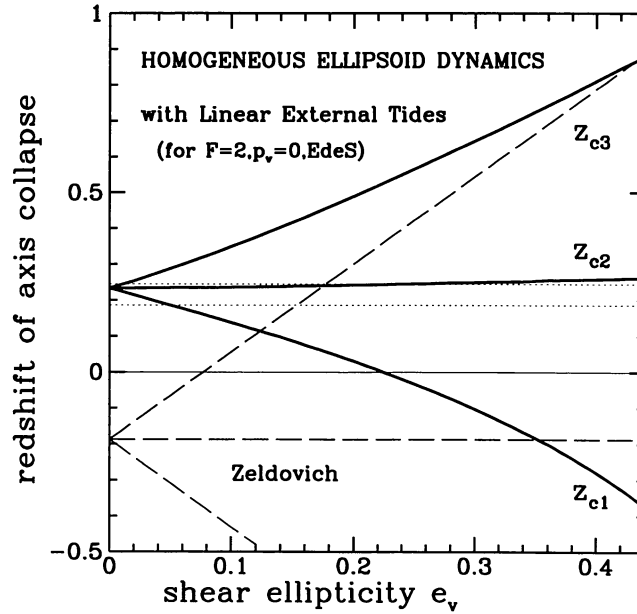$$S(R_{pk}) \equiv (F_{pk}R_{pk}^5)^{-1} \int_0^{R_{pk}} \bar{F}(<R_{TH})dR_{TH}^5, \tag{2.27b}$$

FIG. 1.—The collapse redshifts for the three ellipsoidal axes as a function of the initial ellipticity $e_v = (\lambda_{v3} - \lambda_{v1})/(2F)$, assuming zero prolaticity p_v, linear overdensity now $F = 2$, and our standard linear external tide approximation (*solid line*). We also show when the analytic spherical model reaches overdensity 170 (*upper dotted line*) and complete collapse (*lower dotted line*). The dashed curve shows how poorly the Zeldovich approximation fares: only for extreme elongations does it get the collapse redshift along the 3-axis right, and is very far off for the other two directions.

and $\bar{F}(<R_{TH})$ is the volume-average of the unsmoothed $F(r, t)$ within the Lagrangian sphere of radius R_{TH} from the peak center, i.e., $F(r_{pk}, t; R_{TH})$. This first-order perturbation theory result for ε_{int} is exact irrespective of the inhomogeneity of the peak's density profile and since $F_{pk} \propto D$, it is conserved, irrespective of cosmology.

Further, in the spherical approximation to the dynamics, ε_{int} will be conserved throughout the nonlinear evolution. However, nonlinear tidal effects cause the internal energy to change somewhat for an ellipsoid, so ε_{int} can only serve as an estimate of the binding energy of the final state of the interior. The derivation of this formula, with the effects of curvature and cosmological constant included, and a discussion of the tidal heating/cooling effects are given in Appendix B.

2.2. *Anatomy of a Peak Patch*

In this subsection, we show how varying the density, displacement, and strain field and other constraints affects the linear structure of a peak patch, and illustrate with a simulation of a large cluster how well the gross features of the final collapsed structure are reproduced by ellipsoidal and spherical dynamics. We concentrate on variations of a $\nu_{pk} = 2.45$ peak ($R_G = 5h^{-1}$ Mpc) in a $\sigma_8 = 1$ cold dark matter model ($\Omega_{cdm} = 1$, $h = 0.5$) cosmology. This ν_{pk} value was chosen so that peaks of this mass or above would have an abundance of $10^{-5}/(h^{-1}$ Mpc$)^3$, slightly more than for Abell richness 1 clusters.

The constrained field techniques used are given in Appendix C. The displacement and density fields described are realizations of a Gaussian process with 18 constraints, nine associated with the density, displacement, and anisotropic strain, and nine more associated with $\nabla_i F$ and $\nabla_i \nabla_j F$. The peak constraint is $\nabla_i F = 0$ and $\nabla_i \nabla_j F$ negative definite. On average, the principal axes for $\nabla_i \nabla_j F$ align with those for $e_{pk,ij}$, but considerable misalignment is statistically probable. The analogs of ν_{pk}, e_v, p_v for the tensor $\nabla_i \nabla_j F$ are x_{pk}, where $x = -\nabla^2 F/\sigma_2$ is a measure of the angle-averaged curvature of the smoothed peak profile, and e_d and p_d, which together measure how oblate or prolate it is (BBKS). For the simulation, statistically averaged values were given for the constraint quantities: $e_v = 0.136$, $p_v = 0.0085$, $x_{pk} = 2.56$, $e_d = 0.175$, $p_d = 0.011$, which gives a flavor for the expected magnitudes. Principal axis alignment was also chosen. In addition, the peak was chosen to be moving with the one-dimensional rms velocity of peaks.

We have used an SPH code with a multigrid Gauss-Seidel potential solver to evolve 17,077 gas particles and 17,077 dark particles (with $\Omega_{cdm} = 0.95$ and a baryon density of $\Omega_B = 0.05$). We have also used a tree code to perform a purely collisionless simulation of just the 17,077 dark particles (with $\Omega_{cdm} = 1$). The two simulations of the same constrained field initial conditions give very similar results for the gross features, as expected since the dynamical evolution is dominated by the dark matter.

For this peak patch, the spherical model predicts a collapse redshift of $z = 0.1$, while the ellipsoidal model predicts collapse occurs along the 3-axis at $z_{c3} = 0.3$, along the 2-axis at $z_{c3} = 0.14$, along the 1-axis at $z_{c1} = 0.04$. The simulations show a major merger between redshift 0.2 and 0.04: two groups of $3.5 \times 10^{14} h^{-1} M_\odot$ and $4 \times 10^{14} h^{-1} M_\odot$ at $z = 0.2$ formed a single cluster with $1.2 \times 10^{15} h^{-1} M_\odot$ at $z = 0.04$. The spherical and ellipsoidal models predict masses of $1.34 \times 10^{15} h^{-1} M_\odot$ and $1.07 \times 10^{15} h^{-1} M_\odot$, respectively, using the empirical relationships between R_{pk} and R_G (see Fig. 10 below). The internal energy (as measured by v_E, eq. [2.27a]) for both the spherical and ellipsoidal collapse models is predicted to be 1540 km s^{-1}, while the tree code gives 1550 km s^{-1}

at $z = 0.04$. (We also find that the velocity dispersion as estimated from the cluster kinetic energy is 17% higher, whereas isolated virial equilibrium would suggest equality, a point we return to in BM2.) Overall, the agreement between the collapse characteristics of the simulations and the predicted time, mass, and energy from the peak patch approximation are encouraging. However, other realizations of the initial conditions with the same constraints could lead to earlier mergers or a delay in merging of subclusters: identifying the bulk Gaussian peak properties can obviously not fully specify the fate.

We now take the 2.45σ density peak example and show what happens to the linear density and displacement field in and around a peak patch when we vary the shear eigenvalues and velocities and also the realizations that define the substructure. The results of this exercise are shown graphically in Figures 2, 3, 4, and 5.

We find it conceptually useful to separate the construction into three pieces, $s = \bar{s}_b + \Delta s_b + s_f$. s_f is a fluctuating field which consists of unconstrained wavenumber components of the field with high wavenumber. The longer wavelength background field $s_b = \bar{s}_b + \Delta s_b$ is naturally split into two parts, a mean background displacement $\bar{s}_b$ and a random field deviation from the mean Δs_b. Similarly F has $\bar{F}_b$, ΔF_b, and F_f pieces. So that the long-wavelength influence could be seen clearly in the density contours in the figures shown here, waves were only added to the fluctuating field down to $k^{-1} = 1\ h^{-1}$ Mpc; otherwise the contours become quite jumbled through uncorrelated short distance power.

Figure 2 isolates the individual components that contribute to the total peak-patch fields shown in Figure 2d. The linear density is the contour map and the peculiar velocity field is denoted by arrows. (The standard convention for the displacement field makes
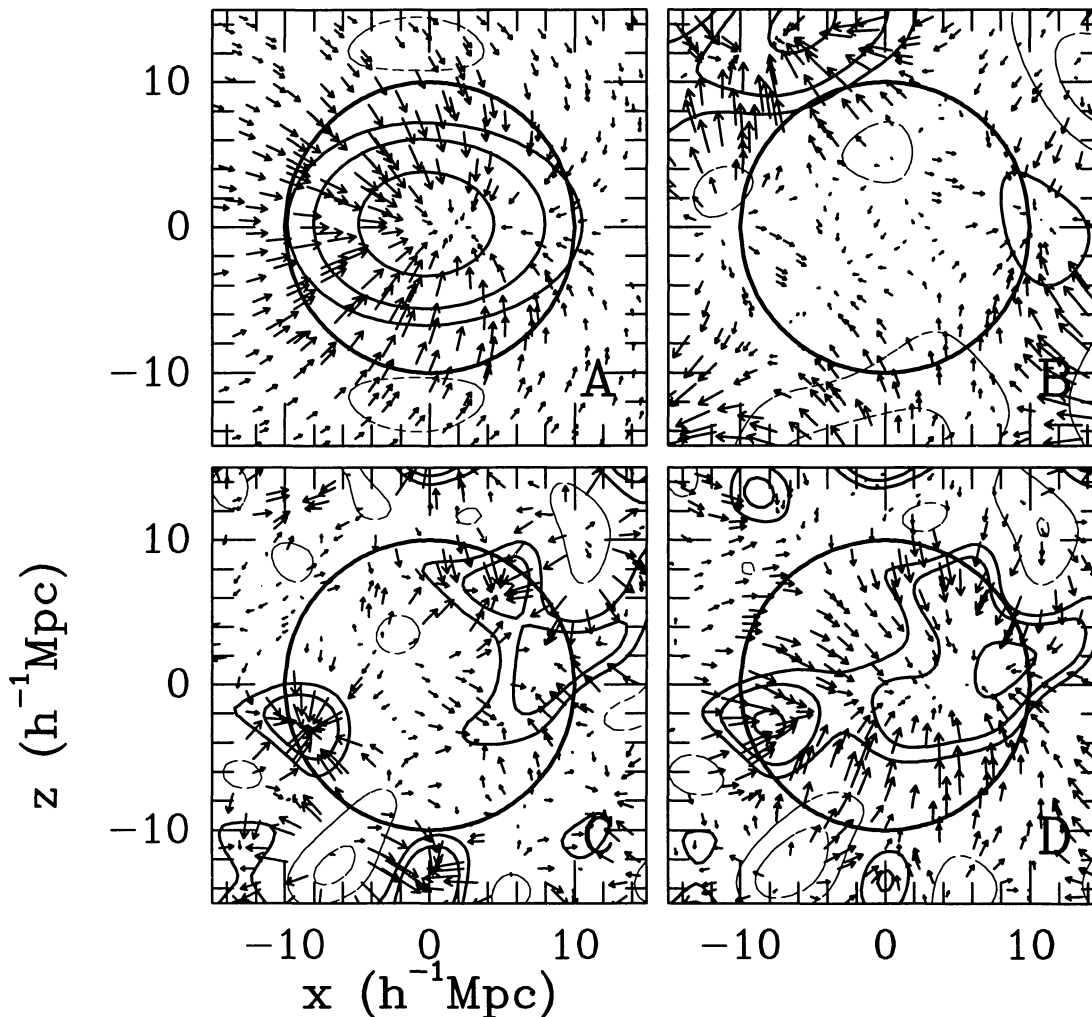

FIG. 2.—The first three panels show the individual elements that make up peak-patch linear density (*contours*) and peculiar velocity (*arrows*) fields: (*a*) the background mean-field, (*b*) the background variance field, which is extremely quiescent in the neighborhood of the peak, and (*c*) the short-distance fluctuating field responsible for subclumps within the medium. (*d*) is the sum total peak-patch field. In (*a*) and (*b*), the contours increase by factors of 2 from the minimum contour at $f_c/2$, where $f_c = 1.686$ is the critical contour for spherical "top-hat" collapse. The light lines denote negative contours. The displacement field arrows are scaled for appearance, and only one in 12 are sampled. Panels (*c*) and (*d*) start at the f_c contour level for positive (dark) densities and at $2f_c$ for negative ones. The peak was constrained to have $\nu_{pk} = 2.45$, $e_{v,pk} = 0.14$, $v_{1,pk} = 0.46\ \sigma_v$ when Gaussian-smoothed over $5h^{-1}$ Mpc. The circle at $10h^{-1}$ Mpc is the average R_{pk} associated with Gaussian-peaks at this filter scale, but substantial variance is expected.
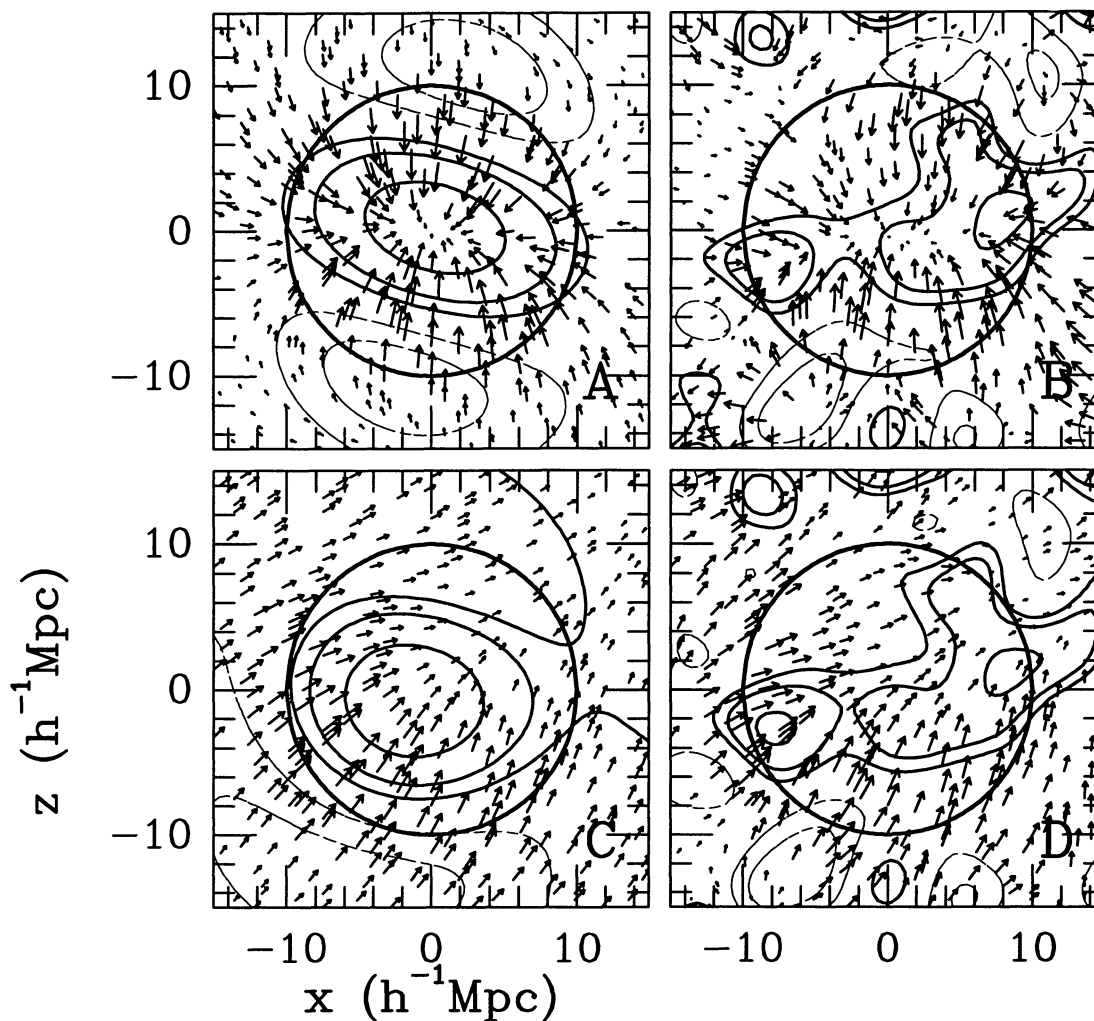
FIG. 3.—Panels (a) and (b) show the mean background and total constrained fields for a case with shear ellipticity $e_{vpk} = 0.27$, near the outside range for peaks of this height. (Contouring choices are the same as in the previous figure.) Increasing the shear further deepens the holes on either side of the "pancake" plane. The peak has a velocity of 0.8 σ_v, the rms for peaks of this scale, but it is moving in the 2-direction so one cannot see its influence. Panels (c) and (d) illustrate the effect of giving the peak a high velocity. It is moving at a speed of 2.26 σ_v toward the upper right at 45°. This is a 2.8 σ fluctuation for peaks (which have lower velocities than field points do, by 20% in this case). Note the stretching of the density contours in that direction as well. Although the flow pattern of (d) looks quite different than in (b), once the mean flow for the box is subtracted, the pattern is actually reasonably similar, emphasizing that it is the strain which dominates the local dynamics.

it of opposite sign to the peculiar velocity field.) Figure 2a shows the background mean-field; Figure 2b, the background variance field; and Figure 2c, the uncorrelated fluctuating field. The short-distance fluctuating field is responsible for the formation of subclumps. The background field lifts them up or down. The background-variance field is essentially flat without flows within the radius of the circle at $2R_G$. This is because we have specified enough constraints that the field is essentially fully specified over a smoothing scale, and that field is given by the mean-field. The background-variance field is also, of course, a total background field—one for the constraints of no smoothed density contrast, no velocity, no shear, no density gradient, vanishing $\nabla_i \nabla_j F$. That is why it is so quiescent in the neighborhood of the peak.

The contours are in units of $f_c = 1.686$, the linear overdensity required for complete collapse in the spherical model. The minimum positive contour is f_c in all figures except those that show the mean background or background-variance field, where a $f_c/2$ contour is also included. The fluctuating field adds a relatively large amplitude, so to make the pictures that include it less confusing, we chose $2f_c$ to be the first negative contour. This still shows where the deep voids are. The first negative contour for the background-only cases is $f_c/2$. It is apparent from this figure that the mean field gives an adequate representation if one is interested in phenomena in the immediate neighborhood of the peak, provided enough constraints are imposed. (The realization shown here is *not* the same as for the simulation, which had fewer grid points but went out to 30 h^{-1} Mpc.) The circle at 10 h^{-1} Mpc is the average R_{pk} associated with Gaussian peaks at this filter scale.

The strong role that values of the anisotropic shear and the bulk flow have on the surroundings of peaks had not been emphasized very much before this work. (Bond (1987b) described the effects of shear on peaks, but within the Zeldovich approximation, and
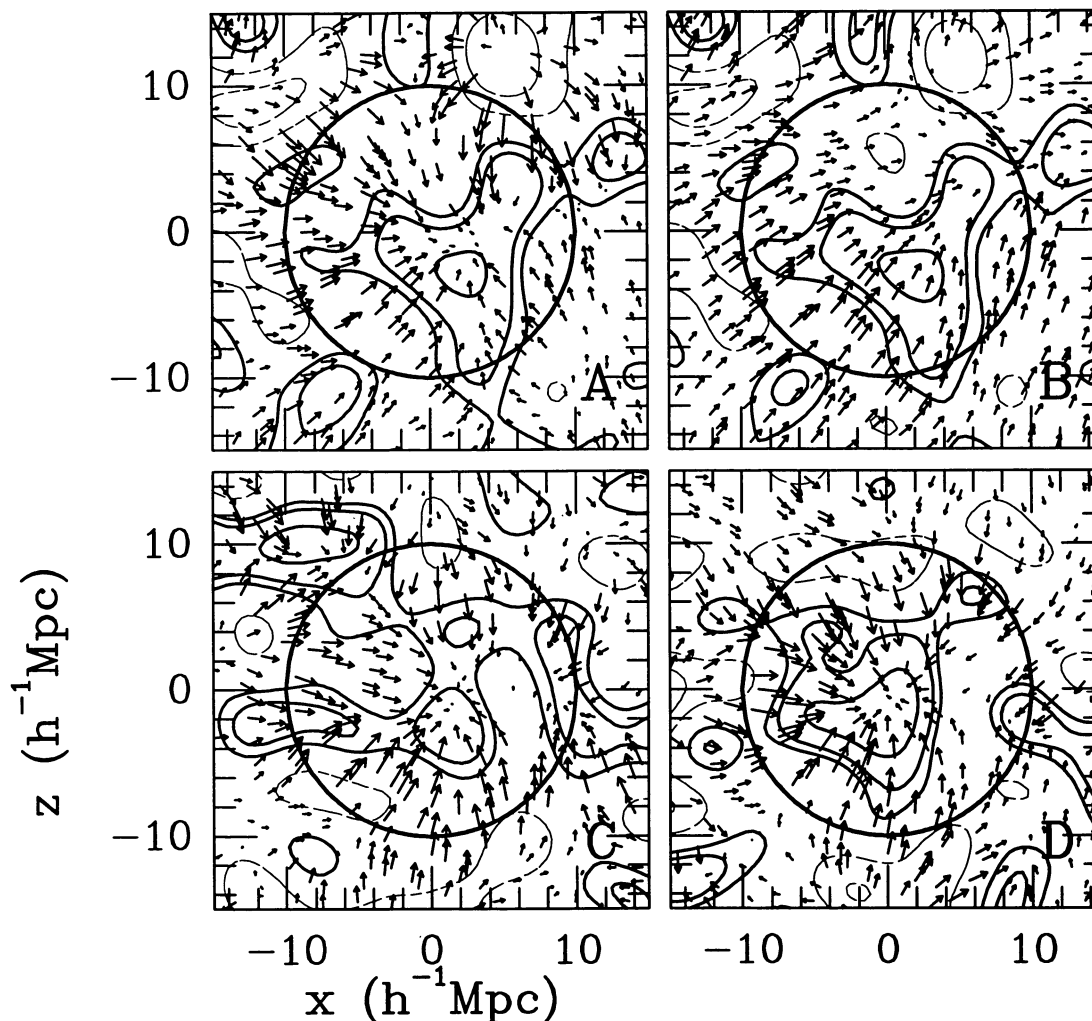
FIG. 4.—Panels (a), (c), and (d) show three realizations with the same mean peak constraints, demonstrating how sensitive merger history will be to variations in the fluctuating field. Contours increase by factors of 2 from $f_c = 1.686$ for positive (dark) densities and from $2f_c$ for negative ones. Panel (c) has the same background-variance field as in Fig. 1, but a different fluctuating field realization. Panel (b) has the peak moving at 2.26 σ_v as in Fig. 3d, but for a different realization, the same as for panel (a). There is still a strong resemblence to the Fig. 3d realization. Note that the displacement field can look rather different from what one would infer from local density contours, because long wavelengths must conspire to give both the anisotropic shear and mean flow of the Gaussian-smoothed fields.

Dubinski & Carlberg (1991) included linear "external" tides in their N-body study of forming galaxy halos, but did not impose self-consistency with the internal strain.) The effects are shown in Figure 3. Figures 3a and 3b show the mean background and total constrained fields, respectively, for a peak with large ellipticity, $e_v = 0.27$. about twice the statistically averaged value, and a rms bulk velocity for peaks of $0.8\sigma_v$. The principal axes of $\nabla_i\nabla_j F$ are rotated relative to those for e_{ij}, to show the effect of slight misalignment. Figures 3c and 3d show the effect of greatly increasing the speed, to $2.26\sigma_v$, while dropping e_v back to 0.14. The velocity field shows large scale coherence, as expected. However, when we remove the box-averaged flow the remainder looks relatively similar to Figure 2d. Thus, in the frame of the bulk flow, the ellipsoidal approximation should work reasonably well.

Figure 4 confirms the very strong influence that the "short-distance" fluctuating field has in creating a large range of possibilities even given the specification of the average peak-patch parameters. Figures 4a, 4c, and 4d are three different realizations of the case shown in Figure 2d. Figure 4b is a different realization of the high-speed peak of Figure 3d. It is primarily scales not too far below that of the Gaussian filter that determine the major pieces of substructure. It is a statistical question whether these subclumps will add to the background field to enhance the likelihood of collapse, or whether subvoids can destructively interfere enough to delay collapse. The density lumps outside the cluster are the candidates for groups that merge with the forming cluster. For example, the fluctuating field in Figure 4c happened to have three clumps near the edge of the circle. Upping the density enhancement within the peak-circle bridged the sumlump contours. The expectation is that the three sublumps will form smallish clusters as will the central enhancement and these will all merge at some future point. Thus, although we have imposed a specific peak constraint at the origin, a larger scale peak at a slightly different location is the more "dynamically correct" entity which subsumes our original
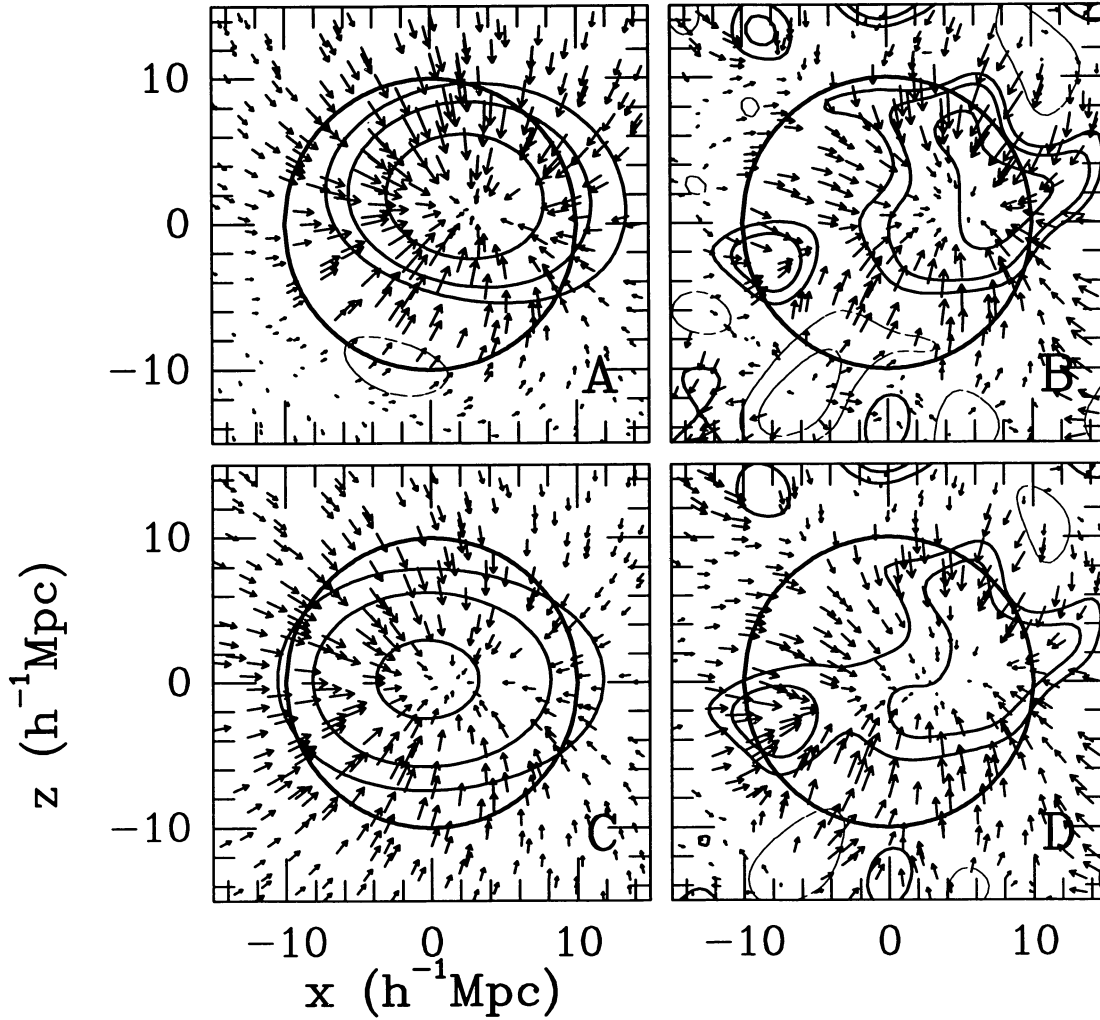
FIG. 5.—Panels (a) and (b) show the mean background field and the total constrained field for the standard realization and standard parameters, except instead of the peak constraint, $\nabla_i F$ was given a 1 σ value directed along the $z = x$ line. Panels (c) and (d) are for a rare peak of height $\nu_{pk} = 3.43$ in a model with $\sigma_8 = 0.71$, which suppresses the background variance and fluctuating fields relative to the mean background field shown in (c). Except for this suppression, the standard realization of Fig. 1 has been adopted.

peak and the neighboring subclumps. Finding these dynamically correct peaks among all the peaks is what our hierarchical method is designed to do.

In Figures 5a–5b, we show the significance of the peak constraint, $\nabla F_{pk} = 0$ by constraining ∇F to have a nonzero value at the origin. Not surprisingly, the flow is away from the origin, converging to where $\nabla F_{pk} = 0$. Figures 5c and 5d show what a rare $\nu_{pk} = 3.43$ peak looks like. The higher peak leads to a more extended profile and the background variance and fluctuating fields are suppressed, so the mean background field has a larger control over the nature of the contours and flow field.

3. THE PEAK PATCH CATALOG

The state at time t of the objects (groups) in a catalog at positions x_g with peculiar velocities V_g is fully characterized by a distribution function:

$$f_{gp}(x, v, M, \varepsilon_{int}, t) = \sum_g \delta^{(3)}(x - x_g)\delta^{(3)}(V - V_g)\delta(\ln M - \ln M_g)\delta(\varepsilon_{int} - \varepsilon_{int,g}) . \tag{3.1}$$

As sample internal properties we take the mass M_g and the internal (binding) energy per unit mass $\varepsilon_{int,g}$ of the individual groups, since these are the ones we focus on in this paper. The associated point process integrates over the peculiar velocities:

$$n_{gp}(x, M, \varepsilon_{int}, t) = \sum_g \delta^{(3)}(x - x_g)\delta(\ln M - \ln M_g)\delta(\varepsilon_{int} - \varepsilon_{int,g}) . \tag{3.2}$$

One generally compares catalogs through their low-order statistics. Examples of these are various "one-point" functions, including the mass function of bound groups

$$\bar{n}_{\mathrm{gp}}(M, t)d\ln M = d\ln M \int_{-\infty}^{0} d\varepsilon_{\mathrm{int}}\langle n_{\mathrm{gp}}(x, M, \varepsilon_{\mathrm{int}}, t)\rangle \qquad (3.3)$$

and the integrated internal binding energy distribution,

$$\bar{n}_{\mathrm{gp}}(>v_E, t) = \int d\ln M \int_{-\infty}^{-v_E^2/2} d\varepsilon_{\mathrm{int}}\langle n_{\mathrm{gp}}(x, M, \varepsilon_{\mathrm{int}}, t)\rangle . \qquad (3.4)$$

We have translated the internal binding energy distribution into one for a velocity v_E defined by $\varepsilon_{\mathrm{int}} = -v_E^2/2$. This will indeed be the velocity dispersion of the group provided it is relatively isolated and in virial equilibrium.

The detailed implementation of our approach is described in the next section. Here we put the approach into a more formal context. Our goal in the hierarchical peaks method is to determine from the initial conditions only an (Eulerian space) distribution function

$$f_{E,\mathrm{hpk}}(x, V, M, \varepsilon_{\mathrm{int}}, t) = \sum_{\mathrm{hpk}} \delta^{(3)}(x - x_{\mathrm{hpk}})\delta^{(3)}(V - V_{\mathrm{hpk}})\delta(\ln M - \ln M_{\mathrm{hpk}})\delta(\varepsilon_{\mathrm{int}} - \varepsilon_{\mathrm{int,hpk}}), \qquad (3.5)$$

which should be a reasonable approximation to the group distribution function that an N-body simulation would find and relatively easy and fast to calculate. Critical to solving the cloud-in-cloud problem is to develop a merging algorithm in which (Lagrangian space) clouds enveloped by other (Lagrangian space) clouds are excluded from the final hierarchical peaks list, and those that are overlapping are in some way merged. Such an operation on a set of candidate points will be highly nonlocal. The candidate points, however they are selected, must, at the very least, include all of the peaks that survive exclusion and merging, and may include many more points besides.

3.1. *Selection and Exclusion of Lagrangian Peaks*

Our standard algorithm is to choose a large number of Gaussian filter scales, and, for each Gaussian filter in turn, find all peaks of the smoothed density field $F(r; R_f)$ (evaluated at the present time) that lie above some chosen threshold, $F(r_{\mathrm{pk}}; R_f) > f_t$. For $\Omega = \Omega_{\mathrm{nr}} = 1$ cold dark matter models, we usually take $f_t = 1.686/D(z_{\mathrm{pk}})$, where $D(z)$ is the linear growth factor for the fluctuations and z_{pk} is the redshift of the peak, determined by how far away the peak is from "here and now," the global origin of the catalog we wish to construct. The factor 1.686 is the linear factor required for a spherical top-hat perturbation to have collapsed to a point.

The patch around each peak of the unfiltered density field is then measured to determine the *largest* radius R_{pk} of a spherical region in Lagrangian space that will have collapsed by the redshift of the peak. For the spherical approximation to dynamics, this involves measuring the average linear overdensity at a variety of radii, R_{TH}, and converging upon the largest one for which $\bar{F}(<R_{\mathrm{TH}}) = f_c/D(z_{\mathrm{pk}})$, where $f_c = 1.686$ (for $\Omega = \Omega_{\mathrm{nr}} = 1$ models). In the homogeneous ellipsoid approximation to the dynamics, we measure the average strain tensor [and hence $\bar{F}(<R_{\mathrm{TH}})$, e_v, p_v], within an estimated Lagrangian radius R_{TH}, use a table to check whether the ellipsoid with these parameters will have collapsed by the redshift in question, then increase or decrease R_{TH} until the measured shear is such that collapse just occurs, and so define R_{pk}. The mass of the peak (in nonrelativistic particles, that is, those which cluster) is then

$$M_{\mathrm{pk}} = \tfrac{4}{3}\pi\bar{\rho}_{\mathrm{nr}}\bar{a}^3 R_{\mathrm{pk}}^3 . \qquad (3.6)$$

The binding energy estimation $\varepsilon_{\mathrm{int}}$ and the mass-averaged displacement field s_{pk} within the patch of radius R_{pk} are then calculated. The result is a distribution function for the candidate point process determined in "Lagrangian space":

$$f_{L,\mathrm{pk}}(r, s, R, \varepsilon_{\mathrm{int}}, t) = \frac{1}{(H_D\bar{a})^3} \sum_{\mathrm{pk}} \delta^{(3)}(r - r_{\mathrm{pk}})\delta^{(3)}(s - s_{\mathrm{pk}})\delta(\ln R^3 - \ln R_{\mathrm{pk}}^3)\delta(\varepsilon_{\mathrm{int}} - \varepsilon_{\mathrm{int,pk}}) . \qquad (3.7)$$

We have chosen the normalization so that equation (3.7) has the same "dimensions" as equation (3.5). (Recall that in linear theory, the peculiar velocity is just $V_p = -H_D\bar{a}s$, hence the displacement field serves the same purpose as velocity in the distribution function.) Note that although we have found the peaks with Gaussian filtering, the averages are over the Lagrangian volume. That is, the local properties are found with top-hat filtering centered on the peak, with the top-hat radius being adjusted until one predicts that the region has *just* finished its collapse along the 1-axis.

To describe simple exclusion criteria mathematically, it is convenient to transform the final distribution function $f_{E,\mathrm{hpk}}$ back into Lagrangian space (using $x_{\mathrm{pk}} = r_{\mathrm{pk}} - s_{\mathrm{pk}}$, $V_p(x_{\mathrm{pk}}) = -aH_D s_{\mathrm{pk}}$),

$$f_{\text{L,hpk}}(r, s, R, \varepsilon_{\text{int}}, t) = \frac{1}{(H_D \bar{a})^3} \sum_{\text{hpk}} \delta^{(3)}(r - r_{\text{hpk}}) \delta^{(3)}(s - s_{\text{hpk}}) \delta(\ln R^3 - \ln R_{\text{hpk}}^3) \delta(\varepsilon_{\text{int}} - \varepsilon_{\text{int,hpk}}) . \tag{3.8}$$

The Lagrangian-space number density is the integral of $f_{\text{L,hpk}}$ over velocities and internal energies

$$n_{\text{L,hpk}}(r, R, t) = \int (H_D a)^3 d^3 s \, d\varepsilon_{\text{int}} f_{\text{L,hpk}}(r, s, R, \varepsilon_{\text{int}}, t) = \sum_{\text{hpk}} \delta^{(3)}(r - r_{\text{hpk}}) \delta(\ln R^3 - \ln R_{\text{hpk}}^3) . \tag{3.9}$$

In § 4.1.3, we describe a number of merging operations that transform $f_{\text{L,pk}}$ into $f_{\text{L,hpk}}$. In the simplest version, points of small mass whose Lagrangian regions overlap with the Lagrangian regions associated with points of large mass are excluded and the big ones are left with the same mass. We term this full exclusion. In half-exclusion, only if the small mass point lies within the large mass patch is it excluded; otherwise both points survive and retain their same masses. Half-exclusion can obviously lead to some double-counting of mass. We currently prefer a more complicated binary merging algorithm which divides the Lagrangian volume between two overlapping peaks on the intersection plane between them. This is not so extreme as full exclusion and yet does not overcount mass as the half exclusion prescription can. The full and half-exclusion operations can be described by a simple mathematical expression—the binary algorithm cannot.

We first derive the equation for half-exclusion. If we choose the peak radius increment dR to be small enough, then the quantity

$$-\Delta_R f_{\text{L,pk}} \equiv f_{\text{L,pk}}(r, s, R, \varepsilon_{\text{int}}, t) - f_{\text{L,pk}}(r, s, R + dR, \varepsilon_{\text{int}}, t) \tag{3.10}$$

either has one peak contributing to it or none. That peak will be included in the hierarchical list if it is not located within the Lagrangian regions "belonging" to any of the hierarchical peaks with larger radius; that is, if the action of

$$1 - \mathcal{E}_h(r, R+) \equiv 1 - \sum_{\text{hpk}, R_{\text{hpk}} > R} \chi_{V(R_{\text{hpk}})}(r - r_{\text{hpk}})$$

$$= 1 - \int d^3 r' \int_{\ln R+}^{\infty} d \ln R' \chi_{V(R')}(r - r') n_{\text{L,hpk}}(r', R', t) \tag{3.11}$$

upon $\Delta_R f_{\text{L,pk}}$ gives a nonzero value. Here, $\chi_{V(R')}(r)$ is unity if r is within a sphere of radius R' and zero otherwise, hence $\mathcal{E}_h$ is a half-exclusion operator describing the space occupied by higher mass peaks. A peak that survives its action will be part of the hierarchical list and contribute to the distribution function the term

$$-\Delta_R f_{\text{L,hpk}} \equiv f_{\text{L,hpk}}(r, s, R, \varepsilon_{\text{int}}, t) - f_{\text{L,hpk}}(r, s, R + dR, \varepsilon_{\text{int}}, t) . \tag{3.12}$$

We therefore have the multiplicative equation $\Delta_R f_{\text{L,hpk}} = [1 - \mathcal{E}_h(r, R+)] \Delta_R f_{\text{L,pk}}$, which looks simple except that $\mathcal{E}_h[n_{\text{L,hpk}}]$ is a linear functional of $n_{\text{L,hpk}}$, hence of $f_{\text{L,hpk}}$.

We can solve this "stochastic" equation to get an even simpler form. We assume that we do not count the same point twice in the candidate point distribution function, equation (3.7), since, even if we find the point to be a peak on two filtering scales, the masses we find will be the same so it would appear in the distribution only once. Thus at the point r with $f_{\text{L,pk}}(r, s, R, \varepsilon_{\text{int}}, t)$ nonzero that we are deciding to include or not, $f_{\text{L,pk}}(r, s, R + dR, \varepsilon_{\text{int}}, t)$ will be zero, as will $f_{\text{L,hpk}}(r, s, R + dR, \varepsilon_{\text{int}}, t)$. Therefore a succinct version of the stochastic equation is

$$f_{\text{L,hpk}}(r, s, R, \varepsilon_{\text{int}}, t) = f_{\text{L,pk}}(r, s, R, \varepsilon_{\text{int}}, t)[1 - \mathcal{E}_h(r, R+)] , \tag{3.13}$$

which shows that the exclusion operator is entirely responsible for the mapping from candidate to final point process. Equation (3.13) is easily seen by multiplying each δ-function term in equation (3.7) by zero if it is to be excluded, one if it is to be kept. The ability to rank-order from large to small R, with $\mathcal{E}_h(r, R+)$ dependent only upon those above the current R is crucial for this derivation. Although simple to write, equation (3.13) is not simple to solve fully, except numerically.

Full exclusion satisfies the same kind of functional equation, except with the full-exclusion operator

$$1 - \mathcal{E}_f(r, R) \equiv 1 - \int d^3 r' \int_{\ln R}^{\infty} d \ln R' \chi_{V(R'+R)}(r - r') n_{\text{L,hpk}}(r', R', t) , \tag{3.14}$$

where $V(R' + R)$ imposes the requirement that the candidate point at r_{pk} whose Lagrangian patch has radius R_{pk} does not lie within the radius $R_{\text{hpk}} + R_{\text{pk}}$ of any of the previously selected hierarchical peak points. In the binary technique, if the point lies within R_{hpk} and $R_{\text{hpk}} + R_{\text{pk}}$, we may retain it, but reduce its mass, and also reduce M_{hpk}, thereby allowing modifications to go upward in the hierarchy.

3.2. *Practical Lagrangian Exclusion*

A major obstacle in the Bond (1988) extension of the BBKS formalism to a mass hierarchy was the overcounting of smaller mass objects that would have merged into higher mass ones. In the hierarchical peaks method, the "cloud-in-cloud problem" is solved by having peaks of larger extent annihilate some fraction, if not all, of the volume included in the overlapping peaks of smaller extent. The problem of merging of peaks can be broken into two parts: the partitioning of Lagrangian space so that the same mass elements are not assigned to more than a single peak (exclusion), and the combination of distinct peaks that have moved into superposition in the final state (merging). The Lagrangian exclusion of overlapping peaks is essential in the method, otherwise mass is overcounted and not conserved. The final-state merging, on the other hand, is not crucial to the method, but has observational consequences in clustering and subclustering of objects.

The assignment of overlapping mass elements to individual peaks is a complex one, as the full solution requires knowledge of the evolution well into the nonlinear regime. This, in effect, is what N-body simulations do: parcel the universe into finite mass elements and evolve the configuration. Because we are treating the problem as a local linear process, we can only approximate the mass assignment. There are several simple methods that we consider for the peak Lagrangian merging algorithm.

We break the question into the problem of a single largest (primary) peak overlapping with a number of smaller (secondary) peaks, which all overlap with the primary peak and may or may not be mutually overlapping. For two peaks with centers at r_{pk1} and r_{pk2}, if

$$|r_{pk1} - r_{pk2}| \leq R_{pk1} + R_{pk2},$$

then the two peaks overlap and one must be rejected or a partitioning of mass must occur. We will assume in all merging methods that if the center of the smaller of the two peaks lies within the larger of the two,

$$|r_{pk1} - r_{pk2}| \leq \max(R_{pk1}, R_{pk2}),$$

then the smaller will be discarded in entirety. For more than two overlapping peaks, care must be taken to do the overlap tests and reduction in some sensible order. In general, the situation of chains of overlapping peaks can be dealt with in stages. We consider a rank-ordered list of peaks with centers at Lagrangian positions $\{r_{pk1}, r_{pk2}, \cdots\}$, where all subsequent peaks overlap with the first peak. At this stage we will order the list in decreasing order of (initial) peak mass, $M_{pk1} \geq M_{pk2}$, etc. Thus r_{pk1} is the location of the primary peak, and the rest are secondary peaks. We consider three options:

1. *Full exclusion.*—Throw away all but the primary peak, and assign the full mass as calculated for it as an isolated peak.

2. *Half-exclusion.*—Throw away all secondary peaks whose center lies within the primary peak-patch, and assign it the full mass as calculated for it as an isolated peak. Keep secondary peaks whose center lies outside with their full mass.

3. *Binary exclusion/reduction.*—Form all pairs of overlapping peaks (primary and secondary). For each pair, throw away the smaller of the two if its center lies within the larger peak. Otherwise, reduce the volume of each of the two peaks by partitioning using a plane that contains the circle formed by intersection of the surfaces of the two Lagrangian spheres; i.e., the plane of separation between the spheres. When all pairs have been considered, reduce the Lagrangian radii of all remaining peaks to conform to the reduced masses. This procedure will ensure that no mass element is assigned to more than one peak, but because the reduction is done by pairs, it will overcount regions that are mutual elements of three or more peaks, and thus in this case overestimate the excluded volume. This is calculationally much simpler than finding the exclusion considering the full intersection and is unlikely to make a large difference.

Of these methods, "full exclusion" is the most extreme in annihilating mass, "half-exclusion" overcounts mass, which "binary reduction" remedies. After extensive exploration and comparison between these methods, we have chosen binary reduction as our standard (see BM2). To partition the mass between two peaks with Lagrangian radii $R_1 \geq R_2$, separated by a distance d, we wish to cut on a plane perpendicular to the vector d at a distance d_1 from the center of peak 1, and d_2 from the center of peak 2,

$$d_1 + d_2 = d, \qquad R_1^2 + d_1^2 = R_2^2 + d_2^2,$$

and such that peak 2 center is not within peak 1,

$$d_1 \geq d_2, \qquad d > R_1 - R_2.$$

We then have

$$d_1 = \frac{1}{2d}(d^2 + R_1^2 - R_2^2), \qquad d_2 = d - d_1. \tag{3.15}$$

The change in spherical volume of the two peaks is given by

$$\Delta V_j = \int_{d_j}^{R_1} dz \pi (R_j^2 - z^2) = \frac{2\pi}{3} R_j^3 - \pi d_j R_j^2 + \frac{\pi}{3} d_j^3, \qquad j = 1, 2 \,. \tag{3.16}$$

The fractional change in mass of the peaks is given by

$$\frac{\Delta M_j}{M_j} = \frac{1}{2} - \frac{3}{4} \frac{d_j}{R_j} + \frac{1}{4} \frac{d_j^3}{R_j^3}, \tag{3.17}$$

where d_1 and d_2 are calculated from equation (3.15). After all pairs of peaks are checked, then for each peak the fractional reductions from all its pairings are summed to obtain a total reduction. If the peak is reduced to zero mass, then it is eliminated. Although the mass reduction is strictly occurring on the overlaps between peaks, it is treated as a reduction in radius retaining sphericity of the patch.

3.3. *A Generalized Press-Schechter Method with Volume Exclusion*

If our method for identifying candidate points is efficient, we should get virtually the same result from a candidate point process which is much more highly oversampled. In § 3, we gave our standard threshold choice for density peaks, $f_t = 1.686$. We have found that choosing $f_t = 0$, which includes many more candidates, gives quite similar results to $f_t = 1.686$ after exclusion and merging. Instead of finding peaks in the density field, we might consider the points that are peaks in the strain eigenvalues. The picture of evolution of the medium suggested by the Zeldovich approximation is that the first regions to collapse are peaks of the largest eigenvalue λ_{v3} of the strain tensor. We have tried those points as candidates as well (with zero threshold) and find similar results to density peaks with $f_t = 1.686$. The Zeldovich approximation would also suggest peaks of the smallest eigenvalue λ_{v1} may be important for object formation, since the linear flow in the neighborhood of the candidate point will be converging upon the point in all three dimensions. (However, we find nonlinear internal tides in the ellipsoidal approximation allow initially nonconvergent flows to collapse.) We have tested these points as well (with zero threshold) and again find similar results to density peaks. These tests are described in § 4.2.3, and the mass functions for the various methods are shown below in Figure 13.

Although it is extremely inefficient to do so, one could choose *all* of the points in the volume. We believe that the result would be almost identical to that obtained with the λ_{v1} peak points, which sample a large fraction of the points in the simulation. The reason that choosing all of the "field points" and allowing exclusion to do all of the work is interesting is that this is precisely what a natural nonlocal generalization of the Press-Schechter approach to mass formulae would do.

Let us review what the Press-Schechter (PS) or excursion set approach does, following BCEK. Consider the set of candidate points to be the set of grid points in a lattice. Just as for our candidate peak points, PS methods again use the largest smoothing radius at which the density field equals the threshold f_c to define a Lagrangian radius and a mass. (The spherical approximation to dynamics is used to determine f_c.) Unlike the hierarchical peaks method, the PS method has *no exclusion* of points with small mass if they lie within the patches associated with points of large mass. Instead there is a binary "merging" algorithm of a strange sort: the two grid points contribute the fraction of space in their grid cells to the total (Lagrangian space) volume count of objects with their respective masses. Thus cells that are side-by-side invariably are counted as belonging to different mass objects, a decidedly unphysical vision. Obviously one can get no spatial information from this excursion set approach, and it is rather a miracle that the PS mass functions can come so close to those determined from N-body studies.

The natural smoothing to use for the PS formalism is top-hat filtering, but BCEK showed that only sharp k-space filtering gives the original Press-Schechter formula for the mass function. Top-hat and Gaussian filtering give a high-mass end that is the same as the original PS formula, but without the famous factor of two "fudge factor." To have the fraction of space in objects of any mass sum to unity, the mass functions for these filters have an extended low-mass tail less steep than the PS formula one (Peacock & Heavens 1990; BCEK). Although the PS formula with the factor of 2 does arise naturally for the sharp k space filter, how mass is assigned to the Lagrangian radius R_k at which the smoothed overdensity equals f_c is not well justified. R_k cannot be used by itself since the smoothing function associated with it is highly oscillatory, $\propto j_1(r/R_k)/(r/R_k)$. The method BCEK used was to construct the mass through a "top hat radius" function of R_k by requiring the variance in the density fluctuations smoothed with the two filters agrees:

$$M = (4\pi/3) \bar{\rho}_{nr} \bar{a}^3 R_{TH}^3, \qquad \text{where } \sigma_{TH0}^2(R_{TH}) = \sigma_{k0}^2(R_k) \,. \tag{3.18}$$

What the PS method should do is this: take all points. For each point, start at a large radius and come inwards until the volume-averaged linear overdensity $= f_c$. If so, assign that point the top-hat mass associated with the critical radius. Take the candidate points to be those which have pierced the f_c line. *Now apply to the candidate points the full exclusion algorithm of the last subsection.* Most candidate points are excluded and the surviving points with their nonoverlapping spherical Lagrangian patches about them are precisely our hierarchical peaks. We shall see that the end result for the mass function is not very different from the standard Press-Schechter result, with a slightly modified mass assignment, but there are no fudges, the mass assignment is natural and one can do spatial structure, including correlations. More important, the peaks picture is physically correct.

4. IMPLEMENTATION OF THE HIERARCHICAL PEAKS METHOD

We described the physical and mathematical underpinnings of the peak-patch picture in § 2. We now present the detailed implementation of the algorithm used to realize catalogs of virialized objects—the Hierarchical Peaks Method for Peak-Patch Catalog Generation.

The basic procedure consists of three stages: identify candidate peaks in a simulation volume, measure internal peak-patch parameters, and perform the displacements to the final Eulerian positions.

Let us suppose we have a catalog covering some cosmological comoving volume we wish to simulate. We first need to cover the volume with cubic boxes in comoving space. The size of each box is the largest we can manage subject to accurately realizing the smallest scale we think we need to identify the internal properties of the peak-patches of interest. For cluster catalogs, we have found that if 128^3 lattices are the size limitation, then a box size of $(200\,h^{-1}\,\mathrm{Mpc})^3$ gives sufficient short distance resolution. For galactic halos at high redshift, the boxes would be much smaller. The standard configurations are a single box (for checking with N-body results), many boxes in a cubical configuration, for all-sky catalogs, and, for catalogs covering a limited area on the sky, an inverted pyramid of boxes which contains within it a "cone" or "wedge," of given angular size. In this paper, we illustrate the situation for a single box, and in BM3 we show results for an all-sky cluster catalog out to $z = 0.1$ that uses 27 boxes, and a $5° \times 5°$ wedge that goes out to redshift 1.5 that uses 11 boxes.

Cubical boxes are chosen to get the advantages of the speed of FFTs, but the FFT restrictions of allowed wavelengths to the modes of the box are circumvented by the direct addition of ultralong wavelength modes as needed. The situation is reminiscent of the split between background and fluctuating fields described in the last section, and we adopt that notation. That part of the linear density field F that can be obtained by FFT is denoted by F_f and that part built from the ultralong wavelength modes by F_b; similarly for the displacement field s_f and s_b. The cut between the waves which build F_f and those that build F_b is taken to be a sharp one in k-space, with boundary k_b. That is, the Fourier components $\tilde{F}_b(\boldsymbol{k}, t)$ have $|\boldsymbol{k}| \leq k_b$ and the Fourier components $\tilde{F}_f(\boldsymbol{k}, t)$ have $|\boldsymbol{k}| > k_b$.

We describe the version of the algorithm in which the candidate points are density peaks above a threshold f_t.

I. Choose a pattern of contiguous boxes which completely covers the catalog volume.

II. If there is significant power beyond the fundamental mode of the boxes:
   A. Choose a sampling strategy for the ultralong wavelength modes, e.g., a combination of logarithmic and power-law sampling in $|\boldsymbol{k}|$, and uniform in k-space solid angle. Choose the number of wavelengths, typically $\lesssim 5000$. Determine k_b as that wavenumber at which the k-space volume of the long-wavelength sampling strategy equals the cell volume in the reciprocal k space of the box. A detailed discussion of this procedure is given in Appendix D.
   B. Construct a realization of the Fourier components of the background linear density field, $\tilde{F}_b(\boldsymbol{k}, t_0)$, for the chosen k-space sampling. The power spectrum $P_F(k)$ and $\tilde{F}_b(\boldsymbol{k}, t_0)$ are normalized with the linear growth factor $D = 1$ at the present time $t_0(z = 0)$.
   C. Evaluate σ_{0b} for the waves with $k < k_b$. Lower the threshold f_t to allow for very rare ultralong wavelength excursions (e.g., $f_t = 1.686 - 5\sigma_{0b}$).

III. For each box, centered at redshift z_{box}, we
   A. Realize discrete Fourier components $\tilde{F}_f(\boldsymbol{k}, t_0)$ of the linear Gaussian random density field on the reciprocal lattice wavevectors of the grid, using $P_F(k)$, and normalized with $D = 1$ at t_0. [We set $\tilde{F}_f(\boldsymbol{k}, t_0) = 0$ if $|\boldsymbol{k}| < k_b$.]
   B. Determine the linear growth factor $D(t_{\mathrm{box}})$ at time $t_{\mathrm{box}} = t(z_{\mathrm{box}})$ for the chosen cosmology. If evolution of $D(t)$ across the box should be included, this is the largest D within the box. Form the modified threshold $f_t(t_{\mathrm{box}}) = f_t(t_0)/D(t_{\mathrm{box}})$.
   C. Form the Fourier components of the displacement field $\tilde{s}_f(\boldsymbol{k}, t_0)$ of s on the grid, $\tilde{s}_k = -i(\boldsymbol{k}/k^2)\tilde{F}_k$, and do an FFT to get $s(\boldsymbol{r}, t_0)$.
   D. For each Gaussian filter scale R_G, working downward from largest to smallest,
      1. Filter the density field in Fourier space $\tilde{F}_f(\boldsymbol{k}, t_0; R_G) = \tilde{F}_f(\boldsymbol{k}, t_{z\mathrm{box}}) \exp(-k^2 R_G^2/2)$. Transform to real space, to form the filtered $F_f(\boldsymbol{r}; R_G)$, using a three-dimensional real Fast Fourier Transform (FFT). (The ultralong modes are not included, but would be lost by the FFT anyway).
      2. Find the peaks of F in the $F_f(\boldsymbol{r}, t_0; R_G)$ realization above the threshold $f_t(t_{\mathrm{box}})$. In the implementation on a grid, a peak pixel is required to be larger (or equal to) each of its 26 nearest lattice neighbors. Construct a list of peak positions $\{\boldsymbol{r}_{\mathrm{pk}}\}$. (Do not include peaks that have been listed at a larger filter.) Provided k_b is small enough, $F_b(\boldsymbol{r}, t_0; R_G)$ will have no impact on whether a pixel is a peak or not.

IV. Fast Fourier transform the unfiltered density field $\tilde{F}_f(\boldsymbol{k}, t_0)$ to get $F_f(\boldsymbol{r}, t_0)$. (Or weakly filter it to ensure smoothness at the shortest distances.)

V. For each peak at position $\boldsymbol{r}_{\mathrm{pk}}$,
   A. If evolution over the region of the box is to be included, evaluate $D(t_{\mathrm{pk}})$, where $t_{\mathrm{pk}} = t(z_{\mathrm{pk}})$ is the cosmological time and z_{pk} is the redshift at the comoving distance of the peak from the global origin of coordinates. Otherwise, take $t_{\mathrm{pk}} = t_{\mathrm{box}}$ and $D(t_{\mathrm{pk}}) = D(t_{\mathrm{box}})$.
   B. Determine R_{pk} by numerical integrations of $F(\boldsymbol{r}, t_0)$ and $s(\boldsymbol{r}, t_0)$ on the lattice in spherical steps outward from the peak center. Evaluate, by direct summation over the ultra-long wavelength modes, $F_b(\boldsymbol{r}, t_0)$ and $s_b(\boldsymbol{r}, t_0)$ for the points $\boldsymbol{r}$ swept over as needed, if they have not already been calculated for an earlier peak [If $k_b R < 1$, these vary slowly enough that only $F_b(\boldsymbol{r}_{\mathrm{pk}}, t_0), s_b(\boldsymbol{r}_{\mathrm{pk}}, t_0), e_{bij}(\boldsymbol{r}_{\mathrm{pk}}, t_0)$ need be evaluated.]. Keep track of $\bar{F}(<R, t_0), \bar{s}(<R, t_0)$, and (possibly) $\bar{e}_{ij}(<R, t_0)$. See Appendix E.

1. In the *spherical* approximation, at each radius step R: adjust the average overdensity to be the value at $z_{\rm pk}$, $\bar{F}(<R, t_{\rm pk}) = D(t_{\rm pk})\bar{F}(<R, t_0)$; determine whether a spherically symmetric region with linear overdensity $\bar{F}(<R, t_{\rm pk})$ will have collapsed by $z_{\rm pk}$. For $\Omega = \Omega_{\rm nr} = 1$, just compare with the "critical" value f_c; for $\Lambda \neq 0$ models, a look-up table of collapse redshifts, $z_c(F)$, is used. Truncate the outward search with $R_{\rm pk} = R$. [$\bar{e}_{ij}(<R, t_0)$ is not calculated.]

2. In the *homogeneous ellipsoid* approximation, at each radius step R, form the mean strain tensor at redshift $z_{\rm pk}$, $\bar{e}_{ij}(<R, t_{\rm pk}) = D(t_{\rm pk})\bar{e}_{ij}(<R, t_0)$. Calculate the eigenvalues λ_{vi}, and hence the peak ellipticity e_v and prolaticity p_v (eq. [2.20d]). Determine if a region with $\bar{F}(<R, t_{\rm pk})$, e_v, and p_v would have collapsed by $z_{\rm pk}$, using a look-up table for the redshift of "collapse" along the final axis z_c. Truncate the outward search with $R_{\rm pk} = R$ when $z_c = z_{\rm pk}$.

C. Evaluate the peak-patch averages $M_{\rm pk} = (4\pi/3)\bar{\rho}_{\rm nr}\bar{a}_{\rm pk}^3 R_{\rm pk}^3$, $\bar{s}_{\rm pk} = s(<R_{\rm pk}, t_{\rm pk}) = D(t_{\rm pk})s(<R_{\rm pk}, t_0)$, and the internal energy $E_{\rm int,pk}$.

VI. The list of candidate points is now trimmed by a Lagrangian-space exclusion and merging algorithm, to avoid mass over-counting and the "cloud-in-cloud" problem.

A. In *full exclusion*, the most massive peak in a set of mutually overlapping peaks is retained, while the others are discarded.

B. In *binary exclusion/reduction*, for each pair of overlapping peaks, the mass of each is reduced to the value obtained by partitioning with a plane defined by the intersection of the spherical surfaces of the two Lagrangian spheres. For pairs of peaks with center separations less than the radius of the larger of the two, the less massive peak is discarded with no reduction of the survivor.

We now have the hierarchical peak patches in Lagrangian space.

VII. The Lagrangian space peak patches are moved to their final Eulerian positions using the Zeldovich approximation (possibly augmented by a quadratic correction). We either

A. Use the spherically averaged displacement calculated during the integration stage $\bar{s}_{\rm pk}$ to move the peak to its final Eulerian position $x_{\rm pk} = r_{\rm pk} - \bar{s}_{\rm pk}$.

B. Use the displacement field evaluated at $r_{\rm pk}$ at $t_{\rm pk}$ Gaussian filtered over a fixed smoothing scale R_s. We have used the value $R_s = D(t_{\rm box})\sigma_s/\sqrt{3}$, the one-dimensional rms displacement at redshift $z_{\rm box}$, with $\sigma_s \equiv \sigma_{f-1}(R_f)$ for a judiciously chosen filter R_f. We *strongly* prefer the top-hat smoothing strategy (A.), which has a spatially varying smoothing filter.

C. Make further mergers of the final state patches, if desired. (Lagrangian-space exclusion rarely makes this important, at least for the cases we have treated so far.)

VIII. We ascribe final-state profiles to the patch, using the Lagrangian space quantities $R_{\rm pk}$, $F_{\rm pk}$, e_v, p_v, strain tensor orientations, internal energy, and bulk velocity to scale them. The bulk velocity is $V_{\rm pk} = -a_{\rm pk}H_D(a_{\rm pk})s_{\rm pk}$. Sample internal properties are the mass, $M_{\rm pk}$; the mass-averaged interior three-dimensional (isolated virial) velocity, $v_E = (-2E_{\rm int,pk}/M_{\rm pk})^{1/2}$; an Eulerian "top-hat" radius for the final-state patch, $R_{\rm E,pk} = 0.3a_{\rm pk}R_{\rm pk}/F_{\rm pk}$. The internal properties and profiles depend upon detailed knowledge from N-body/hydrodynamical calculations of individual peak-patch collapses, or from observations. This translation from Lagrangian to Eulerian properties is accompanied by statistical dispersion—more information is needed than the limited number of Lagrangian space properties we measure to define the profiles—and by uncertainties in our knowledge of the fate of peak patches. The latter uncertainties enter like systematic errors and currently dominate over statistical errors associated with a dispersion of final fates. BM3 addresses this for clusters.

The computational requirements for implementation of this method are actually rather modest. Each filter scale R_G uses an FFT, the computation of the displacement uses three FFTs, and after the peak finding, each spherical or ellipsoidal collapse calculation requires a grid search and integration (the ellipsoidal dynamics uses an eigenvalue computation also). Because the fields are real, so only the complex Fourier components are needed for the upper half of k-space, we use appropriately packed real FFTs to decrease the storage requirements by a factor of 2. The CPU speed of most workstations is sufficiently fast for 128^3 or even 256^3 grids. The storage for the F and s arrays requires 32.8 MB (4 bytes $\times$ 128^3 $\times$ 4 components). In practice, we retain the unfiltered Fourier components $\tilde{F}(k, t_0)$, an extra 8.2 MB of storage, to avoid recalculating them for each filter scale.

For a density peak calculation using the ellipsoidal approximation to internal dynamics, for a single box with a 128^3 grid, and 26 filter scales, 5 hours were used on a Silicon Graphics IRIS 4D/280 (CPU 25 MHz). The same calculation required only 20 minutes on a DEC Alpha 400 workstation.

If, instead of peaks in the linear density field, we use peaks in a chosen eigenvalue of the strain field to get the candidate points (e.g., λ_{v3} or λ_{v1} peaks), we need storage for the strain e_{ij}. We construct at each Gaussian-filter R_G, the filtered Fourier components $\tilde{e}_{ij,f}(k, t_0) = -k_i k_j \tilde{F}_f(k, t_0)e^{-(kR_G)^2/2}$, perform a Fast Fourier Transform upon it, and evaluate the eigenvalues at each grid point of the lattice for each box. This procedure adds five more 8.2 MB arrays of storage (because storage for $F = -\sum_i e_{ii}$ has already been counted), and, the extra computer cycles associated with the five extra FFTs and the eigenvalue determinations at each filter.

In BM2, we compare the results of this algorithm and variations of it with N-body simulations to check the performance of the method. With assumptions about the baryonic content of the galaxies and cluster intergalactic medium of the clusters, this catalog can be used to compare with observational data. So far we have applied this Monte Carlo method to construct submillimeter and millimeter maps of emission from dusty primeval galaxies and to construct X-ray and Sunyaev-Zeldovich maps of emission and scattering by clusters (Bond & Myers 1991, 1993a, b). We describe how the cluster applications are done in BM3. We now investigate the performance of various of the options described above.

4.1. *Performance of the Hierarchical Peaks Algorithm*

Figure 6 shows a slice of width 6 h^{-1} Mpc in a 200 h^{-1} Mpc box which illustrates the various stages that a hierarchical peak calculation passes through. The first panel shows the original peaks (cut by the threshold $f_t = 1.686$), with the size of the Lagrangian spheres chosen by $R_{TH} = 2R_G$, where R_G is the Gaussian filter used to find the filter. This shows the cloud-in-cloud problem, with small filter peaks inside large ones. The second panel shows the transformation in the radius that occurs when measurements are made in Lagrangian space. On average for the large peaks, the radius increases. The third panel shows the remaining peaks after the operation of binary exclusion. The last panel shows the transformation into Eulerian space. The circle size is $R_{E,pk} = 0.3\bar{a}_{pk}R_{pk}/F_{pk}$. For $F_{pk} = 1.686$, this is $R_{E,pk} = \bar{a}_{pk}R_{pk}/(179)^{1/3}$, taking the Lagrangian sphere and compactifying it into a sphere with overdensity $1 + \delta_{Vcut} = 179$. The lines show either where the peak is going, in the case of Figures 6*a*–6*c* or where the peaks have come from in the case of Figure 6*d*.

4.1.1. *Peak-Finding for the Candidate Point Process*

There are many possible strategies for identifying the candidate points—we choose the practical approach of finding peaks of the linear density field F smoothed on a set of Gaussian filtering scales. Since we are calculating our dynamics for a spherical top-hat filtered field, it would be natural to use a set of top-hat filters for peak selection. However, a top-hat–filtered CDM density field tends to be quite choppy at small scales, since the high k limit of the filter equation (2.6) only damps as a k^{-2} power, and higher derivatives
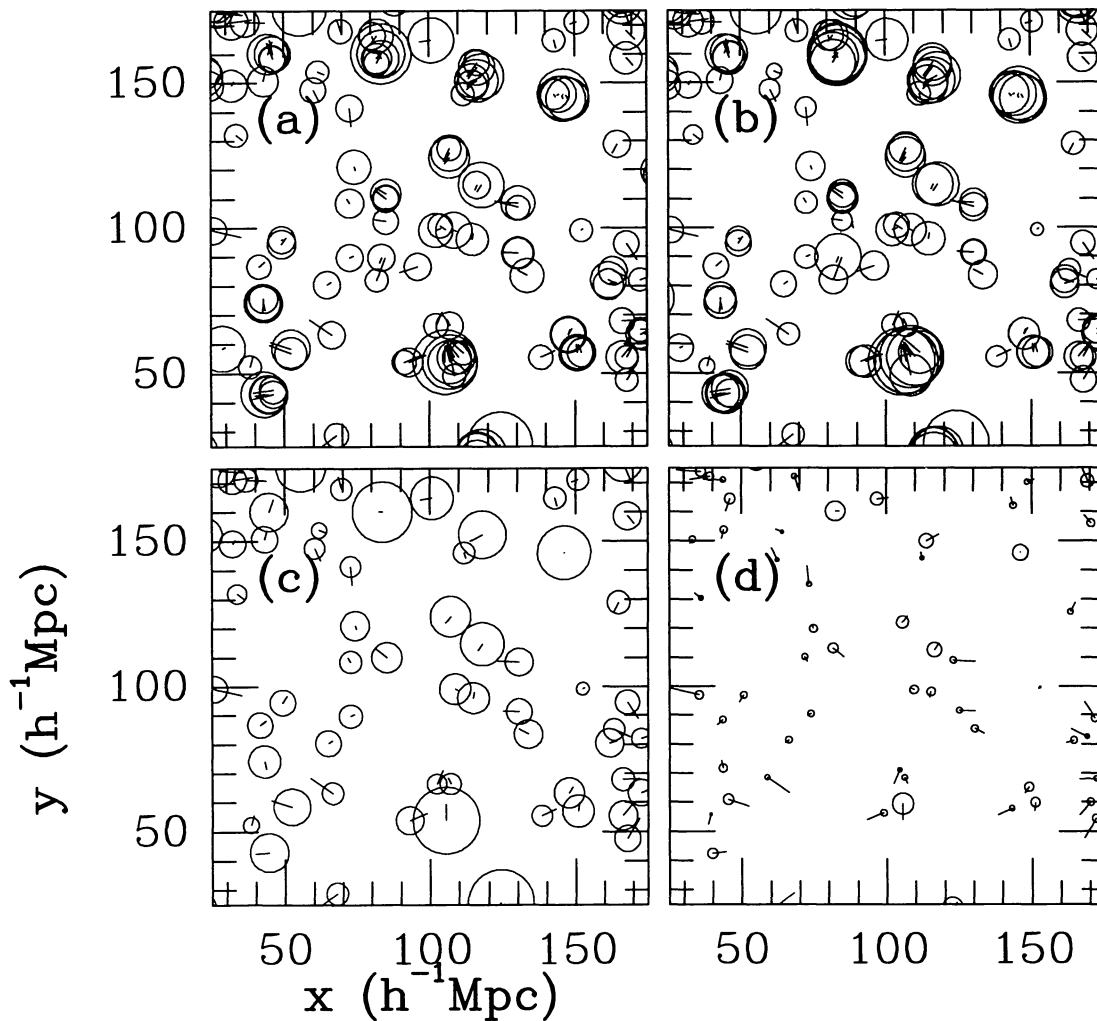

Fig. 6.—The stages of a hierarchical peak calculation for a $\sigma_8 = 0.97$ CDM model, for a slice of width $6h^{-1}$ Mpc (at $z = 120h^{-1}$ Mpc) projected onto the (x, y) plane for the inner $150h^{-1}$ Mpc of the $200h^{-1}$ Mpc box. In panels (*a*–*c*), the peaks are in Lagrangian space, and the lines give the Zeldovich displacement to their final Eulerian positions. (*a*) Selected Gaussian-filtered peaks above threshold $f_t = 1.686$ (with circle radius $1.95 R_G$), show the cloud-in-cloud problem. (*b*) Candidate peaks with radii R_{pk} calculated from ellipsoid collapse. (*c*) Postexclusion peaks after binary reduction. (*d*) Final peaks in Eulerian space, with radii $R_{E,pk} = \bar{a}_{pk}R_{pk}/(179)^{1/3}$ and lines back to the peaks' origins.

of the field are only differentiable by virtue of the Nyquist cutoff on the modes allowed in the box. In particular, peaks are sensitive to the second derivative of the density field, and this field has most of its power at these short scales. Although we add a Gaussian filter on the scale $a_L/2$, which would smooth the edges of any top-hat filter (called bowler-hat filtering in BCEK), we feel that the candidate points we would find with top-hat filtering would not be as optimally placed as those we find with Gaussian filtering, and there would be more of them to check. The added complication of k-space filtering with j_0 also leads us to use the Gaussian filters instead.

An important step is to determine the number of filters needed to ensure there are enough points sampled while minimizing the computational effort. For our standard example of the simulation of clusters in a $(128)^3$ 200 h^{-1} Mpc box with scale-invariant CDM initial conditions ($\Omega = \Omega_{cdm} = 1$, $h = 0.5$ and $\sigma_8 = 0.97$), we find a range of Gaussian filter radii from $2\,h^{-1}$ Mpc $\leq R_G \leq 8\,h^{-1}$ Mpc to be adequate. The mass associated with the filter scale can be estimated from $R_{pk} \approx 2 R_G$ and thus the typical cluster-building wavenumber is $k^{-1} \sim 4\,h^{-1}$ Mpc as $\sigma_\rho(4\,h^{-1}$ Mpc$) = 0.95\sigma_8$. The lower limit is determined by the lattice scale ($1.56\,h^{-1}$ Mpc). For the CDM model, $\sigma_\rho(2\,h^{-1}$ Mpc$) = 1.75\sigma_8$, hence 1σ peaks at this scale can reach $f_c = 1.686$. Choosing such a low cut for the filters helps to saturate the medium with candidate points. The upper limit is determined by the most massive peak patch to be found in the volume. For the CDM spectrum $\sigma_\rho(8\,h^{-1}$ Mpc$) = 0.45\sigma_8$ and thus for $\sigma_8 = 0.97$ it would take a $\nu \approx 3.7$ peak at $R_G = 8\,h^{-1}$ Mpc to reach $f_c = 1.686$, and these are very rare indeed.

The number of filters we use between an identified minimum and maximum is a matter of debate. Because the runs are not that computationally demanding, we tend to err on the large number side: for our cluster simulations, we use a hierarchy of 25 filters, spaced logarithmically from $R_G = 2.0\,h^{-1}$ Mpc to $R_G = 8.0\,h^{-1}$ Mpc; we could halve the number of filters and still get excellent results.

Peak finding on the lattice is a simple operation, consisting of checking F at each grid position against the value at the 26 immediate neighboring sites. A preliminary culling of the peak candidates can be made by placing a lower cutoff $f_t(t_{pk})$ on the filtered field $F(r; R_G)$ at each pixel. For example, we can limit our search to those above $f_t(t_0) = f_c = 1.686$, which is the critical value for a spherical top-hat perturbation to have collapsed by the time of interest (see § 3.3). The difference in peaks found with the density threshold $f_t = 1.686$ are compared with those found with no threshold ($f_t = 0$) in Figures 7 and 8. They are essentially the same.

4.1.2. *Strain Eigenvalue Peak Finding*

In the homogeneous ellipsoidal approximation to dynamics, the eigenvalues λ_{vi} of the strain tensor are required to determine the fate of the region. Thus, instead of looking for peaks in the density field F, one might, for example, look for peaks in the λ_{v3} or λ_{v1} "field". This provides a different list of candidate points about which the internal properties are measured.

In Figure 7, we show that the candidate lists consisting of λ_{v3} and λ_{v1} peaks do differ somewhat from those found using an F-peak candidate list, with λ_{v1}-peaks sampling the Lagrangian space more densely and λ_{v3}-peaks more sparsely. In Figure 8, we show that this effect causes the final hierarchical peak patches found after binary exclusion to also differ from F peak patches. These were obtained with a threshold on the density field F of $f_t = 0.01$. The high-mass objects remain more or less the same, but it is the low masses that are affected. We also show that using $f_t = 0.01$ for the F-peak candidate list does not give a very different spatial structure than using our standard $f_t = 1.686$ threshold. During the evaluation of the hierarchical peaks method (BM2), we shall show how these different options fare with N-body data. We conclude there that the F-peak candidate point algorithm *with* the $f_t = 1.686$ choice does somewhat better than using the shear eigenvalues, although all do reasonably well.

4.1.3. *Exclusion and Merging Performance*

In Figure 9, we show how the three exclusion methods affect the distribution in Lagrangian space. Since binary reduction begins with those peaks remaining after half-exclusion and proceeds to reduce the masses until overlaps are removed, the two show similar results, except for the slightly smaller masses for the binary algorithm (manifested by the radii in the figure). Note the significant overmerging in the case of full exclusion.

4.2. *Statistical Measures of Peak-Patch Properties*

We now describe some of the properties of the final list of peaks. We defer the treatment of the distribution of strain ellipticities, prolaticities, and the top-hat averaged linear overdensity (i.e., the threshold for collapse) for the ellipsoid dynamics to BM4, where we show how the features can be well understood by analytic means. We also defer the treatment of peak bulk velocities to BM4.

4.2.1. *Filter Radius versus Mass*

We first investigate the relationship between the hierarchical filter scale and the mass of the peaks that are found under it. In Figures 10a–10b, we plot the peak mass M_{pk} versus the filter radius R_G, where the peak masses were determined using the spherical collapse model. We see that for masses $\gtrsim 4 \times 10^{14}\,h^{-1} M_\odot$ the relationship roughly follows the proportionality

$$R_{TH} = 2.1 R_G \,. \tag{4.1}$$

In this plot, the peak masses were reduced for overlaps using the binary reduction method. A very similar result is obtained if full
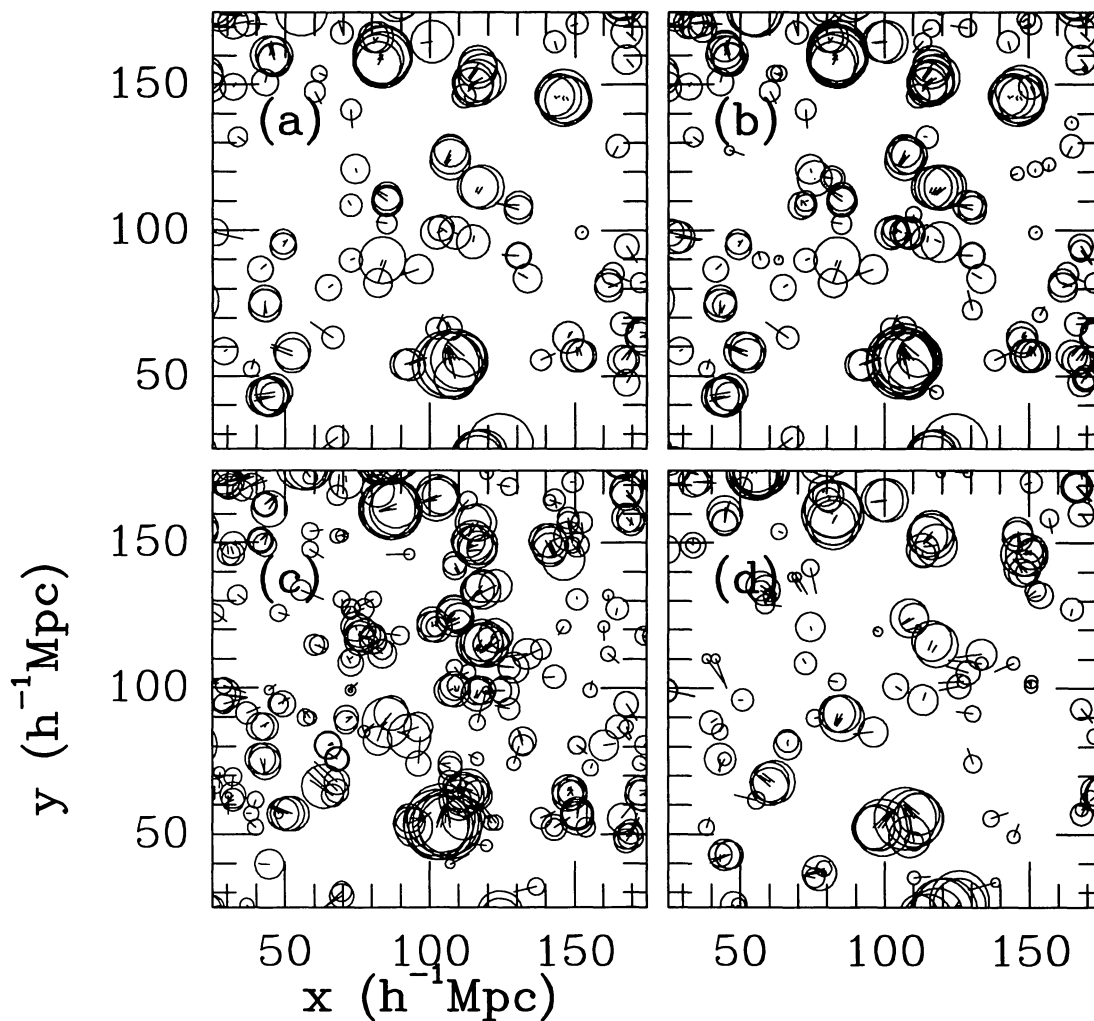
FIG. 7.—We show the effect of varying peak-finding algorithms on the candidate points before exclusion. (a) Standard F peaks, $f_t = 1.686$; (b) F peaks, $f_t = 0.01$; (c) λ_{v1} peaks, $f_t = 0.01$; (d) λ_{v3} peaks, $f_t = 0.01$. The plots are x, y projections of a $6h^{-1}$ Mpc thick slice in the inner $150h^{-1}$ Mpc of the $200h^{-1}$ Mpc box. The peaks are shown as circles of radius R_{pk}, plotted in their initial Lagrangian positions, with the vector showing the Zeldovich displacements to the final Eulerian coordinates.

exclusion is used. In Figure 10b the mass M_{pk} versus filter R_G is shown for the homogeneous ellipsoid model. The peak mass using the ellipsoidal collapse roughly follows

$$R_{TH} = 1.95 R_G, \tag{4.2}$$

consistent with a 20% reduction in mass with respect to the spherical model (see § 4.2.3). (The analytic theory of BM4 gives R_{TH}/R_G in the range 1.940–1.976.) Notice that the spherical and ellipsoidal models have very different distributions of R_{TH} for a given R_G, with the tail of the former extending upward past the best-fit line, and of the latter extending downward. The large scatter in peak mass at the smaller filter scales demonstrates the inaccuracy that arises if masses were determined solely based upon Gaussian filter, the first strategy we tried.

4.2.2. Internal Energy versus Mass

The internal binding energy v_E versus M_{pk} for the peaks is shown in Figure 11. For peaks with mass $M_{pk} \geq 2.5 \times 10^{14}\, h^{-1} M_\odot$, we fitted to a $v_{E,pk} \propto R_{pk}$ power-law relation and find

$$v_{E,pk} \approx 1560 \left(\frac{M_{pk}}{10^{15}\, h^{-1} M_\odot} \right)^{1/3} \text{km s}^{-1}. \tag{4.3}$$
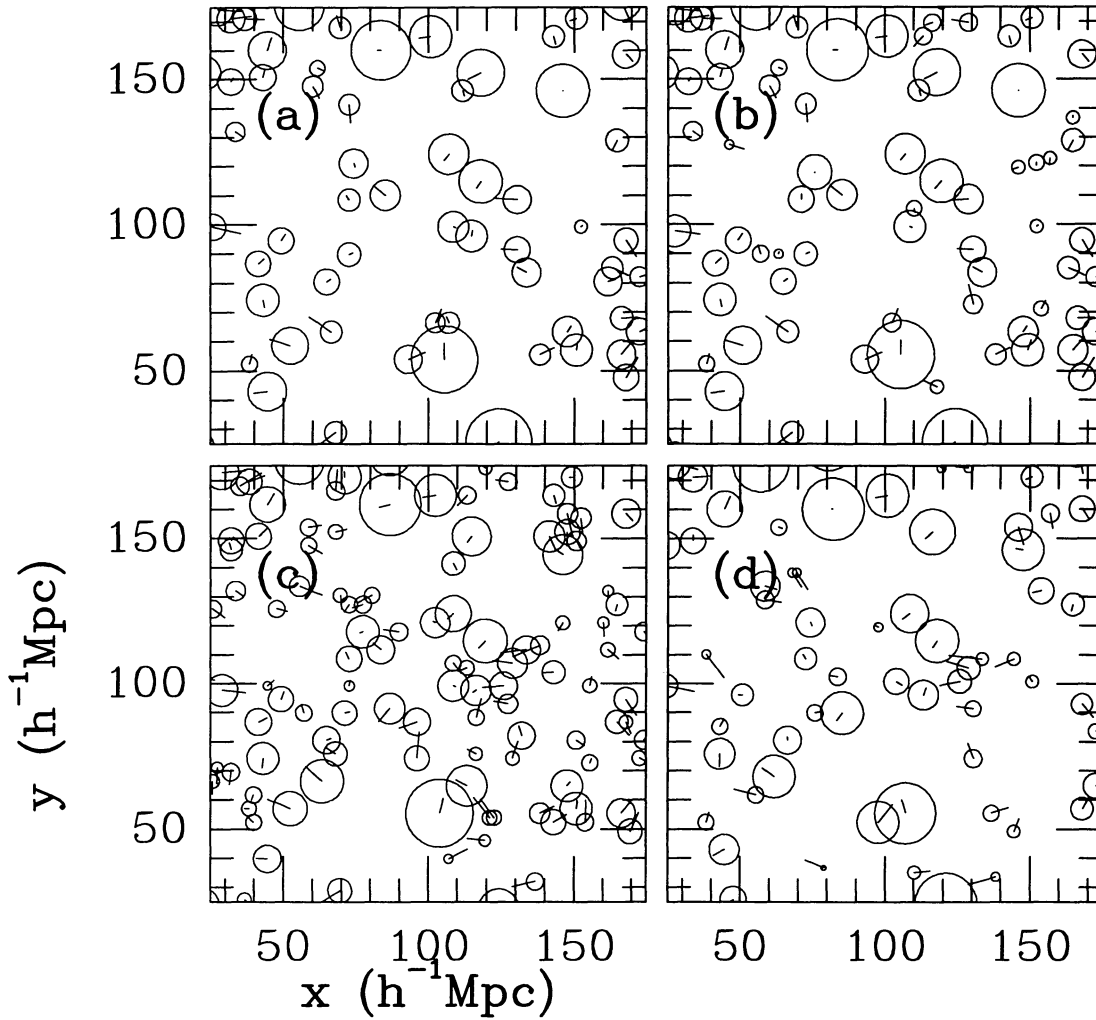
FIG. 8.—We show the effect of varying peak-finding algorithms on the final hierarchical peaks found after binary reduction. (*a*) Standard F peaks, $f_t =$ 1.686. (*b*) F peaks, $f_t = 0.01$. (*c*) λ_{v1} peaks, $f_t = 0.01$. (*d*) λ_{v3} peaks, $f_t = 0.01$. The plots are x, y projections of a $6h^{-1}$ Mpc thick slice in the inner $150h^{-1}$ Mpc of the $200h^{-1}$ Mpc box. The peaks are shown as circles of radius R_{pk}, plotted in their initial Lagrangian positions, with the vector showing the Zeldovich displacements to the final Eulerian coordinates.

The data points actually prefer a slightly flatter relation than the $M^{1/3} \propto R_{pk}$ power law we imposed. A least-squares fit yields

$$v_{E,pk} = 1510 \left(\frac{M_{pk}}{10^{15} \, h^{-1} M_\odot} \right)^{0.29} \text{km s}^{-1} \tag{4.4}$$

with an rms residual in v_E of 5.1%. The analytic counterpart to the hierarchical peaks theory gives a mean relationship between $v_{E,pk}$ and M_{pk}, which for ellipsoid dynamics gives a superb fit; i.e., the analytic and Monte Carlo results agree.

As we shall discuss in detail in BM2, to translate to observed velocities or gas temperatures will generally involve a correction factor multiplying this internal energy that should be calibrated with detailed internal evolution calculations. The amount of the correction will depend in detail upon the observation to be compared with. Here, we shall just compare our result with the standard temperature-mass relation that most groups using the Press-Schechter approach have adopted. This is from Evrard's (1990) (rather small 16^3) smooth particle hydrodynamics simulations of cluster collapse:

$$T_X = 6.2(M/10^{15} \, h^{-1} \, M_\odot)^{2/3} \text{ keV} .$$

To translate this to a velocity-mass relation, we assume that $T_X = m_N(v_T^2/3Y_T)$, where Y_T is the total number of particles per baryon contributing to the internal energy, m_N is the nucleon mass, and v_T is the three-dimensional velocity dispersion:
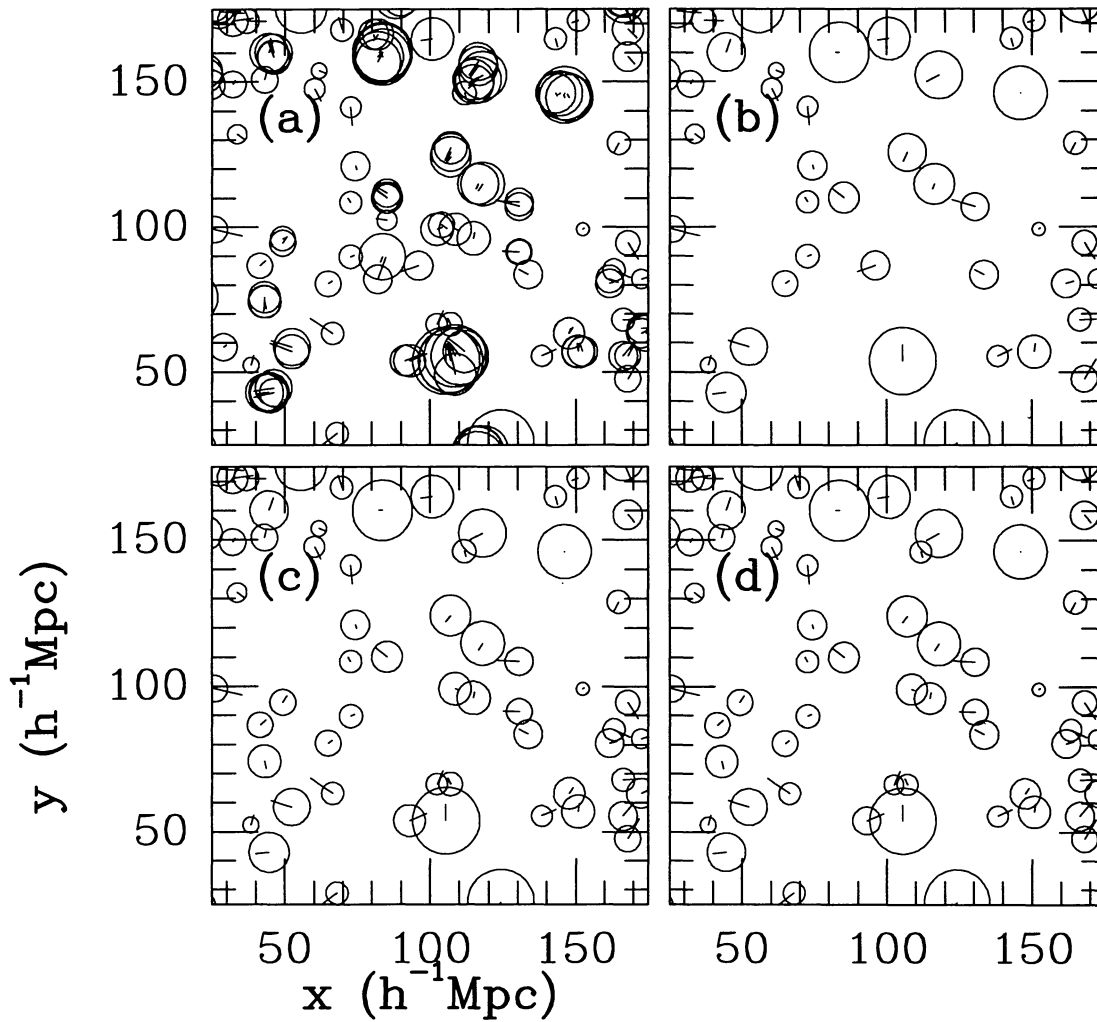
FIG. 9.—We show how the three Lagrangian exclusion methods affect the x, y projection in Lagrangian space, for the same slice of width $6h^{-1}$ Mpc in the inner $150h^{-1}$ Mpc of the $200h^{-1}$ Mpc box. (a) No exclusion. (b) Full exclusion. (c) Half-exclusion. (d) Half-exclusion with binary reduction, our preferred method. Masses of some groups in (d) are slightly reduced over the values in (c). These all use the standard F-peaks with $f_t = 1.686$.

$$v_T \approx 1730 (M/10^{15} h^{-1} M_\odot)^{1/3} \text{ km s}^{-1} .$$

This is 11% higher than our internal energy estimation of v_E. In BM2, we shall show that the kinetic energy of N-body groups has about an 11% correction over our internal binding energy estimates, in agreement with the Evrard number, while a velocity estimated from the internal energy of the groups, assuming an isolated virial equilibrium, is $\sim 6\%$ lower than our internal energy estimate. These numbers are also consistent with the trend seen in the single constrained collapse calculation of § 2.2.

4.2.3. Peak-Patch Mass Functions

The average density in objects above mass M (in units of the critical density ρ_{cr}) is given by

$$\Omega(>M) = \frac{1}{\rho_{cr} V_{box}} \int_M^\infty m \, d \ln m \frac{dn_{pk}}{d \ln m} = \frac{1}{\rho_{cr} V_{box}} \sum_{M_{pk} > M} M_{pk} , \tag{4.5}$$

where V_{box} is the simulation volume ($200^3 h^{-3}$ Mpc^3). The mass function comparison between Monte Carlo hierarchical peaks, analytic peaks, and the Press-Schechter approximation is summarized in Figure 12. Binary reduction was used to deal with Lagrangian overlaps. The mass function assuming spherical dynamics is shifted upward in mass by $\sim 20\%$ at the high-mass end (average 23% for $M_{pk} > 4 \times 10^{14} h^{-1} M_\odot$) relative to that for the ellipsoidal approximation to dynamics.

The standard Press-Schechter method determines mass from a top-hat filtering radius for the rms density fluctuations that enter
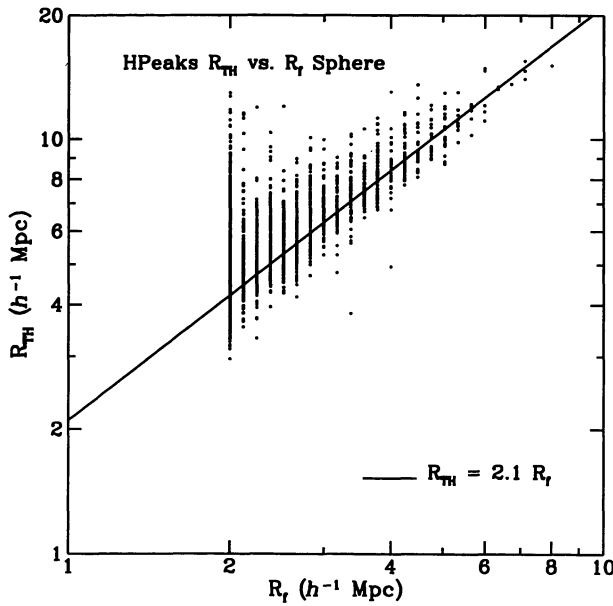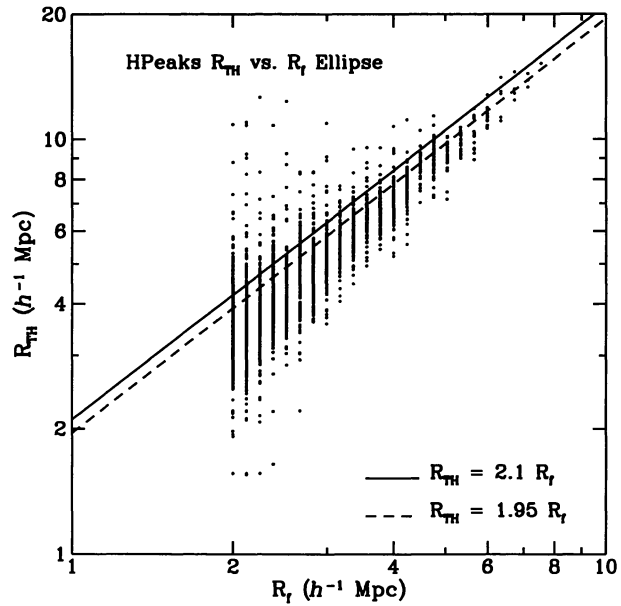
FIG. 10a   FIG. 10b

FIG. 10.—The Lagrangian top-hat radius R_{TH} vs. Gaussian filter radius R_G for peaks using the spherical (a) and ellipsoidal (b) models for interior peak-patch dynamics. The solid line in (a) and (b), $R_{TH} = 2.1\,R_G$, is an empirical fit to the spherical-peak data. The dashed line in (b) corresponds to $R_{TH} = 1.95\,R_G$, which analytic calculations also give. This reduction over the spherical case is an average of $\sim 20\%$ in mass.

the formula. With this mass, the PS method falls short of reproducing the peaks mass function. It matches quite well on the rare event side when the masses are corrected by a factor ~ 1.3. A better way to correct the PS formula is to work within the top-hat framework, but let f_c vary. In the figure, we have decreased f_c to 1.58, a 6% drop from the canonical 1.686 value. If all other things are equal, this changes the $v_T - M$ relation only by a factor of $(f_c/1.686)^{1/2} = 0.97$. In any case, the people who do Press-Schechter studies of X-ray and optical clusters take the $v_T - M$ relation using the estimate of mass from the rms fluctuations. We show in BM2 that the relation $v_T \approx 1755(M_g/10^{15}\,h^{-1}\,M_\odot)^{1/3}$ km s^{-1} actually fits N-body group kinetic energy data up to ~ 1400 km s^{-1} for a $\sigma_8 = 0.97$ CDM model. If we use this in the PS formula with $f_c = 1.58$, we get a reasonable fit to the group kinetic energy data. Of course, there is no dynamical justification for a lower f_c.
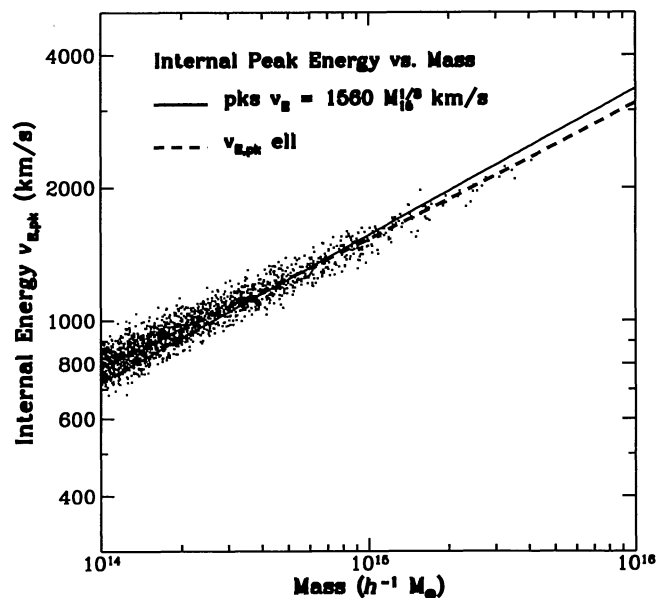

FIG. 11.—The velocity dispersion $v_{E,pk} = |2\varepsilon_{int}|^{1/2}$, where ε_{int} is the internal energy per mass of the peaks, is plotted against peak mass M_{pk}. The solid curve is the best-fit $M^{1/3}$ power law: $v_{E,pk} = 1560\,(M_{pk}/10^{15}h^{-1}M_\odot)^{1/3}$. The dashed curve is the analytic relation for ellipsoidal dynamics, which fits better.
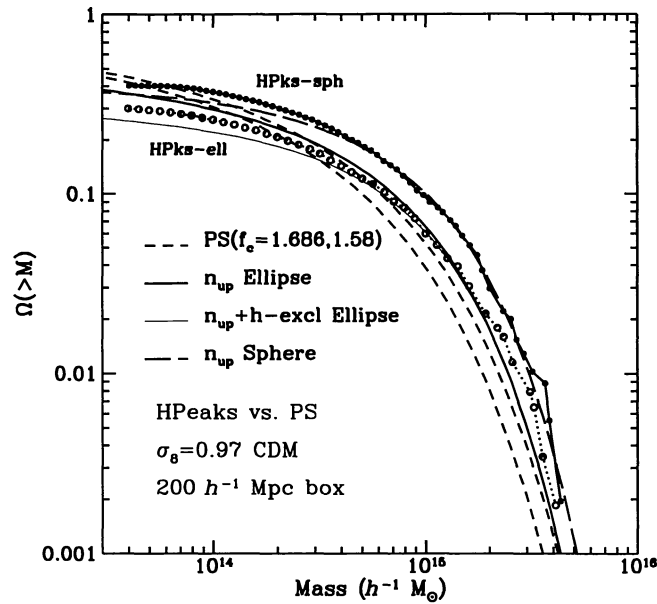
FIG. 12.—Cumulative mass functions Ω ($>M$) for the hierarchical peak-patch and Press-Schechter techniques, calculated in the $200h^{-1}$ Mpc box for a $\sigma_8 = 0.97$ CDM model. The Monte Carlo peak-patch results are shown for homogeneous ellipsoid internal dynamics (*open circles*) and for spherical dynamics (*filled circles*). The corresponding analytic curve (using the upcrossing formula) is shown for spherical (*long-dashed curve*) and ellipsoidal (*solid curve*) dynamics. The light solid line adds a further analytic approximation to half-exclusion. The Press-Schechter (PS) prediction (*lower short-dashed curve*), falls below the peaks relation, but agrees if the critical density threshold f_c is lowered from 1.686 to 1.58 (*upper short-dashed curve*). Note that the peak mass function determined by Monte Carlo simulations is incomplete below $4 \times 10^{14}h^{-1}M_\odot$.

Superposed on the Monte Carlo points are the analytic curves using peaks upcrossing through the threshold $F = f_c$, with f_c fixed at 1.686 for spherical dynamics, but with a threshold dependent upon e_v to treat ellipsoidal dynamics, $f_c(e_v)$, as described in BM4. Both the spherical and ellipsoidal analytic functions are in very good agreement with the Monte Carlo peak points. For the ellipsoid case, we also show a curve that approximates half-exclusion (Bond 1989b; BM4), the best analytic analog of binary exclusion.

In Figure 13, we compare the calculated mass functions if we use peaks of the largest eigenvalue λ_{v3} and the smallest eigenvalue
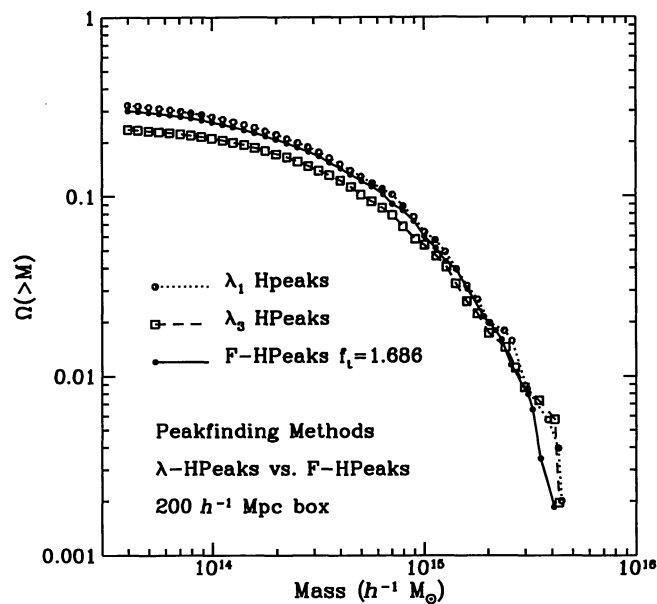
FIG. 13.—Cumulative mass functions Ω ($>M$) for different peak-finding algorithms, calculated for a realization of a $\sigma_8 = 0.97$ CDM model in a $200h^{-1}$ Mpc box. The curves shown are for peaks in the filtered density field F above $f_t = 1.686$ (*filled circles, solid line*), peaks of the largest eigenvalue λ_{v3} of the strain tensor e_{ij} for $f_t = 0.01$ (*open squares, dashed line*), and peaks of the smallest eigenvalue λ_{v1} (*open circles, dotted line*). The mass function for F peaks with $f_t = 0.01$ is indistinguishable from the $f_t = 1.686$ F-peaks curve. Ellipsoidal dynamics and binary reduction were used in all cases. The λ_{v3} peak function is significantly depleted at the low-mass end.

λ_{v1} (both with $f_t = 0.01$ applied to F). As a general comment, we note that at a given point a given threshold is reached at a larger filter radius for λ_{v3} than for λ_{v2} (similar to $F/3$), which in turn is larger than for λ_{v1}—just because of the eigenvalue ordering. The λ_{v1} peaks have a mass function much like that of F peaks in spite of this because, although there are many more small filter points, as is evident by comparing Figure 7c with Figures 7a or 7b, exclusion drastically reduces the number to one not very different from that given by postexclusion F peaks (compare Figure 8c with Figures 8a–8b). However, the λ_{v3} candidate peaks do not cover Lagrangian space densely enough so that exclusion can be relied upon to recover the balance, so that the postreduction λ_{v3} peak curve falls below the F-peaks curve at the low-mass end.

In BM2, we compare the various mass functions with those determined for N-body calculations, and show that the F peaks seem to be slightly preferred. The mass function for F peaks with $f_t = 0.01$ is very similar to that of the λ_{v1} peaks curve.

5. DISCUSSION AND CONCLUSIONS

In this paper, we have described the logical development of the peaks paradigm for how collapsed cosmic objects form. Although BBKS presented a pretty picture of structure formation based on peaks identified via a single-filter snapshot of the medium, there was really very little evidence that it worked. It just made sense physically that peaks had to be associated with the sites of structure formation. The flaws in the BBKS picture were clear from the beginning: peaks could reside within peaks, leading to overcounting of mass, the cloud-in-cloud problem (Bond 1989b; § 4.1.3). The single filter assumption gave all the peaks the same mass so no one-point differential mass function could be constructed (Bond 1989a, b). It also turned out that to the extent one could approximately use a single filter, the BBKS mass assignment was a factor of ~2 too small (Bond 1988, § E). Further, the number density of objects above a given "mass" was overcounted (Bond 1989b, BM4). Much work over the years was directed toward fixing up the BBKS-peaks problems. We believe that the method presented here solves all of these problems.

The peak-patch picture of structure formation is a compelling one. It is the natural consequence of gravitational instability in a medium for which the fluctuation spectrum is sufficiently steep such that the local collapse of a region can approximately decouple from the surrounding dynamics before the next higher scale collapses. Corrections to the linear theory can therefore be made by measurements of the patch of Lagrangian space surrounding the peak candidate—this will determine the fate of the region. It is the measurement of the density, displacement, and strain fields in the peak patches that really provide the utility of this method.

A critical aspect of our method is that the peaks we find on many filter scales are not the end product. They are just candidate sampling points for the crucial second phase of the operation, the exclusion and merging process (§ 4.1.3). We used information based on the average peak-strain field together with a local dynamical model to define the size of the patch for the candidate points. Obviously the homogeneous ellipsoid model cannot do full justice to the dynamics; and the spherical model fares worse. Prior work on homogeneous ellipsoids in cosmology did not properly reproduce linear theory. We showed how this could be done in Appendix A. The Zeldovich approximation was shown to be useless for internal dynamics. We also presented a general formula for measuring the internal energy of the patches in the linear regime (Appendix B) and argued that these should be robust indicators of the internal energy of the final virialized state by showing what happens to the energy as ellipsoids collapse. We paid special attention to modifications to the dynamics and energy with nonzero cosmological constant or nonzero curvature. Although one should be wary of the oversimplification of ellipsoidal dynamics, it is perhaps worthwhile to remind the reader that the tensor virial theorem equations for the interior are similar to ellipsoid equations—except that the orientation of the principal axes may vary.

We showed that inclusion of the external anisotropic tidal field in the ellipsoid approximation lowers the mass by ~20% over spherical collapse models. Although compared with the spherical model, collapse along the axis with the largest strain eigenvalue occurs earlier, the smallest eigenvalue axis collapse is significantly delayed. This anisotropic shear effect is especially pronounced at lower masses, for which e_v values as large as 0.4 are common (see BM4).

We tested other strategies for finding candidate points rather than those chosen by cutting with a threshold f_t the multifiltered density peak list (§ 4.1.1). The simplest was to expand the list by using $f_t = 0$ rather than the conventional spherical collapse value (1.686). We also showed the effects of choosing strain-eigenvalue peaks, λ_{v3} and λ_{v1}; these are of interest for afficianados of the Zeldovich approximation. The main lesson we learned is that the postexclusion lists found with these methods have the same large mass objects, but do differ at the small mass end. The mass functions for the different candidate lists are reasonably close.

A way to improve the final siting of the surviving hierarchical peak points may be to add more candidate peak centers, although still using F peaks as our guide where to lay them. However, the best way to do this so that nearby peaks avoid merging in the candidate list even before exclusion is still under investigation. We believe that an optimized algorithm will lead to approximately the same large mass objects as we find with the F peaks, but expect that we could get a finer determination of the low-mass leftovers. The evidence for this is that a few more low-mass entities were included for F peaks when we dropped the threshold to $f_t = 0$.

Although we have concentrated on Gaussian linear fields, the algorithm also applies to non-Gaussian initial conditions. For a given power spectrum $P_F(k)$, the statistical distribution function for field configurations $\mathscr{P}[F(r)]$ that maximizes the entropy, $-\int \mathscr{P}[F(r)] \ln(\mathscr{P}[F(r)]) \mathscr{D}F(r)$, is the Gaussian one (Bond & Myers 1991). Thus, non-Gaussian distributions concentrate the power in more localized field configurations than the democratic Gaussian one does. In most circumstances, this should make the peaks algorithm work even better (although pathological cases can be constructed).

We pointed out in § 3.3 that using all of the points as sample points was really the logical development of the Press-Schechter (or density field excursion set) approach. Density threshold-crossing points are now connected to their neighbors within a single dynamical entity rather than being scattered into different bins in mass space, as the original excursion set approach does. As well, one may legitimately deal with clustering. Choosing threshold-cut density peaks allows us to sample orders of magnitude fewer points,

but should give essentially the same result as using all points as candidates. We showed that the Press-Schechter method and the hierarchical peak-patch method give similar mass functions, especially at the high-mass end, with a slight lowering of the Press-Schechter critical density threshold f_c (§ 4.2.3). Combined with our internal energy mass relationship (with correction factors derived using detailed constrained field collapse calculations), one may do all of the standard confrontations of models with experiments that people usually do with Press-Schechter, but now with the justification that it is a reasonable fit to the results of the generalized (nonlocal) excursion set theory.

We do not believe that the "faint-end" (low-mass) slopes our method gives will be reliable indicators of what to expect from observations. That is because the high-mass end eats up so much of Lagrangian space that the low-mass end must find the nooks and crannies left over to occupy. And since these are typically not very far from large peak patches, the tidal fields play a large role in defining the fate, and one can probably not suppose that higher order external multipole fields can be ignored. We have long felt that demanding a semi-analytical theory to give a definitive faint end slope was asking too much. The faint end population is clearly sensitive to the detailed physical assumptions about the objects in question, e.g., winds, luminosity-mass relations, surface brightness, the environment, etc.

Our method is basically an adaptive one with crude methods for local and flow dynamics, which can obviously be improved at increasing levels of sophistication. It is clear that the Lagrangian regions that collapse to form a group or cluster are generally not spherical and the asymmetry should get worse for smaller mass and less rare peaks. We note that our binary reduction algorithm actually shaves off sections of the sphere, so that if it is completely surrounded by competing peak points, its final Lagrangian patch will be more polyhedral than spherical. An ambitious project is to search for an algorithm that can efficiently measure the correct Lagrangian region attached to a peak. Perhaps hope lies within the Berger's equation (adhesion) approach to cosmic structure formation, which has had some success in describing collapsed Lagrangian space, even though it is based on the Zeldovich approximation which misses the all-important internal nonlinear tides.

There are many ways in which one can ramp up the computational techniques as we inch towards very large scale adaptive computations of cosmic structure formation. A better interim strategy for the internal dynamics is to do many constrained peak collapses to cover the parameter space, using either pure N-body codes or combined hydrodynamical/N-body codes. This coarsely gridded catalog would then be called upon to calibrate the internal properties. We note that around all of our premerge peak points, we have measurements of the peak shear and peak velocity. Thus, within a given large-peak region, we have locations, shears and velocities for all embedded and nearby smaller mass peaks. The displacement field constrained by all these measurements would have substantially smaller fluctuations because s_f would be highly constrained as well as s_b. Although there will still be some statistical fluctuations, especially at high spatial frequencies, we conjecture that the fate of the primary peak will be effectively defined by this relatively modest tree structure of subpeak and neighboring peak information. How useful such a compressed way of representing a peak patch will be in practice remains to be seen.

The sample constrained peak-patch fields in § 2.2 showed the strong influence of strain and fluctuating field substructure on the patch and the lesser influence of peak velocity. A powerful lesson that can be drawn is that in a general constrained peak realization, centering a simulation volume at the peak point is not always the best strategy, since there may be neighboring peaks or subpeaks that will be better centers. As well, the mass of the region will not necessarily be related to the filter radius used to set up the constrained field. We believe that the postexclusion hierarchical peaks list does a much better job in delivering usable constrained fields for local N-body and hydrodynamical simulations. Of course, one must go farther afield than R_{pk} to do a proper computation. Whatever radius one chooses to go to, an external tidal field should be imposed that is self-consistently determined from the interior displacement field, as we have done for the ellipsoidal model.

An obvious way to improve the candidate-finding algorithm, easily conceivable with the rapidly advancing computing power, is to use very large but low-resolution particle-mesh or multigrid Gauss-Seidel N-body calculations to identify the candidate regions. Eventually, separate high-resolution simulations spawned for each patch to determine the internal state will be possible. In the long run, this grand adaptivity is what the future shall bring. However, even so, having the picture of flowing peak-patch structures that are internally collapsing, merging and growing with time provides a relatively precise language for describing the rare event "intermittent" structure of the medium. Assessing the accuracy of the picture is the task of BM2, while BM3 shows how the tools are used to address questions about clusters in a variety of theoretical models of cosmic structure formation.

APPENDIX A
THE HOMOGENEOUS ELLIPSOID DYNAMICS APPROXIMATION TO PEAK COLLAPSE

In this Appendix, we derive the equations for the ellipsoid model of internal peak-patch dynamics.

To obtain the equations of motion for the flow in the homogeneous ellipsoid approximation, we need the peculiar gravitational acceleration, $g_P \equiv -\nabla_X \Phi_P$, and the peculiar gravitational potential, Φ_P, within the region; Φ_P satisfies the Poission-Newton equation

$$\nabla_X^2 \Phi_P = 4\pi G(\rho_{nr} - \bar{\rho}_{nr}) \equiv 4\pi G \bar{\rho}_{nr} \delta_{nr},$$ (A1)

where ∇_X^2 is the Laplacian operator for the physical Eulerian coordinates X. We have assumed that the only type of matter that can

undergo clustering is nonrelativistic (nr). This includes both cold dark matter and gas. It can also include hot dark matter provided the velocity dispersion is small when the relevant dynamics occurs, as is the case for massive neutrinos. What is not included is vacuum energy (i.e., a cosmological constant) which does not cluster. Boundary conditions for the region (e.g., the external tidal field) are needed to solve equation (A1).

A Taylor expansion of Φ_P in the neighborhood of the peak gives

$$\Phi_P(X) = \Phi_P(X_{pk}) - \sum_i (g_{P,i})_{pk}(X_i - X_{pk,i}) + \sum_{ij} (T_{ij})_{pk}(X_i - X_{pk,i})(X_j - X_{pk,j})/2 . \tag{A2}$$

The contribution $(g_{P,i})_{pk} = -(\nabla_{X^i}\Phi_P)_{pk}$ to the peculiar gravitational acceleration describes the translation of the entire region about the peak, while the gradient of the quadratic term describes the forces distorting the region. The (peculiar) tidal tensor T_{ij} and its traceless part T'_{ij} are defined by

$$T_{ij} \equiv \nabla_{X^i}\nabla_{X^j}\Phi, \qquad T'_{ij} \equiv \nabla_{X^i}\nabla_{X^j}\Phi - \tfrac{1}{3}\delta_{ij}\nabla^2_X\Phi . \tag{A3}$$

Both internal and external tides will be included in T_{ij}.

To get the equation of motion from the potential, including the Hubble expansion, we need to add to Φ_P another term involving the vacuum energy and the background nr-density:

$$\Phi_T \equiv \tfrac{4}{3}\pi G\bar{\rho}_{nr}X^2/2 + \tfrac{4}{3}\pi G(\bar{\rho}_{vac} + 3\bar{p}_{vac})X^2/2 + \Phi_P = \tfrac{4}{3}\pi G\bar{\rho}_{nr}X^2/2 - \tfrac{8}{3}\pi G\bar{\rho}_{vac}X^2/2 + \Phi_P , \tag{A4}$$

From now on, we drop the constant term and the linear gradient term that appear in equation (A2), since the first has no effect on the motion and the second is just center of mass motion. The gravitational potential of a homogeneous ellipsoid of density $\delta\rho_{nr}$ in a known external tidal field $T'_{E,ij}$ is

$$\Phi_P(X) = 4\pi G\delta\rho_{nr} \sum_{ij} \Delta X_i \tfrac{1}{2}\beta_{ij}\Delta X_j/2 + \sum_{ij} \Delta X_i T'_{E,ij}\Delta X_j/2, \qquad \Delta X_j \equiv X_j - X_{pk,j} . \tag{A5}$$

In the principal axes system of the ellipsoid, we have $\Delta X_j \equiv a_j\Delta r_j$, where the a_j are scale factors in each of the three principal directions. The matrix β_{ij} is diagonal in that frame, with eigenvalues b_j given by equation (2.23). (Note that $b_1 + b_2 + b_3 = 0$.) The integrals b_i can be calculated numerically using Carlson's elliptic function,

$$R_D(x, y, z) = \frac{3}{2}\int_0^\infty \frac{d\tau}{(\tau + x)^{1/2}(\tau + y)^{1/2}(\tau + z)^{3/2}} . \tag{A6}$$

Press & Teukolsky (1990) give an efficient routine for calculating it. The b_i can also be expressed in terms of the standard elliptic integrals $E(\theta, k)$ and $F(\theta, k)$ (e.g., Table 2.1 of Binney & Tremaine 1987).

The peculiar tidal tensor entering equation (A5) is

$$T_{ij} = \tfrac{4}{3}\pi G\bar{\rho}_{nr}\delta_{nr}\delta_{ij} + 4\pi G\bar{\rho}_{nr}\delta_{nr}\tfrac{1}{2}\beta'_{ij} + T'_{ext,ij} , \tag{A7}$$

where β'_{ij} denotes the traceless part of β_{ij}, with eigenvalues $b'_i \equiv b_i - \tfrac{2}{3}$. It must agree with the linear tidal tensor $T_{lin,ij}$ given by equation (2.19) for small $a_i - \bar{a}$. In the principal axis system, we have $a_i(t) = \bar{a}(t)(1 - \lambda_{vi})$ to linear order, with $\lambda_{vi}(t) \propto D(t)$. Expanding equation (2.23) to that order gives

$$\frac{b'_i}{2} \equiv \frac{b_i}{2} - \frac{1}{3} = \frac{2}{5}\lambda'_{vi} + \mathcal{O}[D^2(t)], \qquad \lambda'_{vi} \equiv \lambda_{vi} - F/3 . \tag{A8}$$

Thus the contribution $b'_i\delta_{nr}$ in equation (A7) is of second order and hence does not contribute to the traceless linear tide, which must be entirely made up by the external tidal tensor in the linear regime:

$$T'_{ext,ij} = T'_{int,ij} = -4\pi G\bar{\rho}_{nr}e'_{pk,ij} . \tag{A9}$$

Therefore the exterior tidal force arising from the matter outside of the ellipsoid is completely determined by the volume-averaged strain of the ellipsoid. The reason for this is that the displacement field of the points within the ellipsoid responds to internal mass concentrations, which, when volume-averaged, cancel, and to external mass concentrations which do not average out. That is, by agreeing to the initial displacement field within the ellipsoid, one is automatically committed to the form of the external tidal field initially. Of course, to evolve the external tidal field in the nonlinear regime requires another set of equations that does depend upon the specifics of the external region.

The simplest approximation for the full $T'_{\text{ext},ij}$ is to extend the linear evolution as if it continued to operate in the nonlinear regime:

$$\text{linear external tide approximation: } T'_{\text{ext},ij}(t) = [D(t)T'_{\text{ext},ij}(t_0)/D(t_0)] = T'_{\text{int},ij}(t) . \tag{A10}$$

We expect that once the ellipsoid has turned around and begun its collapse, the nonlinear internal tides will overcome the external tides, hence we should not be overly sensitive to this assumption. To test this, we have also considered a simple nonlinear model:

$$\text{nonlinear external tide approximation: } T'_{\text{ext},ij}(t) = 4\pi G\bar\rho_{\text{nr}}\tfrac{5}{4}\beta'_{ij}(t) . \tag{A11}$$

Using equation (A8), we see that this reduces to equation (A10) in the linear regime. Note that once δ_{nr} becomes large, this term will be dominated by the internal dynamics, as required.

In either approximation, the principal axes for the strain tensor remain principal axes for the ellipsoid during evolution. The dynamical equations for the ellipsoid are derived from

$$\frac{d^2}{dt^2}X_i = -\frac{4}{3}\pi G\bar\rho_{\text{nr}}X_i + \frac{8}{3}\pi G\bar\rho_{\text{vac}}X_i - \nabla_{X^i}\Phi_P . \tag{A12}$$

With no vacuum energy, they are given by equation (2.21). More generally, we have [with $X_i(r_i,t) = a_i r_i$]

$$\frac{d^2}{dt^2}a_i = \frac{8}{3}\pi G\bar\rho_{\text{vac}}a_i - 4\pi G\bar\rho_{\text{nr}}a_i\left[\frac{1}{3} + \frac{\delta_{\text{nr}}}{3} + \frac{b'_i}{2}\delta_{\text{nr}} + \lambda'_{\text{ext}i}\right], \tag{A13a}$$

$$\text{linear external tide approximation: } \lambda'_{\text{ext}i}(t) \equiv \lambda'_{vi}(t) , \tag{A13b}$$

$$\text{nonlinear external tide approximation: } \lambda'_{\text{ext}i}(t) = 5b'_i(t)/4 , \tag{A13c}$$

The initial conditions are given by equation (2.24). Thus to characterize an evolution, we need F_{pk}, e_v, and p_v, and the initial redshift.

To gain insight into how equation (A13a) bridges the linear and nonlinear regimes, we rewrite it in terms of nonlinear strain factors, $\lambda_{\text{NL}i} \equiv 1 - a_i/\bar a$, which obey

$$\ddot\lambda_{\text{NL}i} + 2H\dot\lambda_{\text{NL}i} = 4\pi G\bar\rho_{\text{nr}}\left[\left(\frac{1}{3}\delta_{\text{nr}} + \lambda'_{\text{E}i}\right) + \frac{b'_i}{2}\delta_{\text{nr}}\right](1 - \lambda_{\text{NL}i}), \qquad \delta_{\text{nr}} = \prod_j(1 - \lambda_{\text{NL}j})^{-1} - 1 . \tag{A14}$$

The $\lambda_{vi}(t)$ obey the same linear growth equation as $D(t)$:

$$\ddot\lambda_{vi} + 2H\dot\lambda_{vi} = 4\pi G\bar\rho_{\text{nr}}\lambda_{vi} . \tag{A15}$$

Thus, in the linear regime, $\lambda_{\text{NL}i} = \lambda_{vi}(t)$ provided $\lambda'_{\text{E}i}(t)$ reduces to $\lambda'_{vi}(t)$. (Note that for cosmologies that are not Einstein–de Sitter, $D \neq a$, so we must integrate equation (A15) for λ_{vi}, i.e., for D. Although a first integral of the linear evolution equation exists for simplified cosmologies (e.g., equation [B8]), we generally solve coupled ODE's for D/a, $d\ln D/d\ln a$, and any energy densities for decaying particles or decay products.

As described in § 2.1, we have chosen to stop the calculations by using a radial freezeout factor f_r (Bond, Szalay, & Silk 1988): that is, for $\dot a_i < 0$, once $a_i = f_r\bar a$ at some redshift $z_{c,i} = \bar a^{-1} - 1$, we thereafter keep a_i at that value. Stopping collapse by relying on artificial pressure and dissipation terms has not proved to be very satisfactory. Our virialization strategy makes the final shape triaxial. There are many strategies that one can try for freezeout. For example, using $a_{\text{eq},3}$ to determine how far we allow the 2 and 1 axes to collapse gives final spherical states and somewhat larger overdensities than the f_r strategy. However, the different strategies change the 1-axis collapse redshift, $1 + z_{c,1}$, by at most a few percent. For $f_r = 0.177$, the value adopted for this paper, the overdensity of a spherical collapse is 179, the usual spherical top-hat collapse value. Changing f_r to 0.1 changes $1 + z_{c,1}$ by a percent or so for $e_v = 0.1$, but by 4%–5% for $e_v = 0.3$, and this depends somewhat upon cosmological model. With $f_r = 0.01$, the error can be 10%–20%, depending upon the model, but the overdensities are unrealistically high, more than 10^6. The calculation must be begun at high redshift, since the Zeldovich (linear) setup for the initial conditions becomes inaccurate, leading to a few percent error, otherwise.

There is an interesting history of using the homogeneous ellipsoid as an approximation to triaxial collapses in cosmology. Icke (1973) considered the evolution of expanding spheroids. White & Silk (1979) used equation (A5) with no external tide, but required initial anisotropy to be built in. Peebles (1980, § II.20) used the ellipsoid with no external tide and assumed there was no matter outside, but correctly cautioned that it could be used to gain insight only for nonlinear evolution, and could not be applied

to the linear regime. We have shown that the self-consistent external tidal force is needed to recover the Zeldovich approximation in the linear regime.

Figure 14 shows how the collapse redshifts computed using the homogeneous ellipsoid equations vary with changing parameters and approximations. Figure 14a compares the nonlinear approximation, equation (A13c), with linear evolution of the exterior tidal tensor (which is used in the rest of the panels). Figure 14b shows an isolated ellipsoid (with no external mean background density and no external tide). One can see the similarity in the results for the nonlinear and linear tide approximations, but also the dramatic difference that can occur if the linear regime is not properly reproduced by the equations, as in Figure 14b. Figures 14a, 14b, and 14c are for a flat $\Omega_{nr} = 1$ model. The starting redshift was taken to be 40, but this does not matter if the external tides are properly included. However, if they are not, as in Figure 14b, the degree of anisotropy damping depends upon when one begins.

Figure 14 also compares the $\Omega_{nr} = 1$ evolution for models (Figs. 14d–14f) with nonzero cosmological constant, $\Omega_{vac} = \Lambda/(8\pi G)$, and (Figs. 14g–14i) with negative curvature. We choose $\Omega_{nr} = 0.2$ in both cases, and take $\Omega_{vac} = 0.8$ for a flat cosmology in the former case. Many workers have considered the evolution of the spherical model with nonzero Λ (Peebles 1984; Weinberg 1987; Martel & Wasserman 1990; Martel 1991; Lahav et al. 1991; Lilje 1991). We have checked our $\Lambda \neq 0$ calculations for the sphere ($e_v = p_v = 0$ limit) with the results given by these authors. Even when we use the spherical approximation for our Monte Carlo calculations, we have found it simplest to tabulate numerical results for the collapse redshift as a function of F_{pk}, rather than to construct fitting formulae. For the spherical case with nonzero Λ, the Eulerian radius $X(r, t)$ obeys
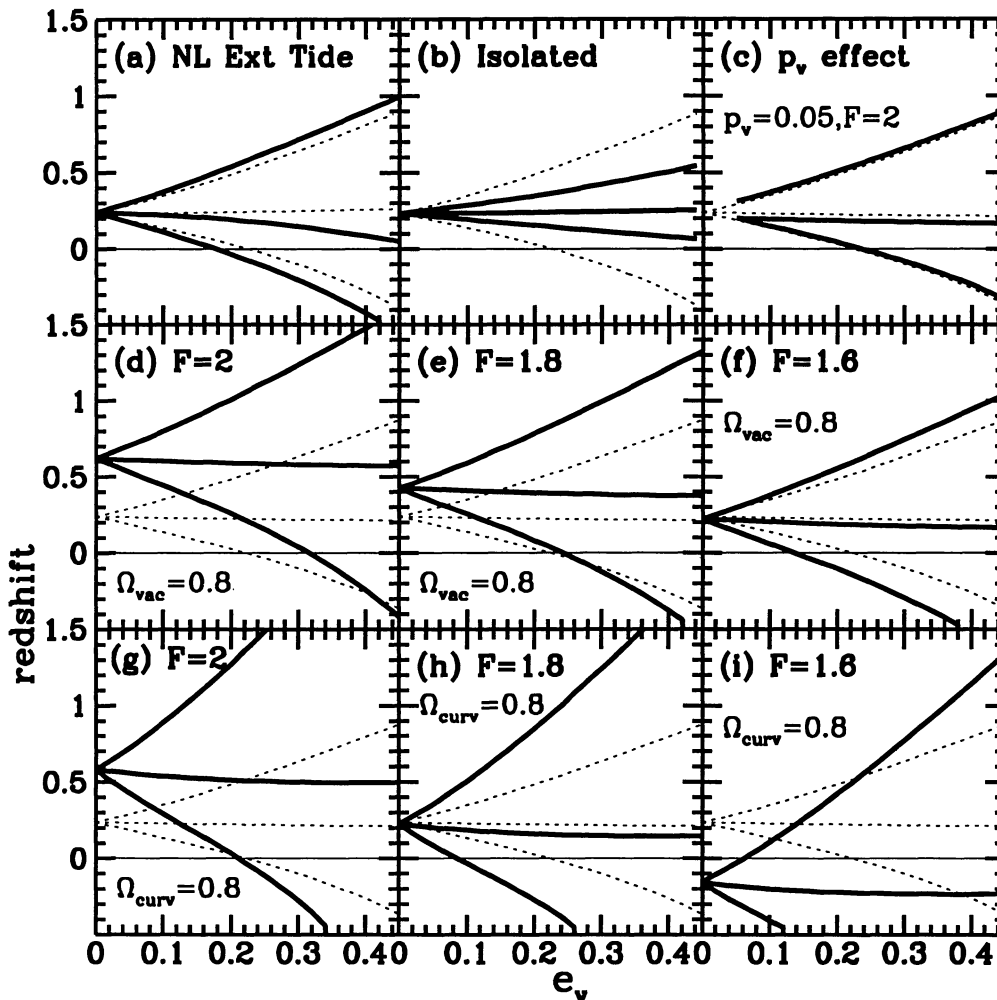

FIG. 14.—The panels show how the collapse redshifts for the three ellipsoidal axes as a function of the initial ellipticity e_v vary as the approximations and parameters change. In all panels the light dotted curves show the standard case for a $\Omega_{nr} = 1$ CDM model with $F = 2$ and $p_v = 0$ for reference. (a) The nonlinear external tide approximation. (b) The evolution if the ellipsoid is isolated. (c) The effect of finite prolaticity p_v for linear external tide. The prolaticities are generally small. The rest of the panels illustrate how ellipsoids in low Ω_{nr} universes (here 0.2) with the same F collapse much earlier than in $\Omega_{nr} = 1$ ones. Panels (d–f) have nonzero cosmological constant $\Omega_{vac} = 0.8$ and values of linear overdensity $F = 2$, 1.8, 1.6, as indicated. Panels (g–i) have nonzero curvature $\Omega_{curv} = 0.8$ and the same range of F. The results are independent of the Hubble parameter. The scaling of $1 + z$ with F no longer holds as in the $\Omega_{nr} = 1$ case.

$$\ddot{X}(r,t) = \tfrac{8}{3}\pi G\rho_{\mathrm{vac}}X(r,t) - \tfrac{4}{3}\pi G\bar{\rho}_{\mathrm{nr}}\bar{a}^3 r^3/X^2(r,t)\,. \tag{A16}$$

Unperturbed patches of the universe that were initially decelerating will eventually accelerate (i.e., inflate) when the redshift falls below $z_\Lambda = (2\Omega_{\mathrm{vac}}/\Omega_{\mathrm{nr}})^{1/3} - 1$. A perturbed patch will also accelerate and thus certainly never turn around if the gravitating nr-mass of the perturbation cannot overcome the negative pressure effects; i.e., if X can fall below $X_\Lambda = r/(1+z_\Lambda)$. Of course the turnaround requirement is more stringent than this. For the spherical case with nonzero Λ, collapse is again halted using f_r. If we use this device for the cold collapse calculation, with $f_r = 0.18$, at which point an overdensity of 179 is obtained, the required linear density contrast is $F(z) = 1.61$, not 1.69, which translates into a 5% rise in the virialization redshift over the usual value adopted.

One can think of the evolutionary equation (A13a) as a tensor virial theorem describing the average behavior of the matter within the initial sphere of radius R_{pk} and which therefore integrates over the interior profile. However, the true dynamics of the collapsing region is much more complex. In particular, if there is a profile then the external tide may not be lined up with the internal ellipsoidal shells. Although one can treat specific nonuniform profiles by concentric ellipsoidal shells for isolated objects, as described in Chandrasekhar (1969) and Binney & Tremaine (1987), we do not believe it is worthwhile to pursue this extra complication in the cosmological setting, since we know that nonalignment of shears and tides plays an important role. Of course, nonuniformity in the spherically symmetric case is straightforward to treat and does illustrate that solving tensor virial equations for spherical regions of various radii r is exact in this case.

<div align="center">

APPENDIX B

ESTIMATIONS OF THE INTERNAL ENERGY OF PEAK PATCHES

</div>

One of the most difficult tasks we have encountered in developing the hierarchical peaks approach is to accurately predict virialized velocity dispersions from measurements made in the initial conditions. Our philosophy is to use measures of nearly conserved quantities.

For a flat $\Omega_{\mathrm{nr}} = 1$ cosmology, as long as there is no transport from an isolated spherical region of radius R_{pk}, there will be at least two conserved quantities for that region, its mass and internal (binding) energy. If there is vacuum energy, nonzero global curvature or mixing (shell crossing through R_{pk}), conservation will not apply. Further, the energy of gas can be increased through the action of external pressure and from heat input through supernovae, etc., and lost through radiation and wind outflows, etc. Even in these cases, we expect that we can infer some of the features of the final region by measuring the binding energy in the initial field.

Internal energy of nonrelativistic matter is not conserved when the cosmology differs from the flat $\Omega_{\mathrm{nr}} = 1$ variety. For high-redshift evolution this is irrelevant, but it is important to consider these effects for clusters in $\Lambda \neq 0$ or open cosmologies. The internal self-energy in nonrelativistic matter for the region within the initial radius R_{pk} is

$$E_{\mathrm{nr}} = \int \rho_{\mathrm{nr}}(X)d^3X\,\tfrac{1}{2}\sum_i V_i^2 - \tfrac{1}{2}\int d^3X d^3X' \frac{G\rho_{\mathrm{nr}}(X)\rho_{\mathrm{nr}}(X')}{|X-X'|}\,. \tag{B1}$$

We consider the energy associated with the vacuum below. The integration regions are the Eulerian-space distortions of the initial Lagrangian space $r < R_{\mathrm{pk}}$. Since $\rho_{\mathrm{nr}}(X)d^3X = \bar{\rho}_{\mathrm{nr}}\bar{a}^3 d^3r$, they reduce to integrations over the Lagrangian space sphere, which considerably simplifies the subsequent development, but is not essential.

We first wish to determine the internal nr-energy in the linear regime. For this we need the linear expansions,

$$V_i = \dot{a}r_i - \dot{a}(1 + H_D/H)s_i\,, \qquad |X-X'|^{-1} \approx a^{-1}|r-r'|^{-1} + a^{-1}|r-r'|^{-3}[s(r)-s(r')]\cdot[r-r']\,. \tag{B2}$$

We also need the Friedmann equation

$$H^2 = \left(\frac{\dot{a}}{a}\right)^2 = H_0^2(\Omega_{\mathrm{nr}}a^{-3} + \Omega_{\mathrm{vac}} + \Omega_{\mathrm{curv}}a^{-2})\,. \tag{B3}$$

The internal nr-energy for a general perturbation is then

$$E_{\mathrm{nr}}/M_{\mathrm{nr}} = E_{\mathrm{nr}}^{(0)}/M_{\mathrm{nr}} + E_{\mathrm{nr}}^{(P)}/M_{\mathrm{nr}}\,, \tag{B4a}$$

where the unperturbed energy is

$$\frac{E_{\mathrm{nr}}^{(0)}}{M_{\mathrm{nr}}} = \frac{1}{2}H_0^2\langle r^2\rangle_V[\Omega_{\mathrm{vac}}\bar{a}^2 + \Omega_{\mathrm{curv}}]\,, \qquad \langle r^2\rangle_V \equiv V^{-1}\int r^2 d^3r = \frac{3}{5}R_{\mathrm{pk}}^2 \tag{B4b}$$

and the perturbed energy is

$$\frac{E_{\mathrm{nr}}^{(P)}}{M_{\mathrm{nr}}} = -H_0^2 \langle \boldsymbol{r}\cdot(\boldsymbol{s}-\boldsymbol{s}_{\mathrm{pk}}) \rangle_V \bar{a}^{-1} [(\Omega_{\mathrm{vac}}\bar{a}^2 + \Omega_{\mathrm{curv}})\bar{a}(1 + H_D/H) + \Omega_{\mathrm{nr}}(3/2 + H_D/H)] \tag{B4c}$$

$$\equiv \varepsilon_P[\boldsymbol{s}] - H_0^2 \langle \boldsymbol{r}\cdot(\boldsymbol{s}-\boldsymbol{s}_{\mathrm{pk}}) \rangle_V \Omega_{\mathrm{vac}}\bar{a}^2 . \tag{B4d}$$

The unperturbed energy is, of course, zero for an Einstein–de Sitter cosmology, and is constant for one with curvature, but increases with time if vacuum energy is included, because "pdV" work pumps energy in with expansion because the vacuum pressure is negative. The perturbed energy is negative if the radial component of the displacement relative to the peak point, $\boldsymbol{s}-\boldsymbol{s}_{\mathrm{pk}}$, is positive, that is, if the peculiar velocity relative to the center is inward pointing. In linear theory almost all of these terms arise from the kinetic energy. Only $\Omega_{\mathrm{nr}}/2$ of the term in square brackets arises from the gravitational potential energy. Recall that $H_D = \dot{D}/D$. The quantity ε_P is the perturbation energy after removal of an interaction energy between the nonrelativistic particles and the vacuum that we identify below. Using $F = \nabla\cdot\boldsymbol{s}$, and the spherical nature of the volume, we can express the volume-averaged term appearing in equation (B4c) in terms of the average overdensity within radius r, $\bar{F}(<r)$:

$$\langle \boldsymbol{r}\cdot(\boldsymbol{s}-\boldsymbol{s}_{\mathrm{pk}}) \rangle_V = \frac{1}{3} \langle \bar{F}(<R)R^2 \rangle_V, \qquad \bar{F}(<R) \equiv \frac{1}{4\pi R^3/3} \int_0^R r^2 \, dr \, d\Omega F(\boldsymbol{r}, t) . \tag{B5}$$

Here $d\Omega$ is the solid angle element. Thus the perturbed internal binding energy per mass within R_{pk} can be expressed as

$$\frac{E_{\mathrm{nr}}^{(P)}}{M_{\mathrm{nr}}}(<R_{\mathrm{pk}}) = -\frac{1}{2}(H\bar{a}R_{\mathrm{pk}})^2 F_{\mathrm{pk}} S(R_{\mathrm{pk}})(3 + 2H_D/H)/5 + \frac{1}{2}(H_0 R_{\mathrm{pk}})^2 F_{\mathrm{pk}} S(R_{\mathrm{pk}}) \frac{(\Omega_{\mathrm{vac}}\bar{a}^2 + \Omega_{\mathrm{curv}})}{5} , \tag{B6}$$

where $S(R_{\mathrm{pk}})$ is given by equation (2.27b). [Note that for a truly homogeneous distribution, we would have $S(R_{\mathrm{pk}}) = 1$.] The unperturbed energy is not constant if $\Lambda \neq 0$ and the perturbed energy is not constant if either $\Lambda \neq 0$ or the curvature is nonzero. However, when account is taken of the gravitational effect of the vacuum on the nr-matter, which adds a term $E_{v-\mathrm{nr}}$ to the relevant energy, only the constant curvature energy remains for the unperturbed part, and only ε_P remains for the perturbed part, which also turns out to be constant:

$$\frac{E_{\mathrm{nr}}}{M_{\mathrm{nr}}} + \frac{E_{v-\mathrm{nr}}}{M_{\mathrm{nr}}} = \frac{1}{2} H_0^2 \langle r^2 \rangle_V \Omega_{\mathrm{curv}} + \varepsilon_P[\boldsymbol{s}], \qquad \varepsilon_P[\boldsymbol{s}] = -\frac{1}{2}(H_0 R_{\mathrm{pk}})^2 \frac{F_{\mathrm{pk}}}{D} S(R_{\mathrm{pk}}) \Omega_{\mathrm{nr}} , \tag{B7}$$

where we have made use of

$$\frac{D}{a}\left[\frac{2}{5}\Omega_{\mathrm{nr}}(3/2 + H_D/H) + \frac{2}{5}\Omega_{\mathrm{vac}}\bar{a}^3 + \frac{2}{5}\Omega_{\mathrm{curv}}a(1 + H_D/H)\right] = \Omega_{\mathrm{nr}} , \tag{B8}$$

a first integral of the equation of cold linear evolution,

$$\ddot{D} + 2H\dot{D} - 4\pi G\bar{\rho}_{\mathrm{nr}}D = 0 . \tag{B9}$$

We now show how this extra term which ensures constancy in linear evolution comes about, and we check under what circumstances the internal energy is conserved during nonlinear evolution. For a homogeneous ellipsoid, the internal energy as defined by equation (B1) is

$$\frac{E_{\mathrm{nr}}}{M_{\mathrm{nr}}} = \langle r^2 \rangle_V \frac{1}{3}\sum_i \frac{\dot{a}_i^2}{2} - \frac{4}{3}\pi G\rho_{\mathrm{nr}}\frac{b_0}{2}\langle r^2 \rangle_V, \qquad b_0(a_j) \equiv a_1 a_2 a_3 \int_0^\infty \frac{d\tau}{\prod_{m=1}^3 (a_m^2 + \tau)^{1/2}} . \tag{B10}$$

However, if we form the virial by taking the equation of motion for $\ddot{X}_i$, multiplying by $\dot{X}_i$, and summing over i, we obtain

$$\frac{d}{dt}\left(\frac{E_{\mathrm{nr}}}{M_{\mathrm{nr}}} + \frac{E_{v-\mathrm{nr}}}{M_{\mathrm{nr}}}\right) \equiv \dot{q}_{\mathrm{tide}} , \tag{B11a}$$

where the energy

$$\frac{E_{v-\mathrm{nr}}}{M_{\mathrm{nr}}} \equiv -\frac{4}{3}\pi G\bar{\rho}_{\mathrm{vac}}\langle r^2 \rangle_V \frac{1}{3}\sum_i a_i^2 . \tag{B11b}$$

associated with the gravitational effects of the vacuum must be added to E_{nr} to form a conserved quantity in linear theory. The heating rate,

$$\dot{q}_{\text{tide}} \equiv 4\pi G \bar{\rho}_{\text{nr}} \langle r^2 \rangle_V \frac{1}{3} \sum_i a_i \dot{a}_i \left(\frac{b_i'}{2} - \lambda_{\text{E}i}' \right), \tag{B11c}$$

arising from the internal shear and external tide breaks energy conservation. It vanishes in the linear regime, since a_i is replaced by $\bar{a}$ and the sums over i of b_i' and $\lambda_{\text{E}i}'$ are both zero. For the same reason, the term always vanishes in the spherical dynamics approximation.

For ellipsoids in the nonlinear regime, $\dot{q}_{\text{tide}}$ can be quite significant, as we illustrate by expanding to second order. Letting $a_i = \bar{a}(1 - \lambda_{vi})$, using $b_i' = 4\lambda_{vi}'/5$ and $\lambda_{\text{E}i}' = \lambda_{vi}$ in the linear regime, and recognizing that sums over i of the quadratic nonlinearities in b_i' and $\lambda_{\text{E}i}'$ (if it exists) vanish, we have

$$\text{in quadratic order: } \dot{q}_{\text{tide}} = 4\pi G \bar{\rho}_{\text{nr}} \langle r^2 \rangle_V \bar{a}^2 H \frac{(2 + H_D/H)}{5} \sum_i [\lambda_{vi}']^2 . \tag{B12}$$

Thus the first apparent effect of shear on the ellipsoid is to add heat, which makes the energy less negative. In BM2, we find that Couchman's N-body groups have internal energy 12% lower than those computed from the initial internal energy of the corresponding peaks (and velocities 6% lower).

The heat input is quite complex in the fully nonlinear regime:

$$\dot{q}_{\text{tide}} = \frac{4}{3} \pi G \bar{\rho}_{\text{nr}} \langle r^2 \rangle_V \bar{a}^2 \sum_i (\lambda_{\text{E}i}' - b_i'/2) \{ \lambda_{\text{NL}i}'[(1 - F_{\text{NL}}/3)H - \dot{F}_{\text{NL}}/3] + \dot{\lambda}_{\text{NL}i}'(1 - F_{\text{NL}}/3) - [\lambda_{\text{NL}i}']^2 H - \lambda_{\text{NL}i}' \dot{\lambda}_{\text{NL}i}' \}, \tag{B13a}$$

$$F_{\text{NL}} \equiv \sum_i \lambda_{\text{NL}i} . \tag{B13b}$$

In this case, it is not clear that the sign is always in the direction of adding energy to the region.

If we ignore this nonlinear tide heating/cooling, we can equate the final state quantities to the zeroth and first-order perturbation values, equation (B7). The internal binding energy in the final virialized state has no bulk kinetic energy, only "thermal" energy, including the gravitational effect of the residue vacuum. Because vacuum energy density does not change during expansion or collapse, this energy is not very large in the compact virialized state. For spherical collapse into a final state of (isolated) virial equilibrium with kinetic energy per mass $K_f/M_{\text{nr}} \equiv v_E^2/2$ and no curvature, we have $\varepsilon_P = -v_E^2/2 - 4\pi G \rho_{\text{vac}} X_f^2$, where X_f is the final-state equilibrium radius. A similar result holds for homogeneous ellipsoids. With the curvature term, the equation of the initial and final energies is

$$\tfrac{1}{2} H_0^2 \langle r^2 \rangle_V \Omega_{\text{curv}} + \varepsilon_P[s] = -\tfrac{1}{2} v_E^2 + \tfrac{1}{2} H_0^2 \langle r^2 \rangle_V \Omega_{\text{vac}} \sum_i a_{\text{eq},i}^2 , \tag{B14}$$

where $a_{\text{eq},i}$ is the final-state ellipsoidal scale factor of axis i. The Ω_{vac} correction factor is usually negligible, however: with a collapse factor $f_r \sim 0.18$, the correction to v_E is only $\sim 0.006 \Omega_{\text{curv}}/[(1 + z_{c1})\Omega_{\text{nr}}]$.

The internal energy of a region is one that we have had considerable success with when we compare in detail with internal energies of N-body groups (BM2). However, we find that Couchman's P^3M groups have, on average, velocity dispersions that are $\sim 11\%$ higher than those inferred from the internal energy, which should be accurate if the regions are virialized and relatively isolated. On the other hand, we have confirmed with constrained field collapses that isolated groups do have both velocity determinations in agreement. Of course, the P^3M groups may be out-of-equilibrium. This is certainly the case if there have been recent major mergers. However, it may also be that the nonlinear tidal energy which we are not currently including in our estimates can draw enough energy from the system (make it more bound) to explain the discrepancy, although we showed that the lowest order correction is to pump energy into the system. So far, we have not found a fully satisfactory way to include the influence of exterior tides upon the energy.

APPENDIX C
CONSTRAINED-FIELD SIMULATIONS OF A PEAK PATCH

Bertschinger (1987) was the first in cosmology to show how to construct a realization of a Gaussian random field which obeys various constraints, using Monte Carlo numerical methods borrowed from lattice gauge theory. If one attempts to apply too many constraints on the field, the relaxation rate of his algorithm to a true realization of the constrained field slows down. For peaks, we have at least $2 \times (1 + 3 + 5)$ constraints of strong interest, for F_{pk}, s_{pk}, $e_{\text{pk},ij}'$ and for $\nabla^2 F$, $\nabla_i F$, $[\nabla_i \nabla_j F]'$. These are (smoothed) scalar, vector or tensor fields, evaluated at the peak site. Therefore a multipole expansion is suggested for the profiles in the neighborhood of the peak (BBKS; Bond 1987a), for then only the monopole, dipole, and quadrupole components will be affected by the constraints. All higher multipoles are just independent unconstrained Gaussian random fields, realizable in the standard way. We have developed a simple efficient numerical algorithm for calculating peak quantities based upon multipole expansion of the fields

about the peak point. The first step is to determine the components of the fields in k-space, which takes essentially no time, and the second is to do a direct transform to real space, which is slow. The multipole method is well suited for analytic and semi-analytic work, e.g., for calculating peak-peak and peak-mass correlation functions and alignments (Bond 1986, 1987a; BM4). Binney & Quinn (1991) have used a different implementation of the multipole method for realizing constrained fields and have also exploited the analytic features of the approach to estimate peak angular momentum (Quinn & Binney 1992).

A simpler approach for numerically realizing constrained fields was introduced by Hoffman & Ribak (1991). They begin with *any* unconstrained realization of the field and measure the values that the constraint operators take in that realization. They then *subtract* from the input field the mean background field derived with the *unwanted* constraints, and then *add* to it the mean background field derived with the *wanted* constraints. If one can ensure that adequate k-space coverage is obtained, then this is the method of choice. It is also excellent for more complicated situations than the single peak one considered here, for example, constraining a field to have peaks at many different sites in the computational volume. The Hoffman-Ribak method for peaks at many sites has been implemented by van Haarlem & van de Weygaert (1993).

In the case we consider here, in which we use direct Fourier transform methods to lay down the long wavelengths for even unconstrained fields (because the Fast Fourier transform has such poor wavelength coverage at low k), the Hoffman & Ribak (1991) method results in little saving. We now sketch our implementation of the multipole method that was used to construct the constrained fields described in this section. Consider the multipole expansion of F, in k-space, $\tilde{F}_{LM}(k)$. Each $\tilde{F}_{LM}(k)$ is a one-dimensional random field in the radial wavenumber $k = |\boldsymbol{k}|$. Clearly, the ν and x constraints affect only $\tilde{F}_{00}(k)$, the s and ∇F constraints affect only $\tilde{F}_{1M}(k)$ and the anisotropic strain and $[\nabla_i \nabla_j F]'$ constraints only affect $\tilde{F}_{2M}(k)$. All $\tilde{F}_{LM}(k)$ for $L > 2$ are unconstrained and statistically independent from each other and are therefore easy to realize. The constraints that do act upon $\tilde{F}_{LM}(k)$ for $L \le 2$ are independent of those acting upon $\tilde{F}_{LM'}(k)$ if $M' \ne M$. Thus the constraints split into at most 2 per (real) LM coefficient for $L \le 2$. Imposing reality upon the multipole components restricts $M \ge 0$, but $\tilde{F}_{L,-M}(k)$ enters into two independent linear combinations with $\tilde{F}_{LM}(k)$ to define two independent real field components.

Different k's must be correlated to allow the constraint operators to have fixed values. That is, the $\langle \tilde{F}_{LM}(k)\tilde{F}_{LM}(k')|\text{constraint}\rangle$ is nonzero for $k \ne k'$ as it is for the unconstrained components. However, because we are dealing with a one-dimensional Gaussian random field with just two constraints, once can easily and rapidly diagonalize this correlation matrix and expand these constrained field components in statistically independent modes. The expansion coefficients are the matrix elements of the inverse square root of $\langle \tilde{F}_{LM}(k)\tilde{F}_{LM}(k')|\text{constraint}\rangle$.

These normal modes have two parts, a statistically averaged mean background field and the variance about it. Only the former depends upon the specific value of the constraints, while the latter is evaluated by independent random number choices for each of the modes.

Since we are interested in accurately sampling the long wavelength modes in a peak patch, we have paid considerable attention to k-space sampling procedures in our implementation of the multipole method, and more generally for realizing any field, whether constrained or not. For the longest wavelengths that affect the constraint, we perform a direct multipole calculation of the fields $F_b(r, \theta, \phi)$ and $\boldsymbol{s}_b(r, \theta, \phi)$. This involves a direct sum over many $Y_{LM}(\theta, \phi)$ and spherical Bessel functions $j_L(kr)$, which is as inefficient as direct Fourier transform, but quite familiar from constructing microwave background realizations. For this component of the field, we use logarithmic spacing for the radial k bins.

To deal with the split between the fluctuating and background fields, it is advantageous if they are uncorrelated (BBKS), hence we make a cut in k-space at k_b. For the $k < k_b$ part, the constrained field is layed down by an expansion in spherical Bessel functions and spherical harmonics (~ 30 multipoles and ~ 100 radial bins in k are sufficient here). For the calculations shown in the figures, we used $k_b^{-1} = 2\ h^{-1}$ Mpc, which is small compared with the $5\ h^{-1}$ Mpc Gaussian filter. Although the patch shown is only $30\ h^{-1}$ Mpc across, corresponding to a $4.8\ h^{-1}$ Mpc fundamental mode, waves as large as $k^{-1} = 50\ h^{-1}$ Mpc were added. To do this calculation solely with an FFT would require a box about an order of magnitude larger. For $k > k_b$, the influence of the constraint is ignored, which is accurate for the k_b choice here. For the fluctuating component, the Fast Fourier Transform is used to lay down the high wavenumbers efficiently (it is a $\sim k^3$ sampling procedure). This is augmented with direct (brute force) Fourier transform calculations using a combination of a hybrid power law (with linear $\sim k$ and quadratic $\sim k^2$ pieces) sampling at intermediate k and logarithmic ($\sim \ln k$) sampling at low k to ensure excellent coverage in k-space. We discuss how these non-FFT sampling procedures are combined with FFT sampling in Appendix D, since they are used to add very long wavelength modes to the density and displacement fields needed for catalog construction. One can also easily implement these three sampling procedures in the Hoffman-Ribak approach to constrained-field realizations, which we have also done.

The figures illustrating the structure of constrained fields shown in Figures 2, 3, 4, and 5, were described in § 2.2. Here we add a few more comments on Figure 3. For the high shear case (Figs. 3a–3b) we included some nonalignment of the $\nabla_i \nabla_j F$ principal axes with the principal axes of the strain (taken to be the Cartesian axes) to show the resulting contour distortion. The parameter e_d was also increased with e_v in accord with mean field theory. We have not shown the independent effect of increasing $-\nabla^2 F$. When one does, one gets increasingly sharp and concentrated contours, as expected. To satisfy the other constraints, the voids just outside become deeper and deeper.

The high-velocity examples (Figs. 3c–3d) show large-scale coherence: at the cutoff of $1\ h^{-1}$ Mpc, the coherence scale for the displacement field ($\sqrt{3}\,\sigma_{-1}/\sigma_0$) is $2.7\ h^{-1}$ Mpc for this CDM model, and the rms displacement is $4.7\ h^{-1}$ Mpc. There must be density enhancements somewhere doing the pulling (or a void doing the pushing). However these can arise from outside the patch shown, from long wavelengths. Note that to house a full wavelength within the entire region shown, the wavevector required (the "fundamental mode") is only $k^{-1} = 5\ h^{-1}$ Mpc. Of course, what is also not shown is the flow out of and into the page, due to other nearby

peaks not visible in this planar cut. What is rather remarkable is that when we remove the box-averaged flow, what is left looks relatively similar to Figure 2 d. That is the deviations in the flow from bulk really do converge nicely in the region within the circle. This is defined largely by the anisotropic peak-strain constraint. Thus, although the image in Figure 3 d of fast matter overtaking slower matter creating a structure like a breaking wave has some correctness, in the bulk flow frame something like an ellipsoidal approximation should work.

A lesson should be drawn from high-speed peak realizations such as this one: high-speed peaks are very likely to be near other major mass concentrations. Such a peak is a good candidate for merging, and it is not a good idea to center a computation on it.

APPENDIX D
THE IMPORTANCE OF THE "BACKGROUND" LONG-WAVELENGTH FIELD

For the simulation "box", the lattice size a_L and our chosen number of grid cells $N_{\text{box}}^3 = 128^3$ determines the box length $L_{\text{box}} = N_{\text{box}} a_L$. The fundamental wavenumber for the box is $k_{\text{fund}} = 2\pi/L_{\text{box}}$. The Nyquist wavenumber is $k_{\text{Nyq}} = \pi/a_L = N_{\text{box}} k_{\text{fund}}/2$. For the cases we show in this paper, we use the standard cold dark matter spectrum ($\Omega_{\text{cdm}} = 1$, $h = 0.5$) with $\sigma_8 = 0.97$ (this is used in the comparison with the Couchman simulation given in BM2). Clusters are defined predominantly by waves with wavenumbers in the range $k^{-1} \sim 3$–$8\ h^{-1}$ Mpc, groups from smaller k^{-1}. A Nyquist wavenumber of $k_{\text{Nyq}}^{-1} = 0.5\ h^{-1}$ Mpc therefore seems to be a safe choice. The box then has $L_{\text{box}} \approx 200\ h^{-1}$ Mpc, which is what we chose. The fundamental mode has wavenumber $k_{\text{fund}}^{-1} = 31.8\ h^{-1}$ Mpc. The amount of power in the linear density fluctuation on this scale is measured by $\sigma_0(k_{\text{fund}}^{-1}) = 0.05\sigma_8$. The contribution to the rms velocities is $\sigma_v(k_{\text{fund}}^{-1}) = 244\sigma_8$ km s^{-1}, and to the rms displacement is $\sigma_{-1}(k_{\text{fund}}^{-1}) = 1.2\sigma_8\ h^{-1}$ Mpc. Note that $\sigma_v = H_D\sigma_{-1}$. For a typical cluster-scale wavevector, $k^{-1} \sim 4\ h^{-1}$ Mpc, we have $\sigma_0 = 0.97\sigma_8$ and $\sigma_v = 751\sigma_8$ km s^{-1}. For 3σ peaks of the background density field, we get only an 0.15 correction to F_{pk}, a relatively small but not negligible correction to the value $f_c = 1.686$, since it can modulate the number of peaks over these very large scales. More significantly, when we map into redshift space, there can be displacement effects associated with the very long waves which should be included to get the correct ultralarge clustering pattern.

Another important facet of the ultralong wavelength modes is this: they ensure coherence of structures from box to box. For F_f and s_f, we choose different random phases for each box. Otherwise we would get the same periodic pattern repeating itself from box to box, which is obviously undesirable. We actually choose to overnest the boxes and do not quite go to the edge to ensure that wraparound does not occur. Nonetheless there is no cross-box coherence of clusters. We can get this only from the ultralong wavelength power.

Although this is not a fundamental problem for clusters because of the large size that we can take the box to be relative to the correlation length of clusters, we do lose large scale correlation power this way. This underscores why having an accurate semi-analytic theory is so important.

For galaxy scale halos, we may wish to have $k_{\text{Nyq}}^{-1} = 0.05\ h^{-1}$ Mpc, which gives 20 h^{-1} Mpc boxes and $k_{\text{fund}}^{-1} = 3.2\ h^{-1}$ Mpc. We then have a contribution to the rms density field of $\sigma_0(k_{\text{fund}}^{-1}) = 1.2\sigma_8$, to the rms velocities of $800\sigma_8$ km s^{-1}, and to the rms displacement of $4\sigma_8\ h^{-1}$ Mpc. The rms values k-space filtered at the Nyquist frequency are $12\sigma_8$, $990\sigma_8$ km s^{-1}, and $5\sigma_8\ h^{-1}$ Mpc, respectively. A typical wavenumber for a galaxy scale is $k^{-1} \sim 0.3\ h^{-1}$ Mpc, which gives $6\sigma_8$ and a rms displacement of $4.9\ h^{-1}$ Mpc. The modulation of the density peak number can therefore be quite significant and most of the displacement comes from the long waves. This is fundamental to include if one would like to determine the clustering associated with large-scale wall and filament formation at very high redshift, for example.

For F_b, we store n_{k+} wavevectors $\boldsymbol{k}$, amplitudes $A_k(t_0) = |F_k|$ and phases θ_k. Since the functions we wish to Fourier transform are real ones, there is a relationship between the upper and lower halves of k-space: $A_{-k}(t_0) = A_k(t_0)$, $\theta_{-k} = -\theta_k$. We therefore only store $\boldsymbol{k}$ in the upper half of k-space (uhs) and there are only n_{k+} terms in the sum:

$$F_b(\boldsymbol{r}, t_0) = 2 \sum_{\boldsymbol{k} \in \text{uhs}} A_k[\cos(\boldsymbol{k} \cdot \boldsymbol{r} + \theta_k)], \qquad A_k \equiv |F_k|, \tag{D1}$$

$$s_b(\boldsymbol{r}, t_0) = 2 \sum_{\boldsymbol{k} \in \text{uhs}} \hat{k} k^{-1} A_k[\sin(\boldsymbol{k} \cdot \boldsymbol{r} + \theta_k)]. \tag{D2}$$

Because this is a direct summation, and many operations are required for each $\boldsymbol{k}$ and each spatial point $\boldsymbol{r}$, it costs many times $n_{\text{pts}} n_{k+}$ in total operations to evaluate. Although we only need to calculate these quantities at those points that lie within the peak patch associated with the candidate points, this can be quite a large fraction of the entire volume. This is therefore a costly operation, even though we at least do not have to evaluate it for each filter. If the characteristic Lagrangian radius of the patches is small compared with the overall box size, as it is for clusters, it is often adequate for us to evaluate the direct sum only at $\boldsymbol{r}_{\text{pk}}$ and assume it varies sufficiently slowly over R_{pk} that we can take its contribution as constant. The number of evaluations is then often quite manageable. Whether or not this can be done, it is clear that we wish to minimize n_{k+} and strategies for minimizing this are very useful.

For the n_{k+} ultralong wavelength vectors in the upper half of k-space, the discretizations of the magnitudes of the vectors, k, and the directions, $\hat{k}$, are at our disposal. We parameterize the upper half sphere by the usual longitude $\varphi \in [0, 2\pi)$ and the cosine of the colatitude $\mu = \hat{k}_z$, with μ restricted to lie in the range $[0, 1]$. The 2-sphere measure is $d\Omega_{\hat{k}}/(2\pi) = d\mu\, d\varphi/(2\pi)$. In practice, we split k, μ, and φ into n_k, n_μ, and n_φ bins, with $n_{k+} = n_k n_\mu n_\varphi$. A given wavevector among the n_{k+} total has three labels, one for the k-bin, one for the μ-bin and one for the φ bin in which it resides. However, within the bins, random number choices are made so that the

k vector is not on the bin boundary. This strategy serves two purposes, ensuring by the binning that k space is well covered, yet by the randomness of $\hat{k}$ within the bins that special lines in k-space are avoided. The radial wavenumber choice deserves special comment. Assume there is a minimum wavenumber allowed, $k_{\min}$, as well as the maximum we are adopting, $k_{\max} = k_b$. We choose the radial wavenumber components k as $k_j = k(q_j)$, $j = 1, \ldots, n_k$. Here $q_j = (j - 0.5)\Delta q$, where $\Delta q = 1/n_k$, and $k(q)$ is a sampling function which goes from $k_{\min}$ at $q = 0$ to $k_{\max}$ at $q = 1$. How we choose it to go in between depends upon what sort of spectrum we have. Let $[\Delta\sigma_F^2]_j$ be the power in F in the $[k_{j-0.5}, k_{j+0.5})$ interval; this is approximately

$$[\Delta\sigma_F^2]_j \approx \frac{k_j^3 P_F(k_j)}{(2\pi^2)} \bigg/ w(k_j), \qquad \text{where } w(k) = \frac{(dq/d\ln k)}{\Delta q}. \tag{D3}$$

In practice, we use one or two of the following forms:

$$\text{logarithmic: } q = \ln(k/k_{\min})/\ln(k_{\max}/k_{\min}), \qquad k(q) = k_{\min}(k_{\max}/k_{\min})^q, \tag{D4}$$

$$w = n_k/\ln(k_{\max}/k_{\min}),$$

$$\text{power law: } q = \frac{k^{n_S} - k_{\min}^{n_S}}{k_{\max}^{n_S} - k_{\min}^{n_S}}, \tag{D5}$$

$$k(q) = [k_{\min}^{n_S} + q(k_{\max}^{n_S} - k_{\min}^{n_S})]^{1/n_S}, \qquad w = \frac{n_k n_S k^{n_S}}{(k_{\max}^{n_S} - k_{\min}^{n_S})};$$

$$\text{hybrid power law: } q = \alpha \frac{k^{n_S} - k_{\min}^{n_S}}{k_{\max}^{n_S} - k_{\min}^{n_S}} + (1 - \alpha) \frac{k^{2n_S} - k_{\min}^{2n_S}}{k_{\max}^{2n_S} - k_{\min}^{2n_S}}, \tag{D6}$$

$$k(q) = k_{\min} x_S^{1/n_S}, \qquad w = (c_1 x_S + a_2)x_S,$$

$$\text{where } x_S = (1 + \alpha x_1)/(1 - \alpha) + a_1^2 + q, \qquad x_1 = (k_{\max}/k_{\min})^{n_S},$$

$$a_1 = \frac{\alpha(x_1 + 1)}{2(1 - \alpha)}, \qquad b_1 = \frac{(x_1^2 - 1)}{(1 - \alpha)}, \qquad c_1 = \frac{n_k n_S 2(1 - \alpha)}{(x_1^2 - 1)}, \qquad a_2 = \frac{n_k n_S \alpha}{(x_1 - 1)}.$$

An FFT is approximately like a power-law sampling function, with power $n_S = 3$, except that it poorly samples near the fundamental mode of the box. When long-wavelength power is needed, our standard strategy is: for the longest wavelengths, we use the logarithmic law; for slightly shorter ones we use the power-law hybrid law with $n_S = 1$ and $\alpha = 0.5$, which is a combination of a linear and square sampling strategy. Each sampling regime is given a separate set of bin numbers, n_k, n_μ, n_φ. The volume of a bin in k-space is $(k_j^3 - k_{j-1}^3)/(n_\mu n_\varphi)$. We choose the sharp k-space cut between logarithmic and hybrid sampling when the volume of the bin with hybrid sampling is smaller than the volume of the bin with logarithmic sampling (if it ever is). For k_b, the transition to where we use the FFT, it is that wavenumber at which the hybrid sampling bin volume equals the volume of a cell in the reciprocal lattice, $(2\pi/L_{\text{box}})^3$, where L_{box} is the comoving length of the box.

Another possible approach is to use very large coarse boxes that have a discrete number of our boxes within them, perform Fast Fourier transforms to get F_b on a very coarse grid, and then interpolate to get the local values. Although we have not used this approach, for some cases it could be faster than the direct one we have adopted.

APPENDIX E
ALGORITHMS FOR LOCAL PEAK-PATCH MEASUREMENTS

Given the list of candidate "peak" lattice cells, we still need to determine the properties of the regions about them. We have Fourier components of the (unfiltered) density field $\tilde{F}_k$ and of the displacement field $\tilde{s}_k$. As mentioned earlier, we actually smooth F with a "minimal" Gaussian filter, $R_G = 0.5a_L$, to damp high-frequency noise in the realization, which has negligible effect on peaks whose sizes are well above a_L, i.e., those of interest. The choice $R_G = 0.5a_L$ arises because it is the Gaussian filter reasonably well-matched to filtering at the Nyquist wavenumber π/a_L. (In FFTs, wavenumbers actually extend to $\sqrt{3}\pi/a_L$, but only in certain directions in the box. To relate a Gaussian filter to a_L, we equate the volume within a Nyquist-frequency sharp k-space filter $[6\pi^2(a_L/\pi)^3]$ with the volume associated with a Gaussian-filter $[(2\pi)^{3/2}R_G^3]$; this yields $R_G = (3\sqrt{\pi}/2)^{1/3}a_L/\pi = 0.49a_L$.

To calculate the mass-averaged quantities $\bar{F}$, $\bar{s}$, and $\bar{e}_{ij}$, and test for collapse, we use the fields sampled on the lattice points r_p:

$$F_p = F(r_p) \qquad s_p = s(r_p).$$

Consider a peak at location r_{pk}. We shall denote the positions of the lattice points relative to the peak center by

$$R_p = r_p - r_{\text{pk}} \qquad R_p = |R_p|.$$

Since the initial density is uniform, mass averages are equivalent to volume averages. Until a more sophisticated approach to the identification of a Lagrangian region associated with a peak is found, we calculate these averages within Lagrangian spheres.

We first choose a radius at which to start our spherical integration. The intention is to first integrate outward to this radius, test for collapse at the redshift of the peak z_{pk}, and then step the radius of integration outward or inward until we find the radius at which the transition between collapse and noncollapse occurs. If we reach the peak center after stepping inward without finding a collapse, then we throw out the peak from the list.

We step in radius by "shells" of the lattice about the center. Because of the cubical symmetry of the grid, the shells (outside the center pixel) come in discrete radial steps and contain at least six cells each. We number the shells m outward from the origin in radius $R[m]$, with $n[m]$ cells on the shell. The radial sampling is roughly even in R^2, since R^2/a_L^2 is an integer that is the sum of 1, 2, or 3 squares of integers. Unfortunately, the number of cells on each shell fluctuates from shell to shell, e.g., 6, 8, 12, 24, 48. This does not present a problem if we smooth or sum over multiple shells.

For shell m, we calculate the quantities

$$\delta F[m] = \frac{1}{n[m]} \sum_{p \in m} F_p, \quad \delta s[m] = \frac{1}{n[m]} \sum_{p \in m} s_p, \quad \delta s_i R_j[m] = \frac{1}{n[m]} \sum_{p \in m} s_{p,i} R_{p,j}, \tag{E1}$$

which are stored as we move outward in radius. At any given shell we compute the volume average of the density field

$$R^3[m]\bar{F}[m] = R^3[m-1]\bar{F}[m-1] + 0.5(\delta F[m-1] + \delta F[m])(R^3[m] - R^3[m-1]). \tag{E2}$$

Our first search is to find the shell m_c at which $\bar{F}$ first crosses the critical value $f_c = 1.686$,

$$\bar{F}[m_c] \geq f_c, \qquad \bar{F}[m_c + 1] < f_c.$$

This defines the region of collapse in the spherical approximation, and we can interpolate the $\bar{F}$ between the shells to find the Lagrangian radius

$$R_{pk,sph}^3 = R^3[m_c] + (R^3[m_c + 1] - R^3[m_c]) \frac{\bar{F}[m_c] - f_c}{\bar{F}[m_c] - \bar{F}[m_c + 1]}. \tag{E3}$$

The expression for the mass-averaged strain $e_{ij}(<R)$ in terms of the surface integral of the relative displacements was given in equation (2.26). We have s_i only on lattice sites—hence we need a method to interpolate the field from the lattice sites onto the bounding spherical shell. We do this by using a spline, that is a smoothing kernel similar to the Gaussian kernel W_G. Although the Gaussian, $W_G \propto \exp[-r^2/(2R_G^2)]$, has many desirable features (it is very smooth and interpolates linearly with high accuracy when the particle separation is $\sim R_G$), one must go out a relatively large distance, $3R_G$, to drop to a percent contribution in the interpolation. Instead, we use the piecewise polynomial smoothing function of compact support given by equation (2.9), a spherically symmetric kernel based on Schoenberg's B-splines (Monaghan 1985). The mean number density of the lattice grid points is the inverse of the volume of a cell, a_L^{-3}, where a_L is the lattice spacing. The field s_i at a point R about r_{pk} is approximated by

$$\Delta s_i(r) = \sum_p a_L^3 \Delta s_i(r_p) W_{sph}(r - r_p; R_h). \tag{E4}$$

Only those lattice points within $2R_h$ of the shell at radius R contribute to the angle-average which gives $\bar{e}_{ij}$. We would like to choose $2R_h$ to be as small as possible to avoid getting a contribution from points too far afield, yet it must be large enough so that a number of radial grid-shells contribute. In our code, we adopt the smoothing size of the lattice ($R_h = a_L$), which interpolates on the grid over 27 points. The angular integral in equation (2.26) can be readily performed by introducing, for each grid point p, a coordinate system with polar axis $\hat{R}_p$, $\mu_p = \hat{R} \cdot \hat{R}_p$, and an azimuthal angle ϕ_p. Averaging $\hat{R}$ over the azimuthal angle then gives $\mu_p \hat{R}_p$. To integrate over μ_p, we change variables to $Q_p = |R - R_p|$, which has the limits $|R - R_p| \leq Q_p \leq R + R_p$, yielding

$$e_{ij}(<R) = -\frac{3a_L^3}{\pi R_h^3} \sum_p \frac{(\Delta s_{p,i} R_{p,j} + \Delta s_{p,j} R_{p,i})}{2R} \mathcal{U}(R/R_h, R_p/R_h), \tag{E5}$$

$$\mathcal{U}(u, u_p) \equiv \int_{(R-R_p)^2}^{\min[4R_h^2, (R+R_p)^2]} dQ_p^2 \frac{W_{nsph}(Q_p; R_h)}{4RR_p} \frac{(R^2 + R_p^2 - Q_p^2)}{2RR_p}. \tag{E6}$$

The integral $\mathcal{U}$ over the kernel in equation (E5) can easily be calculated for the piecewise polynomial SPH kernel. To display the explicit equation, we introduce the following abbreviations and functions,

$$u = R/h_p, \quad u_p = R_p/h_p, \quad u_- = |u - u_p|, \quad u_+ = u + u_p$$

$$g_1(x, w) = -\tfrac{31}{35} - \tfrac{1}{4}x^4(1 - x^2 + \tfrac{3}{7}x^3) - \tfrac{7}{5}w + \tfrac{1}{4}wx^2(2 - \tfrac{3}{2}x^2 + \tfrac{3}{5}x^3).$$

$$g_2(x, w) = \tfrac{8}{35} - \tfrac{1}{4}x^4(2 - \tfrac{12}{5}x + x^2 - \tfrac{1}{7}x^3) - \tfrac{2}{5}w + wx^2(1 - x + \tfrac{3}{2}x^2 - \tfrac{1}{5}x^3).$$

We then have

$$
\begin{aligned}
\mathcal{U}(u, u_p) &= g_1(u_-, u^2 + u_p^2) && \text{for } u_- \le 1, u_+ > 2, \\
&= g_2(u_-, u^2 + u_p^2) && \text{for } 1 \le u_- \le 2, u_+ > 2, \\
&= g_1(u_-, u^2 + u_p^2) - g_2(u_+, u^2 + u_p^2) && \text{for } u_- \le 1, 1 \le u_+ \le 2, \\
&= g_2(u_-, u^2 + u_p^2) - g_2(u_+, u^2 + u_p^2) && \text{for } 1 \le u_- \le 2, 1 \le u_+ \le 2, \\
&= g_1(u_-, u^2 + u_p^2) - g_1(u_+, u^2 + u_p^2) && \text{for } u_- \le 1, u_+ \le 1, \\
&= 0 && \text{otherwise.}
\end{aligned}
\tag{E7}
$$

Since we use the lattice spacing for the smoothing, $R_h = a_L$, the interpolation from a given lattice site spreads over 27 points. Thus, to calculate $e_{ij}[m]$ on lattice shell m, we smooth over a radius of four cells. Of course, the ideal procedure is to mass-average $e_{ij}(<R)$ in the same way as for $\bar{F}[m]$. Even though we have smoothed over more than just a single shell, our estimation will be somewhat inaccurate. However, the errors will affect all of the components in about the same way, so since we have $\bar{F}[m]$ from the spherical shell integration stored, we renormalize the $e_{ij}(<R)$ by dividing by the trace calculated using the spline smoothing and multiplying all components by $\bar{F}[m]$. The values of the peak ellipticity e_v and prolaticity p_v (eq. [2.20d]) are, of course, unaffected by this renormalization.

Thus, at the radius $R[m]$, we use the $\bar{F}[m]$ and the calculated e_v and p_v to determine $z_c[m]$, which is in turn compared to the $z_{\rm pk}$. By our search in radius, we locate the shell m_0 such that

$$z_c[m_0] \ge z_{\rm pk} \qquad z_c[m_0 + 1] < z_{\rm pk}.$$

The Lagrangian radius $R_{\rm pk}$ is then determined by interpolation in $z_c[m]$ between the shells:

$$R_{\rm pk,hom}^3 = R^3[m_0] + (R^3[m_0 + 1] - R^3[m_0]) \frac{z_c[m_0] - z_{\rm pk}}{z_c[m_0] - z_c[m_0 + 1]}. \tag{E8}$$

We obtain the mass of the peak (in nonrelativistic, i.e., clustering, matter) from the Lagrangian top-hat radius,

$$M_{\rm pk} = \frac{4\pi}{3} \bar{\rho}_{\rm nr}(z_{\rm pk}) \bar{a}_{\rm pk}^3 R_{\rm pk}^3 = 1.156 \times 10^{12} \Omega_{\rm nr}(R_{\rm pk}/h^{-1} \text{ Mpc})^3 h^{-1} M_\odot. \tag{E9}$$

The mean overdensity $\bar{F}(<R_{\rm pk})$ is interpolated linearly in R^3 between the shells, the reverse of the interpolation equation (E3). To get the mean displacement of the peak, we volume average s over the lattice points inside $R_{\rm pk}$

$$\bar{s}_{\rm pk} = \frac{1}{N} \sum_{m=0}^{m_0} n[m]\delta s[m], \qquad N = \sum_{m=0}^{m_0} n[m], $$

where $\delta s[m]$ is the shell average of s_p (eq. [E1]).

For the calculation of the (perturbed) internal binding energy (per unit mass), $\varepsilon_{\rm int,pk}$, we need to mass-average $\bar{F}(<R)$ as in equations (2.27a)–(2.27b). To evaluate $S_{\rm pk}$, we use the simple numerical integration

$$S[m] = \frac{1}{R^5[m]} \sum_{m'=1}^{m} \frac{1}{2} (\bar{F}[m' - 1] + \bar{F}[m'])(R^5[m'] - R^5[m' - 1]), \tag{E10}$$

$$S_{\rm pk} = \frac{1}{R_{\rm pk}^5} R^5[m_0] S[m_0] + \frac{1}{2} (\bar{F}[m_0] + \bar{F}_{\rm pk})(R_{\rm pk}^5 - R^5[m_0]). \tag{E11}$$

Other local properties of the peaks can also be measured. For example, a byproduct of our strain eigenvalue determinations are the orientation angles of the strain tensor's principal axes. If one can convince oneself that these have will be aligned with the principal axes of the virialized objects, at least statistically, then they can be used to address such issues as the Binggeli effect, i.e., of clusters tending to align with other clusters. We have not yet checked how well this works compared with N-body studies, although we are convinced that it is much better to use the initial peak-strain tensor alignments to discuss this effect than principal axes alignments of the tensor $(\nabla_i \nabla_j F)_{\mathrm{pk}}$ that Bond (1987b) originally suggested.

REFERENCES

Bardeen, J. M., Bond, J. R., Kaiser, N., & Szalay, A. S. 1986, ApJ, 304, 15 (BBKS)

Barnes, J., & Hut, P. 1986, Nature, 324, 446

———. 1989, ApJS, 70, 389

Bernardeau, F. 1994, ApJ, 427, 51

Bertschinger, E. 1987, ApJ, 23, L103

Binney, J., & Quinn, T. 1991, MNRAS, 249, 678

Binney, J., & Tremaine, S. 1987, Galactic Dynamics (Princeton: Princeton Univ. Press)

Bond, J. R. 1986, Galaxy Distances and Deviations from the Universal Expansion, ed. B. F. Madore & R. B. Tully (Dordrecht: Reidel), 255

———. 1987a, Nearly Normal Galaxies from the Planck Era to the Present, ed. S. Faber (New York: Springer), 388

———. 1987b, in Proc. Workshop Cosmology and Particle Physics, ed. I. Hinchcliffe (Singapore: World Scientific), 22

———. 1988, in Proc. NATO Summer School, The Early Universe, ed. W. G. Unruh (Dordrecht: Reidel), 283

———. 1989a, in Proc. Vatican Study Week, Large-Scale Motions in the Universe, ed. V. Rubin & G. Coyne (Princeton: Princeton Univ. Press), 419

———. 1989b, in Frontiers of Physics: From Colliders to Cosmology, ed. A. Astbury et al. (Singapore: World Scientific), 182

Bond, J. R., Cole, S., Efstathiou, G., & Kaiser, N. 1991, ApJ, 379, 440 (BCEK)

Bond, J. R., & Myers, S. 1991, Trends in Astroparticle Physics, ed. D. Cline & R. Peccei (Singapore: World Scientific), 262

———. 1993a, in Proc. 3d Teton Summer School, The Evolution of Galaxies and Their Environment, ed. M. Shull & H. Thronson, NASA CP 3190, 21

———. 1993b, in Proc. 3d Teton Summer School, The Evolution of Galaxies and Their Environment, ed. M. Shull & H. Thronson, NASA CP 3190, 52

———. 1995a, ApJS, 103, 41 (BM2)

———. 1995b, ApJS, 103, 63 (BM3)

———. 1995c, preprint (BM4)

Bond, J. R., Szalay, A. S., & Silk, J. 1988, ApJ, 324, 627

Chandrasekhar, S. 1969, Ellipsoidal Figures of Equilibrium (New Haven: Yale Univ. Press)

Cole, S., & Kaiser, S. 1988, MNRAS, 233, 637

Couchman, H. M. P. 1991, ApJ, 368, L23

Davis M., Efstathiou, G., Frenk, C. S., & White, S. D. M. 1985, ApJ, 292, 371

Doroshkevich, A. G. 1970, Astrophysica, 6, 320

Doroshkevich, A. G., & Shandarin, S. 1978a, Soviet Astron., 22, 653

———. 1978b, MNRAS, 182, 27

Dubinski, J., & Carlberg, R. G. 1991, ApJ, 378, 496

Evrard, G. 1990, ApJ, 363, 349

Gott, J. R., & Rees, M. J. 1975, A&A, 45, 365

Gunn, J. E., & Gott, J. R. 1972, ApJ, 176, 1

Gurbatov, S., Saichev, A., & Shandarin, S. 1989, MNRAS, 236, 385

Hernquist, L., & Katz, N. 1989, ApJS, 70, 419

Hoffman, Y., & Ribak, E. 1991, ApJ, 380, L5

Icke, V. 1973, A&A, 27, 1

Lahav, O., Lilje, P. B., Primack, J. R., & Rees, M. J. 1991, MNRAS, 251, 158

Lilje, P. B. 1991, ApJ, 386, L33

Martel, H. 1991, ApJ, 377, 7

Martel, H., & Wasserman, I. 1990, ApJ, 348, 1

Monaghan, J. M. 1985, J. Comput. Phys., 60, 253

Monaghan, J. M., & Lattanzio, J. C. 1985, A&A, 149, 135

Park, C. 1990, MNRAS, 242, 59

Peacock, J. A., & Heavens, A. F. 1985, MNRAS, 217, 805

———. 1990, MNRAS, 243, 133

Peebles, P. J. E. 1980, Large-Scale Structure of the Universe (Princeton: Princeton Univ. Press) (PS)

———. 1984, ApJ, 284, 439

Press, W. H., & Schechter, P. 1974, ApJ, 187, 425

Press, W. H., & Teukolsky, S. A. 1990, Comput. Phys., 1990 Jan/Feb., 92

Quinn, T., & Binney, J. 1992, MNRAS, 255, 729

Shandarin, S. F., & Zeldovich, Ya. B. 1989, Rev. Mod. Phys., 61, 185

van Haarlem, M., & van de Weygaert, R. 1993, ApJ, 418, 544

van de Weygaert, R., & Bertschringer, E. 1995, preprint

Villumsen, J. 1989, ApJS, 71, 407

Weinberg, S. 1987, Phys. Rev. Lett., 59, 2607

White, S. D. M., & Silk, J. 1979, ApJ, 231, 1

Zeldovich, Ya. B. 1970, A&A, 5, 84